Deposition of Hydrogen-Doped Indium Oxide Thin Films Using Atmospheric-Pressure Plasma-Enhanced Spatial Atomic Layer Deposition

Anusha Varanasi

TU Delft
TNO innovation for life
PVMD Delft University of Technology

Deposition of Hydrogen-Doped Indium Oxide Thin Films Using Atmospheric-Pressure Plasma-Enhanced Spatial Atomic Layer Deposition

by

Anusha Varanasi

in partial fulfillment of the requirements for the degree of

Master of Science
in Electrical Sustainable Energy

at the Delft University of Technology,
to be defended publicly on Friday, September 8, 2017 at 11:00 AM.

Supervisors:	Dr. Olindo Isabella,	TU Delft
	Dr. Andrea Illiberi,	TU Delft and TNO
	Prof. dr. Fred Roozeboom,	TU Eindhoven and TNO
Thesis committee:	Prof. dr. Arno Smets,	TU Delft
	Dr. Olindo Isabella,	TU Delft
	Prof. dr. Fred Roozeboom,	TU Eindhoven and TNO

This thesis is confidential and cannot be made public until September 8, 2018. The work reported in this thesis was conducted in the period of Nov. 2016 to Sept. 2017

An electronic version of this thesis is available at http://repository.tudelft.nl/.

TU Delft Delft University of Technology

Abstract

Transparent conductive oxides (TCOs) are wide bandgap semiconductors characterized by high conductivity and high transparency in the visible and near infrared spectrum of light. TCOs find applications in displays, thin film transistors, solar cells, etc., due to these distinctive properties. Hydrogen-doped indium oxide (IO:H), a TCO first developed in 2007, is emerging as a material of interest because of its high mobility (>100 $cm^2/V.s$) and high transparency (>90 % in the visible region of the spectrum) as compared to other TCOs such as tin doped indium oxide (ITO) and aluminium doped zinc oxide (AZO).

Recently, IO:H has been developed using sputtering and temporal atomic layer deposition. However, each has its disadvantages such as the development of pinholes in TCO films, long purge steps in ALD process, etc. For this reason, a new deposition method has been investigated.

In this thesis, IO:H has been deposited using atmospheric-pressure plasma-enhanced spatial atomic layer deposition. In the first part of this project, the use of N_2 plasma along with water and trimethylindium (TMI) vapour as the prime reactants for the deposition of IO:H films with thicknesses typically around 140 nm on alumino-boro-silicate glass substrates was studied. The process parameters such as flow rate of water, exposure time of the substrate to the reactants, etc. were optimized, and the ALD process temperature window was found to be between 150 °C and 225 °C. In the next part of the project, H_2/N_2 plasma was employed to further reduce the total process time and to enable deposition of a high-quality TCO at a lower temperature. The use of H_2/N_2 plasma almost doubled the rotation speed of the substrate (i.e., substrate exposure time reduced from typically 300 ms to 150 ms). This opens ways for faster net deposition rates that typically correspond to 0.02 nm/s.

The electrical, optical and structural properties of the thin films deposited using both the plasmas were studied. It is demonstrated that using H_2/N_2 plasma, it is possible to deposit high-quality thin films with carrier mobility values as high as 85 $cm^2/V.s$ at 150 °C and 110 $cm^2/V.s$ at 175 °C with resistivity values of only ~ 2.5 mΩ.cm. When N_2 plasma was used similar values were recorded at 200 °C and 225 °C. A transparency of ~ 90 % in the visible region of the spectrum and ~ 85 % on an average was observed in the spectral range of 300-1800 nm in both the cases and the absorbance was found to be below 10 %. XRD and SEM analysis of the thin films showed that the layers deposited are polycrystalline. The average size of the crystal increases in the direction parallel to the surface of the substrate with an increase in the deposition temperature. The average size increases from ~ 50 nm to ~ 100 nm when N_2 plasma is used and from ~ 35 nm to ~ 70

nm when H_2/N_2 plasma is used.

Finally, a preliminary optical analysis of the thin film on a CuInSe (CIS) solar cell was performed and compared with an ITO-based CIS cell stack. From the simulation results, it was seen that no parasitic absorption occurs in IO:H in the near infrared region of the spectrum. The advantage of high transparency of IO:H, as compared to ITO, is somewhat lost as the thickness of IO:H thin film has to be increased to compensate for the relatively higher resistivity of the material as compared to ITO.

The knowledge gained from the spatial ALD process developed in this thesis and the properties of the thin films deposited as such will propel advancements to further improve the deposition technique for low temperature and large area applications in commercial *roll-to-roll* and *sheet-to-sheet* production of thin films on polymer substrates.

Contents

1 Introduction **1**

1.1 Transparent Conductive Oxides 1

1.2 Properties of a TCO 3

1.2.1 Scattering. 4

1.3 Indium Oxide 6

1.4 Hydrogen-doped indium oxide 8

1.5 Thin-film deposition techniques 9

1.6 Motivation and thesis objectives. 11

1.7 Thesis outline. 12

2 Thin-film growth of indium oxide using ALD and doping in IO:H **13**

2.1 Reactants used for ALD of indium oxide 13

2.2 Doping in indium oxide 15

2.2.1 Doping in semiconductors 15

2.2.2 Oxygen vacancies 17

2.2.3 Hydrogen as a donor 18

3 Equipment for thin-film deposition and characterization **21**

3.1 Deposition 21

3.1.1 Spatial ALD reactor 21

3.1.2 Plasma generation and sources 23

3.1.3 Surface Dielectric Barrier Discharge 24

3.2 Characterization 26

3.2.1 Spectroscopic ellipsometry. 26

3.2.2 Spectrophotometry 27

3.2.3 Hall Setup 29

3.2.4 Four-point probe 31

3.2.5 X-ray diffraction 32

3.2.6 Scanning Electron Microscopy (SEM) 33

4 Deposition of hydrogen-doped indium oxide thin films using N_2 plasma 35

4.1 Introduction 35

4.2 The ALD process window 35

4.2.1 Non-ideal effects in ALD 37

4.3 Process parameters 38

4.4 The ALD process window using N_2 plasma 40

4.5 Film thickness uniformity 41

4.6 Structural Properties 42

4.7 Optical Properties 45

4.8 Electrical Properties 47

4.9 Concluding remarks 51

4.10 Limitations 52

5 Deposition of hydrogen-doped indium oxide thin films using H_2 plasma 53

5.1 Introduction 53

5.2 Motivation for using H_2 plasma 53

5.3 Process parameters 54

5.4 The ALD process window using H_2 plasma 55

5.5 Film thickness uniformity 56

5.6 Structural Properties 57

5.7 Optical properties 59

5.8 Electrical Properties 60

5.9 Concluding remarks 63

6 Optical modelling of IO:H thin films in a CIS solar cell 65

6.1 Introduction 65

6.2 Optical modelling and simulations 65

6.3 Optical simulations using GenPro4 66

6.3.1 Validation using IO:H-Glass interface 67

6.3.2 Comparison of IO:H with ITO 67

6.4 Concluding remarks 69

7 Conclusions and recommendations **71**

7.1 Concluding remarks 71

7.2 Recommendations 73

A Recipe for the deposition of IO:H thin films using plasma enhanced spatial ALD **75**

A.1 Deposition using N_2 plasma 75

A.2 Deposition using H_2/N_2 plasma 76

B Determination of the optical bandgap using the Tauc plot **77**

C Relation between the refractive index, electrical and optical properties **79**

8 Glossary **81**

8.1 List of acronyms 81

8.2 List of symbols 83

Bibliography **87**

1
Introduction

Climate change is one of the most pressing problems of the 21st century. The average global temperature has risen by 0.85 °C from 1880 to 2012 [1]. As the threat of global warming looms large on humanity, the world is slowly but surely moving towards sustainable practices living practices. A major part of this shift is the production of energy from renewable sources.

Amongst renewable energy technologies, photovoltaics have begun to play a substantial role in the power generation sector and their contribution is steadily rising. One of the many components of a thin-film solar cell is a transparent conductive oxide (TCO). TCOs are a unique class of materials that are both transparent and conductive. For this reason, they are of great interest for applications in solar cells. Apart from photovoltaics, TCOs are widely used in the semiconductor and the electronics industries and are extensively researched. In this thesis, one such TCO, hydrogen-doped indium oxide is chosen as the material of interest.

This chapter is a general introduction to the thesis. First, a review of some essential characteristics of transparent conductive oxides is discussed followed by an overview of the structure of indium oxide. The motivation for choosing hydrogen-doped indium oxide over other TCOs is then presented. Several thin film deposition techniques are discussed and in the end, the motivation, objectives and the outline for this thesis are presented.

1.1. Transparent Conductive Oxides

Transparent conductive oxides (TCOs) are a unique class of materials that have become a ubiquitous part of the modern industry in the past few decades. TCOs are oxidic thin films that are characterized by high optical transparency, with absorption less than 6-7 % in the visible part of the electromagnetic spectrum and high electrical conductivity ($\sim 10^4\ \Omega^{-1}\text{cm}^{-1}$) [2]. Modern devices such as touch panels and displays, organic light emitting diodes (OLEDs), microelectronic devices, sensors, etc., extensively make use of

TCOs. Each of the applications mentioned has a different requirement regarding properties of layers and the ability to tweak a material for various uses makes thin film TCOs very attractive for research.

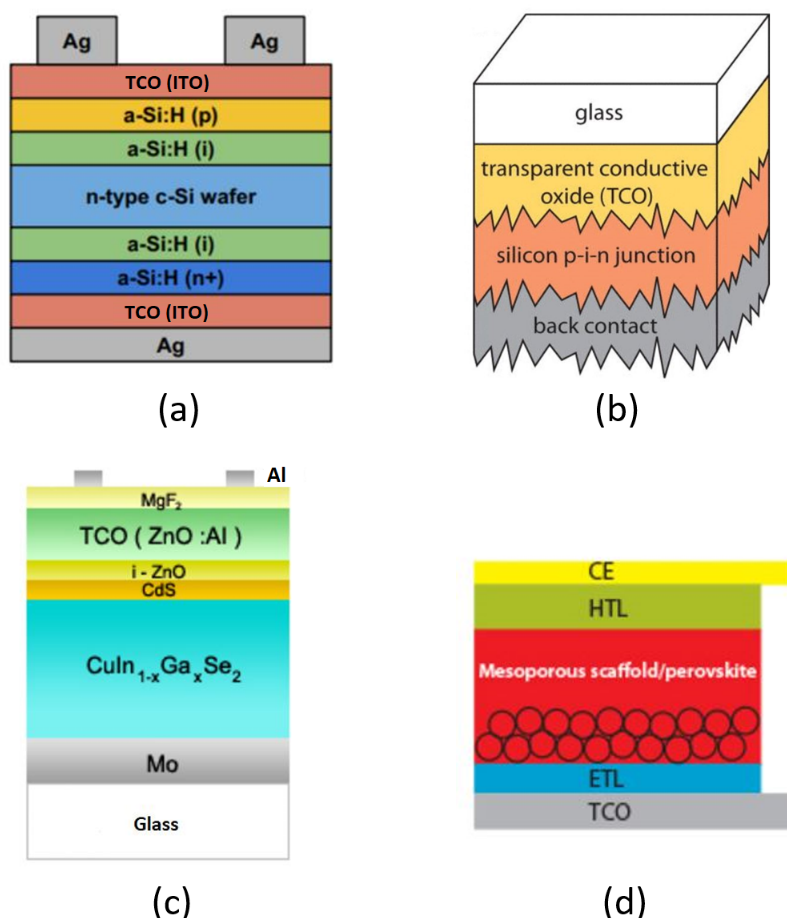

Figure 1.1: (a) SHJ solar cell [3], (b) Thin-film Si cell in a superstrate configuration [4] (c) CIGS solar cell [5] , and (d) Perovskite solar cell [6].

TCOs are particularly important in the solar cell industry. Figure 1.1 shows the schematics of four different solar cells that have been or are being commercialized. The first cell is a silicon-based heterojunction (SHJ) solar cell, the second is a thin-film Si solar cell, the third cell is a copper indium gallium (di)selenide solar cell and the fourth is a perovskite based solar cell. A TCO can be used as a front and back electrode and also as a back reflector. When used as an electrode, as shown in figure 1.1a for example, it must have a high conductivity and transparency in the spectral region of the solar cell. Further, the TCO must have additional properties as a strong scatterer of incident light and must act as a good nucleation layer for the growth of Si in a superstrate configuration for thin-film cells, as shown in figure 1.1b. When used in combination with a back reflector design, the TCO serves to reflect the light back into the cell and as a diffusion barrier. In tandem cells, it is also used to reflect light between the cells. Evidently, TCOs have a decisive

influence on the efficiency of the solar cells and optimizing them for the each particular use is critical [2].

1.2. Properties of a TCO

The conductivity and transparency of a TCO are two of its most important qualities. TCOs act as selective transmitting layers as they are transparent in the visible and NIR range and reflect the far IR radiations.

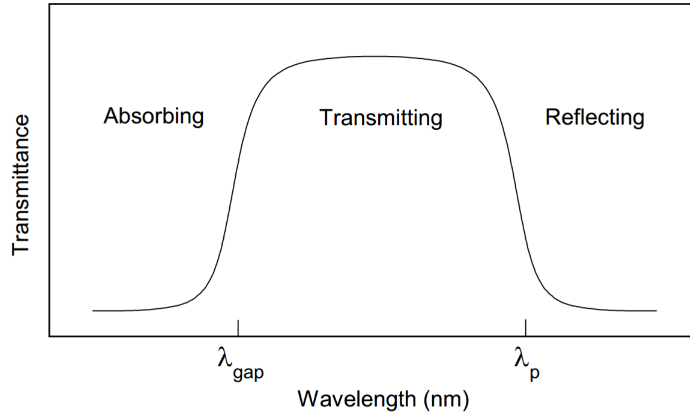

Figure 1.2: Transmission spectrum of a TCO. The wavelengths λ_{gap} and λ_p correspond to the wavelengths at which the bandgap absorption and free electron plasma absorption take place.[7].

Figure 1.2 shows the typical transmission spectrum of a TCO material. For wavelengths less than λ_{gap} (wavelength corresponding to the bandgap), since the photon energy is higher than the bandgap of the material, it gets absorbed resulting in the band to band transitions. For wavelengths higher than the λ_p (wavelength corresponding to the plasma frequency), the light is reflected [8]. To understand plasma frequency, a material can be viewed as a collection of a negatively charged plasma of a free electron gas and stationary, positively charged cores when the scale is much larger than the inter-atomic distances. When an oscillating field is applied, the electron plasma oscillates at a natural frequency known as plasma frequency, ω_p and is expressed by equation 1.1,

$$\omega_p = \sqrt{\frac{Ne^2}{\varepsilon_0 \varepsilon_\infty m^*}} \tag{1.1}$$

where, ε_∞ is the high-frequency permittivity, ε_0 is the permittivity of vacuum, N is the carrier concentration and m^* is the effective electron mass.

The relative permittivity of the material (ε_r), as expressed by equation 1.2, depends on the interaction of the oscillating field and the electron plasma [7, 9],

$$\varepsilon_r(\omega) = \varepsilon_1 + i\varepsilon_2 \tag{1.2}$$

where, ε_1 and ε_2 are the real and complex part of the material's permittvity and are functions of the plasma frequency, ω_p, (refer equations C.5 and C.6 in Appendix C).

Further, the complex refractive index ($\overline{n}_r$) of the material can also be expressed in terms of relative permittivity [1] (refer equation 1.3), where the real part (n_r) is the refractive index and imaginary part (k) is the extinction coefficient.

$$\overline{n}_r = (n_r - ik) = \sqrt{\varepsilon} \tag{1.3}$$

From equation 1.2 and 1.3, it is clear that plasma frequency plays an important role in determining the optical properties of a material. For frequencies higher than ω_p, the material behaves as a transparent dielectric as the electrons are unable to respond to the electric field component of the incoming radiation. On the other hand, at values of $\omega < \omega_p$, since the electrons respond instantly to the applied electric field, the TCO behave as a conductor and behave as a reflector [7, 9].

The conductivity (σ) of a TCO is the product of the number of charge carriers and the mobility (μ) of these carriers. This is shown in equation 1.4,

$$\frac{1}{\rho} = \sigma = N * e * \mu \tag{1.4}$$

where ρ is the resistivity, N is the carrier density and e is a unit charge [10]. From this equation, it is clear that the conductivity can be increased by increasing the number of charge carriers. This can be done in several ways which depend on the material and its structure. The nature of the dopant will decide if the TCO will be p or n-type.

The carrier concentration is also closely related to the plasma frequency (equation 1.1) of a material which implies that an increase in N will also increase the plasma frequency and thus, the transparency of the thin-film will drop. For this reason, the conductivity and transparency of a TCO need to be balanced to achieve the desired properties.

Conductivity can also be increased by increasing the mobility of the carriers in the material. As the mobility depends on the scattering mechanisms, both intrinsic and extrinsic, it is a little more difficult to tune. An overview of the different scattering mechanisms is provided below.

1.2.1. Scattering

Carrier mobility is limited by scattering that occurs in a material by several mechanisms such as lattice scattering, electron-electron scattering, etc. Not all of them affect the mobility in the same way. The total mobility is expressed as in equation 1.5, where μ_{tot}

[1] As most transparent semiconductors are weakly magnetic, the relative permeability is set to 1

is the total mobility and μ_i is the contribution of each scattering mechanism. Some of the most important mechanisms at play in wide bandgap semiconductors are discussed below.

$$\frac{1}{\mu_{tot}} = \sum \frac{1}{\mu_i} \tag{1.5}$$

Ionized impurity scattering

Ionized impurity scattering is a mechanism by which the charge carriers in a material are scattered by the ionized particles in the material. In a doped material, it is the dominant form of scattering for a carrier density higher than 10^{19} cm^{-3} [11]. Several models based on the homogeneous distribution of scattering centers, (for e.g., Dingle [12]) assume that the scattering centers are statistically homogeneously distributed. This assumption is not valid when the concentration of the dopant increases (>10^{19} cm^{-3}) because of the formation of clusters that have a higher charge and hence lead to lower mobility [13].

Grain boundary scattering

In polycrystalline materials, grain boundaries are the regions between the grains or crystallites. They usually act as sources of defects that lead to a deterioration of material properties. These boundaries are generally a few atomic layers thick and form complex structures that represent the transitional region between the different orientations of neighbouring crystallites [14].

Seto *et al.*, in their research [14], assumed a barrier thickness, d, such that L_g is much greater than d, where L_g is the grain size. All the charges in the thickness d are assumed to be trapped, forming a depletion layer. The grain boundary can be modelled as a potential barrier for charge carriers. The mobility μ_{gb} can then be expressed as in equation 1.6,

$$\mu_{gb} = \mu_{gb0} \exp(-\frac{E_b}{k_b T}) \tag{1.6}$$

and

$$\mu_{gb0} = \frac{Lq}{\sqrt{2\pi m^* k_b T}} \tag{1.7}$$

where E_b is the height of the potential barrier, k_b is Boltzmann's constant, q is the charge of the trap and T is the absolute temperature.

Grain boundary scattering only has a significant effect on the total mobility of the material if L is comparable to the mean free path of the charge carriers in the material [7].

Neutral impurity scattering

At high doping concentrations (>10^{21} cm^{-3}), the inactive dopant material can form a variety of neutral complexes. These complexes act as scattering centers and have a significant

contribution in wide bandgap semiconductors. The contribution of this type of scattering is indirectly related to the carrier concentration. It depends on the concentration of neutral impurities which is calculated as a difference between the measured carrier density and the carrier concentration. In contrast, ionized impurity and grain boundary scattering, are directly related to the carrier concentration [7].

Phonon Scattering

Phonon scattering, also known as lattice scattering, is the result of the thermal vibrations in the lattice. Above 0 K, atoms in a lattice vibrate, creating waves called phonons. They can scatter charge carriers in a lattice and the effect of this scattering component is dependent on temperature as shown in equation 1.8 and it increases with increase in temperature [11].

$$\mu_{ph} = \mu_{ph0}\left(\frac{T}{T_0}\right)^{-p} \tag{1.8}$$

Here, μ_0 is the phonon mobility at the reference temperature T_0, T is the temperature at which the mobility is measured and p is a parameter that is 1 above the Debye temperature and between 2-4 below the Debye temperature [15].

1.3. Indium Oxide

Indium Oxide (In_2O_3) is a wide bandgap, n-type semiconductor. It is one of the few materials that can be doped to high concentrations (up to $10^{21}/cm^3$) while maintaining good transparency. Indium oxide can be either amorphous or crystalline depending on the deposition method and the process conditions. Amorphous layers can be grown at low temperatures (<150 °C) using sputtering [16] and pulsed laser deposition [17]. Polycrystalline layers are obtained either by depositing the material at high temperatures or by post-deposition annealing at high temperatures (>150 °C). In the crystalline phase, indium oxide exists in the body-centered cubic bixbyite (BCC) or the rhombohedral geometry, however, the BCC bixbyite structure is the most common one [18].

Each unit cell has 80 atoms, 48 of which are oxygen. Figures 1.3 and 1.4 present a schematic of the unit cell and bond lengths in the bixbyite structure. Indium has two non-equivalent positions, In1 and In2 [19]. The local structure of In1 is symmetrical with six In-O bonds that are shorter than the average In-O bond. In2 also bonds with six oxygen atoms, however, unlike In1, it does not have any linear O-In-O bonds. Oxygen bonds equivalently with four In atoms (one In1 and three In2) forming a tetrahedron [20]. The lattice parameter, a, for this crystal is 1.011 nm [19].

The cubic bixbyite geometry of indium oxide has an electrical bandgap of ~ 2.9 eV and an optical bandgap ~ 3.9 eV. This difference is because the valence band and the conduction band are both of even parity. Laporte's selection rule for centrosymmetric molecules states that only electronic transitions between states with opposite parities

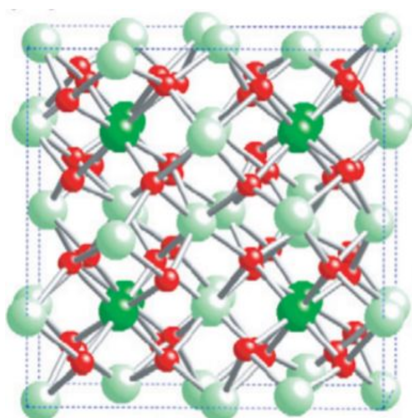

Figure 1.3: Structure of the indium oxide bcc-bixbyite crystal. The red balls represent oxygen, the dark green balls represent In1 and the light green ones represent In2 [19].

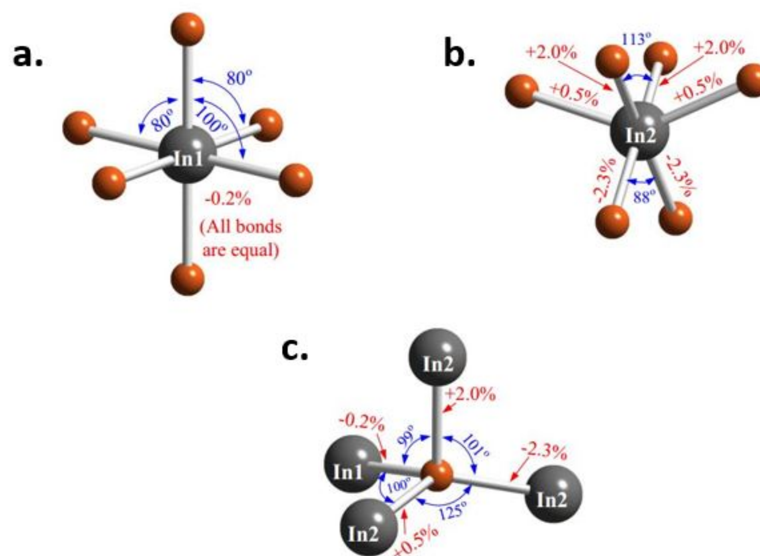

Figure 1.4: (a) Bonds in the In1 state (b) Bonds in the In2 state (c) Bonds with oxygen. The percentages show the deviation of the bond length from the average In-O bond length [20].

are allowed. The first allowable optical transition in indium oxide is at 0.81 eV higher than the optical bandgap (see Appendix B). It is the primary cause of the difference between the two bandgaps [11].

Indium oxide is used in several applications such as optical coatings, thin film transistors, infrared mirrors, as a sensing material in gas sensors, etc. [18]. Doped indium oxide is most commonly used as a transparent conductive oxide for many applications such as solar cells, liquid crystal displays, etc.

1.4. Hydrogen-doped indium oxide

TCOs such as indium tin oxide (ITO) and aluminum doped zinc oxide (AZO) are the mainstay of the modern photovoltaic and display industry because of their properties. ITO, deposited by sputtering (see section 1.5) has a mobility of 20-40 $cm^2/V.s$ at a carrier density $\sim 10^{20}/cm^3$. AZO, deposited by atomic layer deposition (see section 1.5) has a mobility $\sim$ 15 $cm^2/V.s$ with a carrier density in the order of $10^{20}/cm^3$. The higher mobility of ITO allows for a higher short circuit current in a solar cell. However, ZnO based TCOs are used as a low-cost alternative to the more expensive indium tin oxide. Both ITO and AZO have free carrier absorption in the near-infrared region owing to their carrier concentration [21] and it is detrimental to the performance of a solar cell.

Recently, it was discovered by Koida *et al.* [16] in 2007 that indium oxide doped with hydrogen (IO:H) serves as an excellent TCO. It was first developed by sputtering indium oxide in the presence of water vapor which acts as the source of hydrogen. The material can be synthesized at relatively low temperatures (< 200°C). One of the most striking properties that makes IO:H such an interesting material is its high mobility (> 100 $cm^2/V.s$) at carrier densities around $1 - 2 \times 10^{20}/cm^3$. The deposited films were annealed after deposition to obtain excellent film properties generated by the solid-phase crystallization in the film. High mobility allows for a reduction in the carrier density and thus, improvement in the transparency because of lower free carrier absorption. It makes hydrogen-doped indium oxide (IO:H) a promising material for use in photovoltaic applications. It is, thus, chosen as the material of interest for this project work. Table 1.1 summarizes the electrical properties of ITO, AZO and IO:H as found in literature and the absorption coefficients for doped zinc oxide and indium oxide TCOs are shown in figure 1.5. It can be seen that IO:H provides a clear advantage over both ITO and AZO.

Table 1.1: Comparison of electrical properties of ITO, AZO and IO:H [21].

Properties	**ITO**	**AZO**	**IO:H**
Mobility ($cm^2/V.s$)	20-40	10-15	60-120
Carrier density (X 10^{20} cm^{-3})	3.5	3.4-8.5	1-2
Resistivity (Ω cm)	10^{-4}	$10^{-3} - 10^{-4}$	$10^{-3} - 10^{-4}$

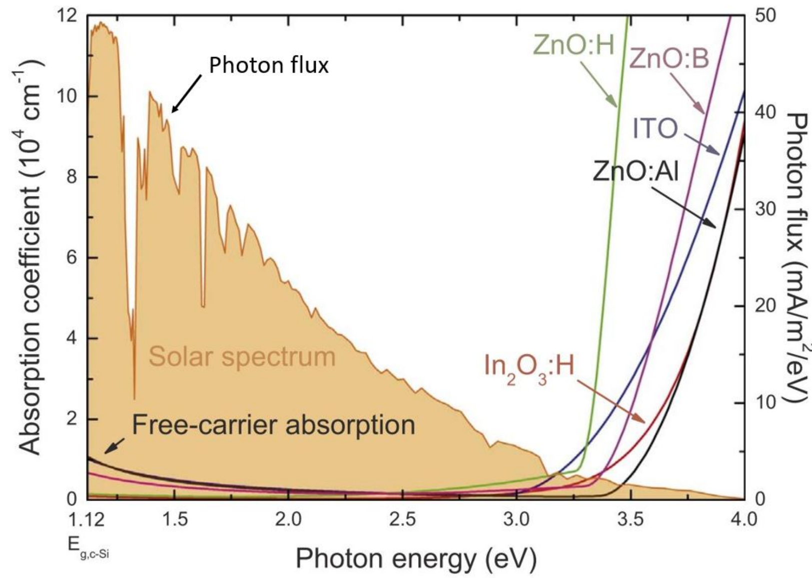

Figure 1.5: Absorption coefficients for various TCOs. AM 1.5 solar spectrum is shown for reference [22].

1.5. Thin-film deposition techniques

Thin-film deposition is carried out by several methods. They are generally classified into two broad categories- physical vapour deposition (PVD) and chemical vapour deposition (CVD). PVD consists of methods involving physical processes such as sputtering, evaporation, pulsed laser deposition (PLD), etc. CVD involves a chemical reaction of two or more reactants in the gas phase. Depending on more specific aspects, CVD can be further classified as vapor phase epitaxy, metalorganic CVD (MOCVD), atomic layer epitaxy (ALE), etc. Furthermore, the processes can either be thermal or plasma enhanced at different pressures (atmospheric or low pressure). Depending on the material to be deposited and the requirement of quality, thickness, film deposition rate, etc., a method is chosen [23].

Atomic layer deposition (ALD) is a variant of CVD with some significant differences. To be used in an ALD process, the precursor or the reactant must have three fundamental properties: (i) it must have enough vapour pressure to be transported to the substrate surface (ii) it should easily decompose into desirable reactive species at relatively low temperatures (iii) it should not react in the gas phase. Solid precursors are heated to achieve the required vapour pressures. The temperature is generally higher than the sublimation temperature of the precursor and its decomposition is a potential concern. Liquid precursors are delivered by bubbling, vapor draw or by direct liquid injection. The choice of the precursors is critical to the speed of the process and to the quality of the end product owing ultimately to the reaction kinetics [23].

In CVD, the precursors react with each other to form a new material which deposits on the substrate. In ALD, the precursor interacts with the substrate, either reacting or adsorbing on its surface. The reactions in ALD are *self-limiting*, propagated by half-

reactions that complete a full cycle to deposit a monolayer of the desired film, unlike in CVD. Two or more precursors or reactants are used. Figure 1.6 gives a schematic of the ALD process. A functionalized substrate (figure 1.6.1) is exposed to the first precursor. After all the available sites on the substrate have reacted completely, the reaction stops due to its self-limiting nature and the excess precursor is purged out (figure 1.6.2). The second precursor is then introduced into the reaction chamber (figure 1.6.3), which reacts with all the active sites building a monolayer of the desired material (figure 1.6.4). The additional precursor is purged again and the process continues until the desired thickness is achieved. The other major difference between CVD and ALD is that ALD forms a layer of *uniform thickness* and is *conformal*, making it an excellent choice for difficult geometries like 3-D trenches. CVD cannot be used to coat such substrates evenly [24, 25].

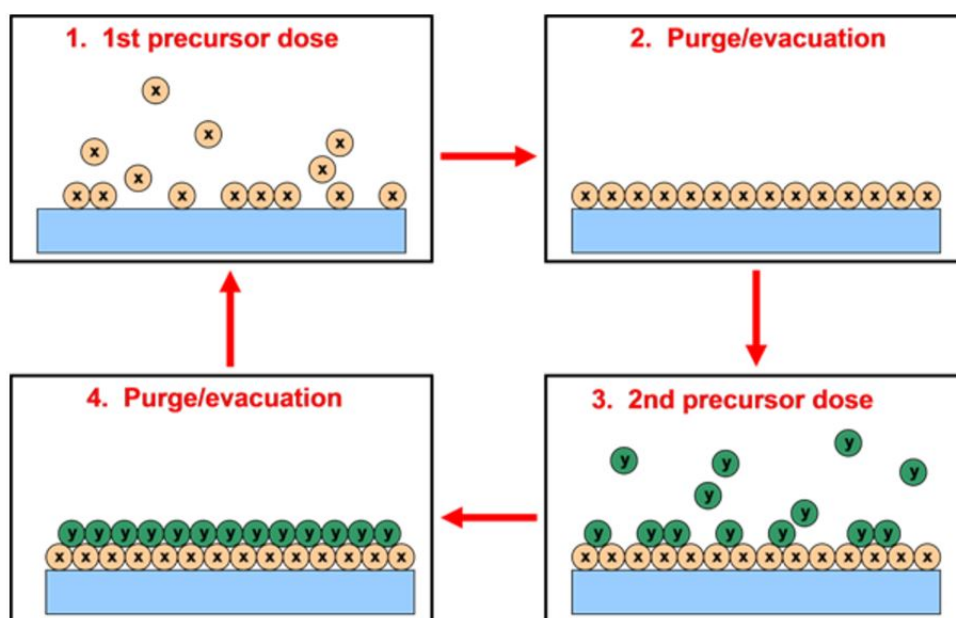

Figure 1.6: Schematic of a typical ALD reaction [26].

Due to the precise control of the process that ALD offers, it has been widely used to manufacture advanced CMOS logic and memory devices such as field effect transistors (FETs), capacitors for dynamic random access memory (DRAM) devices, photovoltaic thin-film devices, moisture barrier layers such as AlOx, etc. The reaction steps are only 10-100 milliseconds long, but the purge steps last longer, in the order of seconds. This makes conventional ALD, also known as *temporal* ALD, a slow process [25]. Another point to note is that since ALD is conformal, the complete reaction chamber is coated with the material. This is highly undesirable.

To overcome these disadvantages, temporal ALD was modified such that the precursors are delivered *spatially* instead of in a time-sequenced manner, eliminating the requirement for purge steps. The concept of spatial ALD was first proposed by Suntola *et al.* in 1977 but only since 2007 have several other research groups developed variations building on the original design [27]. The reactor design is such that the precursors are

separated spatially and that there is no coating on reactor walls (see section 3.1). The process can be adapted for in line processing in sheet-to-sheet and roll-to-roll techniques. This method has been successfully used to deposit alumina [28] and zinc oxide [29] and it holds promise as a useful method for indium oxide as well. A detailed description of spatial ALD is provided in Chapter 3, section 3.1.

1.6. Motivation and thesis objectives

IO:H has been synthesized in the past using sputtering [16, 30] and temporal ALD [11, 15]. However, each method has its disadvantage. Sputtering involves ion bombardment which may cause damage to the layers of the substrate as in a solar cell. Moreover, sputtering gives rise to pinholes which act as point defects, affecting the efficiency of the solar cell. Temporal ALD can be used to make thin, precise layers but it is too slow to be used for industrial processes. Several precursors such as InCp, TMI, etc., have been used in combination with water, oxygen, ozone and hydrogen peroxide, of which a decent growth rate per cycle (0.1 nm/cycle) has been achieved with the precursor indium cyclopentadienyl (InCp) (see section 2.1). This precursor is relatively expensive and thus less of an economically viable option for commercial up-scaling. All these issues warrant the use of a new method for the deposition of IO:H. Spatial ALD is a potential new approach as it provides the advantages of ALD such as precise control and uniformity while mitigating the disadvantages. For this reason, spatial ALD is chosen as the method of deposition for this project work.

The main objective of this thesis is to develop a high-quality film of hydrogen-doped indium oxide using plasma enhanced spatial atomic layer deposition with the application in photovoltaic technologies in mind. To meet this objective, the following research questions have been explored and answered.

1. Is it possible to develop an ALD process using the atmospheric-pressure plasma-enhanced spatial ALD technique?
2. What are the conditions required to deposit IO:H thin films successfully using this technique?
3. What is the influence of temperature on the structural, optical and electrical properties of the films?
4. Can the entire process be improved by using H_2/N_2 plasma?
5. How do the thin films deposited by this technique compare against ITO when an optical analysis is performed?

1.7. Thesis outline

The outline of the thesis is as follows. Chapter 2 deals with the work that has been reported in the literature concerning IO:H by ALD. The choice of precursors, the plasma source and the gases used will also be discussed. Chapter 3 provides a brief overview of the deposition equipment and the equipment used to characterize the layer. Characterization of the layers developed using nitrogen plasma and hydrogen plasma will be discussed in chapters 4 and 5, respectively. An optical analysis comparing ITO and IO:H is presented in Chapter 6. Finally, the conclusions from this project work and an outlook for further study will be briefly examined in Chapter 7.

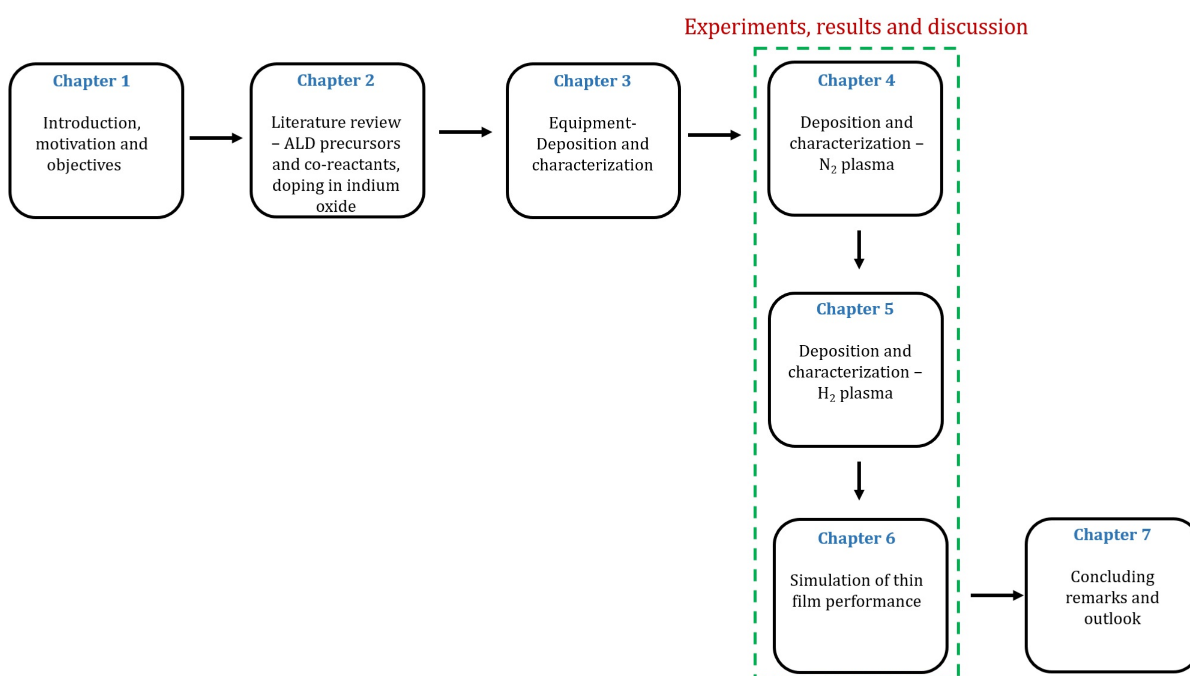

Figure 1.7: Thesis outline.

2

Thin-film growth of indium oxide using ALD and doping in IO:H

Before proceeding to the stage of process development, it is important to understand the advantages and disadvantages of using different precursors and co-reactants. A choice is made after considering all the aspects. The first section of this chapter gives a short description of the different precursors and co-reactants that have been reported in the literature for the ALD of indium oxide. In the next section, the concept of doping, its effect on the energy band structure and the different doping approaches that can yield potential charge carriers in IO:H will be briefly discussed.

2.1. Reactants used for ALD of indium oxide

Indium oxide films have been deposited using ALD with several precursor/co-reactant combinations and reported in the literature. A summary of several methods published is given below.

The first reports of depositing In_2O_3 films using ALD were with $InCl_3$ as the source of In and H_2O/H_2O_2 as the source of oxygen. This method requires very high process temperatures (350 °C - 500 °C) and the by-product of the reaction (HCl) is highly corrosive. $InCl_3$ has a high sublimation temperature of 285 °C. Through its by-product, HCl, $InCl_3$ also etches the growing In_2O_3 film [31]. β-diketonates such as $In(hfac)_3$, $In(thd)_3$, $In(acac)_3$ have been investigated. They, however, yield very little or no growth at all [32]. A combination of indium cyclopentadienyl (InCp) and O_3 was used at temperatures around 200 °C for application in thin-film solar cells, but thickness nonuniformities were reported due to the apparent thermal decomposition of O_3 [33]. InCp, when used either with water or oxygen alone, produced little or no growth. When employed in a *synergistic* combination with water and oxygen, InCp produced hydrogen-doped indium oxide layers with a growth rate (0.12 nm/cycle). It is likely that water strips the Cp ligand while oxygen

oxidizes In from +1 to +3 state. The layers were also produced on large area substrates (12 x 18 in.^{2} Si substrate, 8 x 8 in.^{2} glass substrate) with high uniformity in thickness and resistivity [34] [35]. Though InCp was successfully used to develop In_2O_3 layers, it has several disadvantages. The cost of the precursor ($400 per gram, Strem Chemicals, Inc.) makes it challenging for commercial applications. InCp is a solid precursor and can sinter and age over time. It also has a low vapour pressure of 0.1 Torr at 45 °C [36].

Trimethylindium (TMIn or TMI), on the other hand, is a relatively cheap precursor ($62 per gram, Strem Chemicals, Inc.). It is already widely used in the CVD industry for applications in thin film transistors to deposit materials such as IGZO (indium gallium zinc oxide) [37] and for the deposition of group III nitrides [36]. TMI is a liquid at room temperature and has a high vapour pressure of 8 Torr at 45 °C . TMI, in combination with water, is reported to yield a growth rate of 0.4-0.5 Å/cycle at temperatures ranging between 200-250 °C. At temperatures below 250 °C , water is unable to completely break the $In-CH_3$ bonds because TMI is not very reactive to the In-OH bond [36]. This surface reaction may be triggered by reactive species generated by plasma [11]. Beyond 250 °C, TMIn decomposes, leading to the development of very rough films [36]. High temperatures are not very economical and also cause damage to other layers of a solar cell.

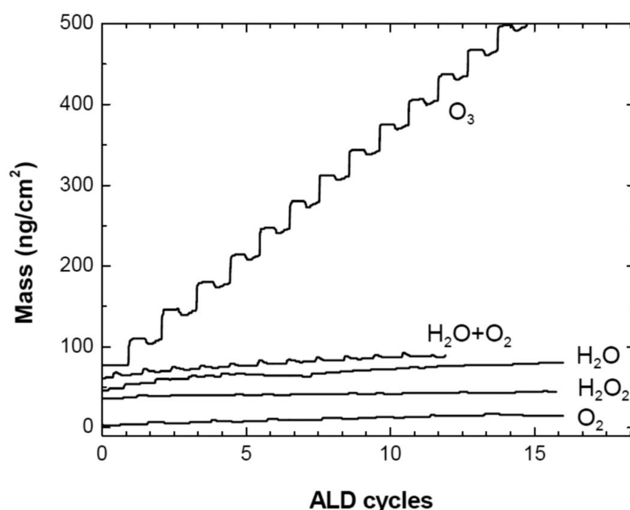

Figure 2.1: Quartz crystal microbalance (QCM) measured in situ for different co-reactants used in thermal ALD with TMI [36].

TMI has been used in combination with several oxygen sources such as O_3, O_2, H_2O, and H_2O_2 as a co-reactant, between 100 °C and 200 °C. Of these, only O_3 was effective in forming In_2O_3 films, using thermal ALD, with good electrical and optical properties but a low growth rate (0.42-0.55 Å/cycle) (figure 2.1). The synergistic combination of water and oxygen does not work with TMI because it is not very reactive towards the In-OH bond. In the case of InCp, oxygen oxidizes In from the +1 to the +3 state while water replaces the ligand. As In is already in the +3 state in TMI, oxygen might become redundant and this could be the reason why the combination of water/oxygen as used by Libera *et al.* [34]

does not work for TMI. Even after functionalizing the substrate with In_2O_3, the reaction between TMI and water is not sustained as shown in figure 2.2 [36].

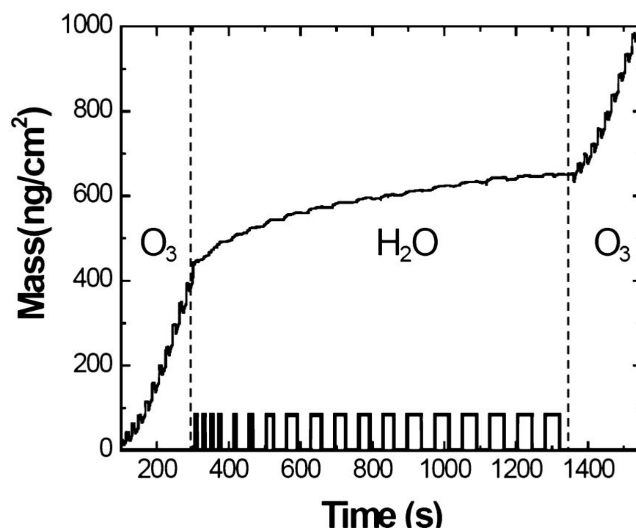

Figure 2.2: QCM measured in situ for the reaction of TMI with water on a substrate functionalized with In_2O_3 (TMI+ozone) [36].

The reports so far, imply that the reaction between TMIn and water requires extra activation, in one form or another, for continuous growth of the film. In this thesis, plasma enhancement is used to provide the necessary energy to boost this reaction. Plasmas composed of N_2 and H_2 along with water vapour have been used and their effects are discussed in chapters 4 and 5, respectively.

Plasma is a cloud of charged particles, electrons, ions and radicals that is usually produced by applying a high voltage across a gas causing a breakdown (see section 3.1). In this project, two different approaches were used. In the first case, nitrogen plasma was used to dissociate water molecules to form reactive species, which then actively react with TMIn. In the second case, plasma was generated using a mixture of hydrogen and water. This was, then, made to react with TMI to produce IO:H.

2.2. Doping in indium oxide

2.2.1. Doping in semiconductors

The incorporation of a small amount of impurity to a pure semiconductor serving to increase its conductivity is called doping. The dopant usually has either more or fewer valence electrons as compared to the undoped semiconductor. In ideal indium oxide, the indium atoms have three valence electrons. When doped with Sn, for example, which has four valence electrons, one of them is loosely bonded to the lattice. After absorption of energy, at room temperature, the electrons are free to move within the lattice. This makes ITO a negatively doped material. If a dopant element with only two valence

electrons is used, the material will be positively doped [38].

In a semiconductor, the arrangement of atoms in a crystal lattice or the amorphous phase of the semiconductor results in a range of allowed and forbidden energy levels known as energy bands and bandgaps, respectively. The density of energy states is the number of allowed states per unit of volume and energy. The Fermi-Dirac distribution function describes the ratio of the states filled with an electron to the total number of allowed states at an energy E as shown in figure 2.3.

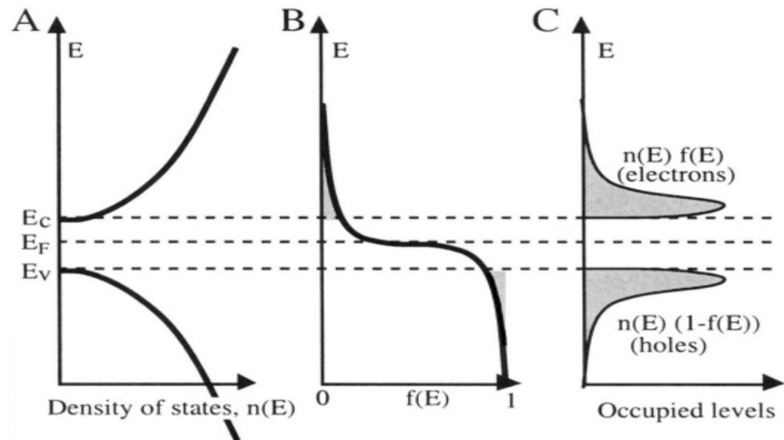

Figure 2.3: (A) Density of states near the bottom of the conduction band and the top of the valence band, (B) Fermi-Dirac function, and (C) density of holes and electrons in the conduction and valence band [39].

The energy difference between the conduction band minimum (CBM) and the valence band maximum (VBM) energy level is called a bandgap. The bandgap may be either direct or indirect. The position of the valence and conduction band may change in different directions in a lattice and thus the propagation of charge carriers also differs. In a direct bandgap material, the VBM is vertically aligned with the CBM. This means that the energy provided by a photon is sufficient to excite the electron. In an indirect bandgap semiconductor, the CBM and the VBM are not vertically aligned and thus an extra momentum is needed for the transfer (figure 2.4) [38].

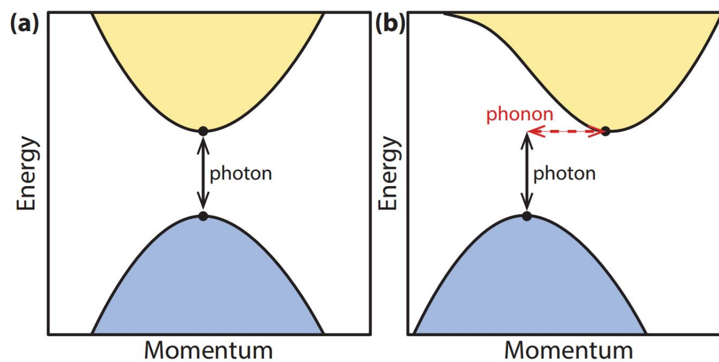

Figure 2.4: (a) Direct bandgap (b) Indirect bandgap [38].

For an intrinsic semiconductor, the Fermi level is in between the VBM and the CBM energy levels. Upon doping with a donor, the energy of the electron lies in the conduction band and the Fermi level shifts up. When the dopant is an acceptor, the Fermi level shifts down towards the valence band as illustrated in figure 2.5 [38].

The nature of the bandgap of indium oxide is not very clear. It has been suggested based on experimental evidence that it is an indirect bandgap material. However, it has been shown by Erhart *et al.* [40] that the experimental observations that indicate an indirect bandgap may not be related to the electronic structure of the bulk.

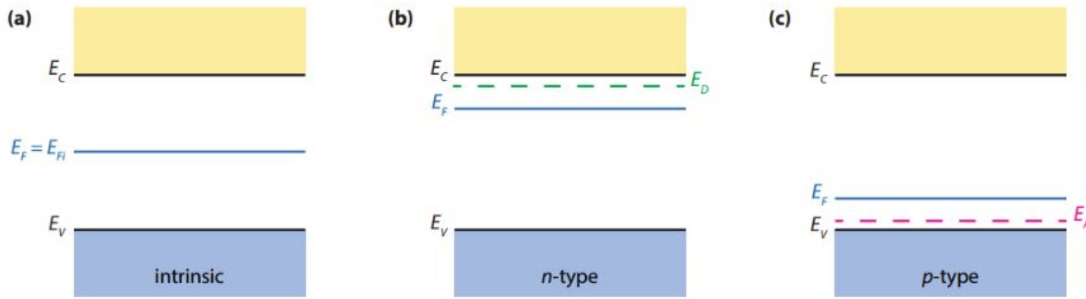

Figure 2.5: Position of the Fermi level in (a) an intrinsic, (b) n-type and (c) p-type semiconductor. E_C represents the CBM and E_V represents the VBM. E_D represents the energy levels introduced by the weakly bound electrons from the donor atoms and E_A represents the same for acceptor atoms [38].

The optical bandgap is defined as the energy required for a photon to excite an electron from the valence to the conduction band. In a *non-degenerate semiconductor*, the electronic bandgap and the optical bandgap are usually equal. In *degenerate* semiconductors, since all bottom states in the conduction band are fully occupied, the energy of the photon needed to excite the electrons to available energy levels in the conduction band is higher. In this situation, the optical bandgap is larger than the electrical bandgap and this shift is known as the Burstein-Moss shift. Even when semiconducting metal oxides are nominally undoped, they are usually n-type. Defects such as interstitials, vacancies, etc., act as donors, increasing the carrier density. The critical carrier density of indium oxide is ~ 6.4×10^{18} cm^{-3}. The measured carrier density of undoped indium oxide deposited by ALD is generally larger than 10^{19} cm^{-3} implying that the material is degenerate. In indium oxide, the defects mentioned above act as sources of negatively charged carriers, making it an n-type material. To develop films with sufficient conductivity (~ 1-2 mΩ.cm) with a transparency above 85 %, an understanding of the donors in the material is imperative [11].

2.2.2. Oxygen vacancies

It has been reported in the literature that the conductivity in nominally undoped indium oxide arises from the creation of oxygen deficiencies. These deficiencies can act

as donors. The vacancies are stable in two states: +2 and 0. For tin doped indium oxide, on the other hand, the increased carrier concentration is attributed to the removal of interstitial oxygen atoms forming complexes with Sn^{4+} [41].

A correlation between increasing oxygen partial pressure and the decrease in the carrier concentration was observed by Ellmer *et al.* [13]. Also, a drop in the carrier concentration and increase in mobility was observed after annealing indium oxide in an atmosphere of oxygen. This indicates that oxygen vacancies that act as shallow donors are removed upon annealing. An increase in mobility shows that the introduction of interstitial oxygen atoms was unlikely as that would decrease the mobility as the atoms would behave as ionized impurities [41]. Libera *et al.* [34] have also reported that charge carriers in hydrogen doped indium oxide may be associated with oxygen vacancies. While all this points to oxygen vacancies as the main donors, it is not the case. Instead, it has been shown that hydrogen itself can act as a potential donor [20, 42]. This is discussed in the following section.

2.2.3. Hydrogen as a donor

Atomic probe tomography of In_2O_3 deposited using the ALD technique by Wu *et al.* [42] has shown that hydrogen is a shallow donor in indium oxide. Their deuterium isotope labelling study using heavy water showed that the hydrogen, incorporated in the layer, originated from both the co-reactant (H=D) and the ligand (CH_3), but the contribution from the co-reactant was higher. Hydrogen can be incorporated as interstitial (H_i) and substitutional (H_O) defects in semiconductors. Interstitial H_i occupies a site that is unoccupied while substitutional hydrogen replaces oxygen in the crystal lattice. H_i is an amphoteric donor in most semiconductors, meaning that, in an n-type material, it is H_i^-, compensating for the donors [20]. However, in some materials, like ZnO, they will act exclusively as donors. This was confirmed experimentally by Hofmann *et al.* [43]. Limpijumnong *et al.* [20] have shown a similar behavior exhibited in indium oxide.

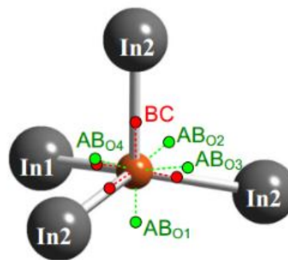

Figure 2.6: Presence of interstitial hydrogen in indium oxide [20].

H_i occurs in three states: +, -, 0. Of these three, only H_i^+ acts as a donor. It prefers sites near the anions and is unstable at the bonding sites. The AB_{O1} antibonding site as shown in figure 2.6 has the lowest energy of formation (-2.09 eV) and is the most likely site of occupation at moderate film growth temperatures. For the negatively charged states,

sites closer to In are preferred.

H_O has been found to be exclusively a donor in the + charge state. The formation energy of H_O^+ is higher than H_i^+ but low enough to contribute significantly to the total carrier density. Oxygen vacancies (V_O) actually behave as deep donors in the indium oxide lattice, occurring in two stable states: 2+ and 0 [20].

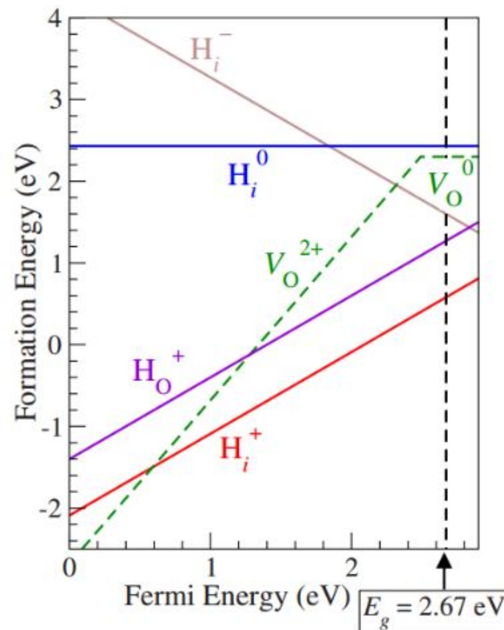

Figure 2.7: Occurrence of interstitial hydrogen and oxygen vacancies in indium oxide [20].

Figure 2.7 shows the formation energy of the different sites described above versus the Fermi energy level. It is observed that the formation energies for H_i^+ and H_O^+ are relatively low, and thus, they can both coexist in the material. H_i^-, however, can only exist in degenerate materials. Substitutional hydrogen H_O, formed by the binding of V_O with H_i has a high binding energy of 1.82 eV, implying that H_O is stable.

3

Equipment for thin-film deposition and characterization

In this chapter, a brief overview of the equipment used to deposit and characterize the IO:H thin films is given. First, the equipment for deposition, a rotary spatial Atomic Layer Deposition (ALD) reactor is treated. In the following sections, the equipment used for optical, electrical and structural characterization are discussed.

3.1. Deposition

3.1.1. Spatial ALD reactor

In this section, the deposition equipment, a rotary spatial ALD reactor is discussed. This reactor, developed in-house at TNO, was used to deposit the IO:H thin films on glass substrates. The basic principle of the process is, in essence, the same as temporal ALD (see section 1.5). Each precursor reacts to complete a half-reaction and a monolayer is formed after a full cycle. The two methods are different in the way the precursors are delivered to the substrate and the half-reactions are carried out. Figure 3.1 shows a bottom view of the gas injection head on the left and a side view of the reactor on the right.

All the precursors are fed by bubbling a carrier gas such as N_2 through a container. They are delivered to the reactor head by a series of pipes into different compartments in the head. The substrate, shown in red, rests on the substrate table which rotates freely, typically 10-50 rpm, while the reactor head is stationary. In this research work, Schott AF 32 eco Thin glass and Corning Eagle-XG glass, both with an area of 15 x 15 cm^2 were used as substrates. They are both alumino-boro-silicate glass substrates. The distance between the table and the head is typically 20-200 μm. As shown in figure 3.2, the precursors are separated from each other by a gas curtain which is created by the flow of an inert gas such as nitrogen or argon from the reactor head towards the substrate (green portion of the disc). Each precursor slot has a main outlet through which the precursor

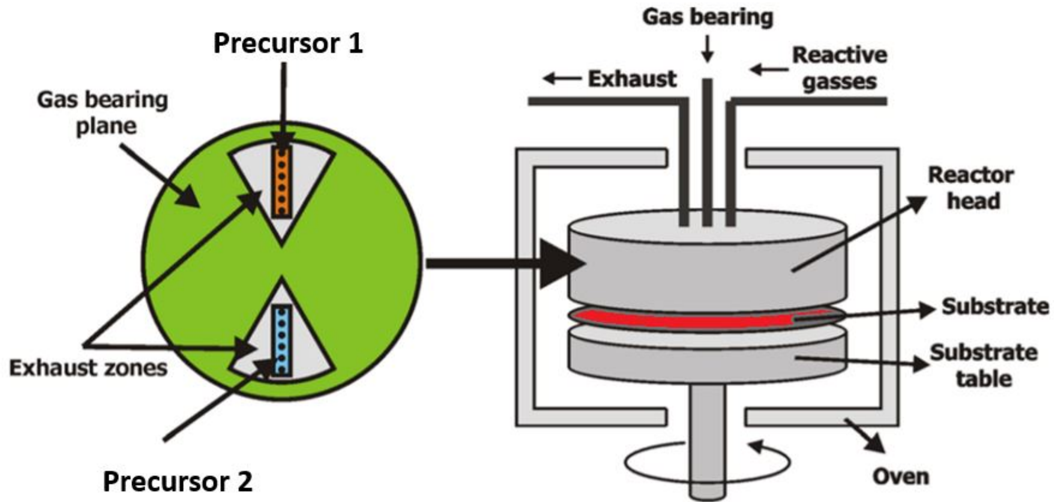

Figure 3.1: Schematic showing a bottom view of the gas injection head and a side view of the reactor [25].

reaches the substrate. The excess precursor is vented through exhaust channels that are present on either side of the main outlet in the slot. The substrate rotates, being exposed to each of the precursors in turn. The function of the gas bearing is two-fold. The first function is the separation of reactants from each other. The second function is to hold down the substrate against the substrate table, effectively acting as a non-contact frictionless bearing between the head and the substrate. This feature allows for mechanical robustness. As the shape of the reactor is circular in this case, the film is deposited in the shape of a donut as indicated by the blue zone in figure 3.3.

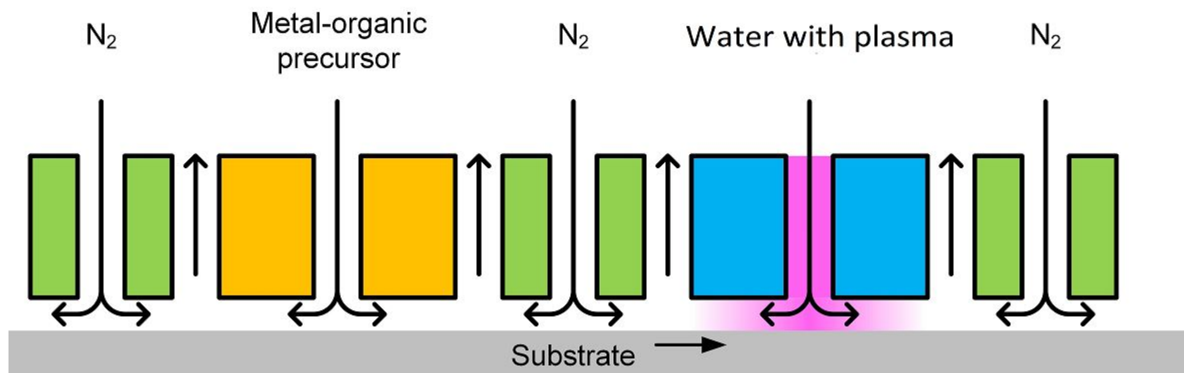

Figure 3.2: Schematic of the spatial ALD reactor showing the reaction separation by the gas bearing.

In this research, trimethylindium (TMI) is the metal-organic precursor. When the rotation speed of the substrate table is fixed, the exposure time of the substrate itself to the precursor decreases as one moves towards the outer circumference of the donut.

This effect is compensated for, by using a *pie-shaped* slot such that the exposure time at all points is equal. The slot for TMI is pie-shaped, ensuring equal exposure time at all points on the substrate. The slot for water, however, houses the plasma source which is linear (figure 3.3). This geometry causes interesting effects during deposition as shown in chapters 4 and 5.

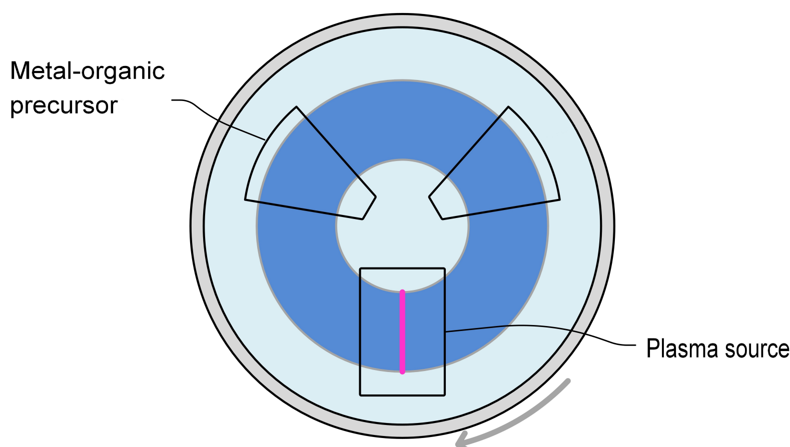

Figure 3.3: Schematic showing the slots for TMI and plasma injection.

The properties of IO:H are known to improve after annealing the thin-film in vacuum or an inert atmosphere after deposition. To study this, some of the samples were annealed after deposition using a hot plate placed in a glove box under an atmosphere of argon. The samples were annealed at 200 °C for thirty minutes.

3.1.2. Plasma generation and sources

Plasma, which is sometimes called the fourth state of matter, is a collection of charged particles, electrons, ions, neutral atoms, radicals and photons. The plasma is neutral as a whole because of the charge balance among the different reactive species.

There are several mechanisms to generate plasma. Conventionally, a *direct* plasma is created by an electric field between two parallel electrodes across a low pressure gas such that the electrons are accelerated (see figure 3.4a). The average electron temperature is between 1-5 eV while the temperature of the reactive gas is 300-500K. The plasma so created is not in equilibrium due to the low gas pressures that are usually used and is called a 'cold' plasma. These electrons further ionize the gaseous reactants through electron induced collisions and sustain the plasma. A direct plasma configuration, most commonly used in plasma enhanced chemical vapour deposition (PECVD), consists of two parallel electrodes. One of the electrodes is charged while the other is grounded. The substrate is placed on the grounded electrode and plasma is generated between the plates at radio frequency. The process conditions of the plasma and the reactive gases cannot

be controlled independently.

A *remote* plasma is generated far from the actual site of reaction and then delivered to the required site (see figure 3.4b). Many electrons and ions are lost in the transport, with mostly radicals reaching the reaction chamber by diffusion. In a remote plasma with RF substrate biasing, the process parameters of the plasma and the reactive gases can be controlled fairly independently unlike in a direct plasma source.

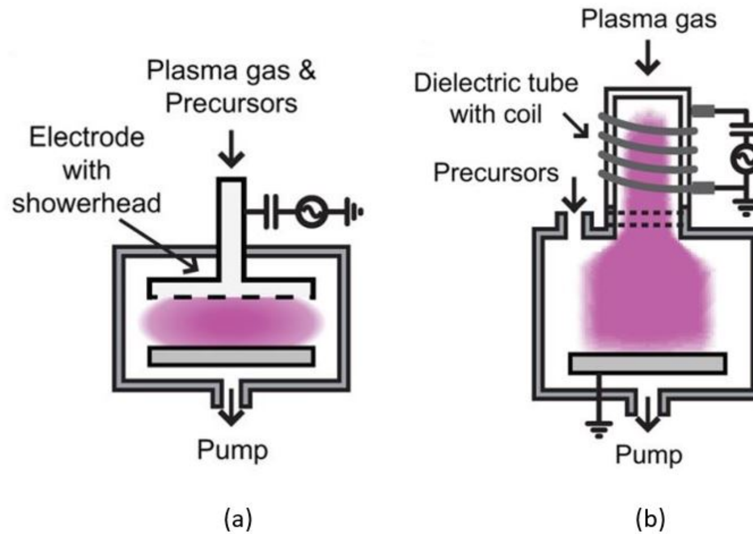

Figure 3.4: Schematic of a (a) direct plasma source (b) remote plasma source [44].

3.1.3. Surface Dielectric Barrier Discharge

In this project work, a remote surface dielectric barrier discharge (SDBD) is used [44]. While plasma processes are usually carried out in vacuum or at low pressure, switching to atmospheric pressure is advantageous as it eliminates the requirement for expensive vacuum systems. Existing low-pressure plasma systems can be used to generate plasma at atmospheric pressure but due to the high number of collisions between the reactive species, the plasma loses its non-thermal nature.

At atmospheric pressure, electrical breakdown occurs in filaments called microdischarges. Current begins to flow when the electric field in the discharge gap is high enough to breakdown the gas, thus creating a plasma. Breakdown phenomena depend non linearly on the product of the pressure, p, and the distance between the electrodes, d, as shown by Paschen curves (figure 3.5).

After the breakdown of the gas, in most cases, a large number of microdischarges are created. To avoid damage due to microdischarges and to spread them uniformly over a large volume or surface, a dielectric barrier discharge is used. Dielectric Barrier Discharges (DBD) are self-sustaining discharges with an insulating material inserted in between the discharge path. The dielectric acts as a buffer and ensures a uniform plasma

is created. As the dielectric cannot pass DC, an AC source is required. The basic configurations of a DBD plasma source are shown in figure 3.6 [45].

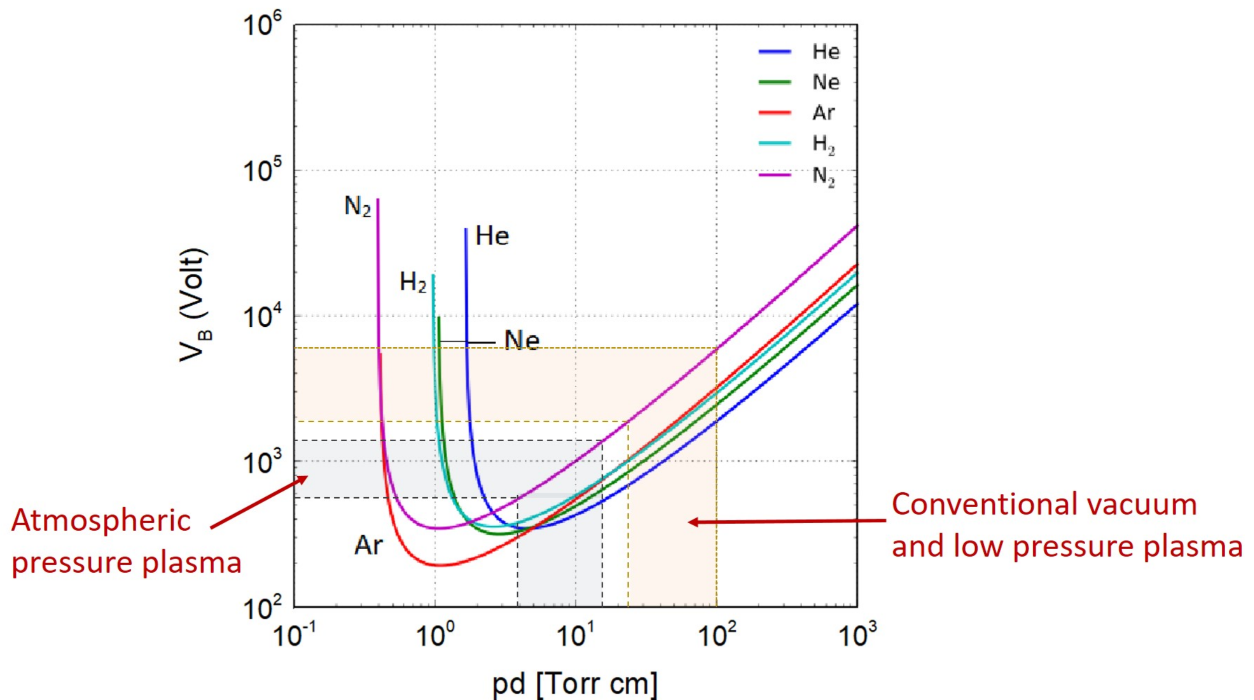

Figure 3.5: Paschen curves for the most common gases used to generate plasma [46].

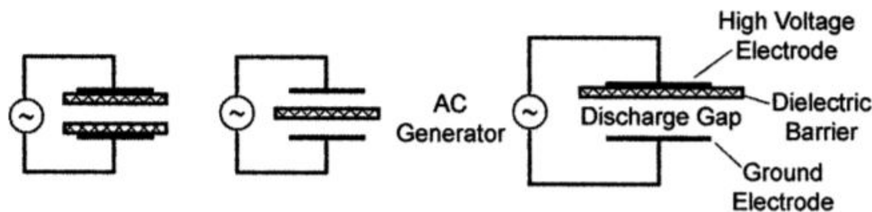

Figure 3.6: Basic DBD configurations[45].

For a conventional remote plasma, the pressure, p, is typically between 1-10 torr and the distance, d, is between 1-10 cm. When adapted for an atmospheric SDBD source, as the pressure is 760 torr (= 1 atm), the distance between the source and the substrate can and should be reduced to 100-200 μm. The different regions of operation for values of p and d for conventional vacuum and low pressure plasma and atmospheric plasma are shown in figure 3.5.

Figure 3.7[1] shows a rough schematic of a similar plasma source. In this project work, the plasma was created using nitrogen for one set of experiments (chapter 4) and using hydrogen and nitrogen for another set of experiments (chapter 5). For the experiments

[1]The exact representation has been withheld by the designer. This image is used as the best replacement.

with nitrogen plasma, the co-reactant, water, is fed through the channel in the center (plasma down flow).

Figure 3.7: Schematic of the SDBD plasma source used in this study.

Nitrogen is fed through one of the side channels (marked 1). The electric field is applied to the electrodes shown in red and plasma is produced on the bottom side of the dielectric. The second channel on the side (marked 2) was not used as it was damaged at the time of this experimentation. For the experiments with hydrogen plasma, both water and hydrogen were fed through the plasma top flow channels 1 and 2. The gap between the source and the substrate is 200 μm. Several reactions occur in the plasma source. A few of the most important ones are listed below (equations 3.1, 3.2, 3.3 and 3.4). H^+, $OH^{\cdot}$, $O^{\cdot}$ and OH are of interest as there is a high chance of their incorporation in the thin-film as dopants. Ammonia, a by-product, is vented through the exhaust outlet.

$$e^- + H_2O \rightarrow H^+ + OH^{\cdot} + 2e^- \tag{3.1}$$

$$e^- + H_2O \rightarrow {H_2}^+ + O^{\cdot} + 2e^- \tag{3.2}$$

$$OH^{\cdot} + e^- \rightarrow OH^- \tag{3.3}$$

$$H^+ + {NH_2}^- \rightarrow NH_3 \tag{3.4}$$

3.2. Characterization

3.2.1. Spectroscopic ellipsometry

Spectroscopic ellipsometry is an optical technique that can be used to measure the thickness of a sample. An ESM 300 system by J. A. Woollam Co. has been used to measure the thickness of the samples in this work. The working principle of the equipment is as follows. A linearly polarized beam of light is incident on the sample. Upon interaction with the thin film deposited on the substrate, the polarization of the light changes and it is reflected. This change in polarization is detected and used to characterize the sample. A schematic of the principle is shown in figure 3.8.

The change in polarization is characterized by (Ψ) and (Δ) and they are related as shown in equation 3.5 [47],

$$\tan(\psi).\exp(i\Delta) = \frac{r_p}{r_s} \quad (3.5)$$

where r_p is the reflectivity for the p-polarized light and r_s is the reflectivity for the s-polarized light. ψ is the magnitude and Δ is the phase difference. The method is precise as it is independent of absolute intensity and only depends on a ratio. The values of ψ and Δ are measured at each wavelength across the spectral range of the equipment.

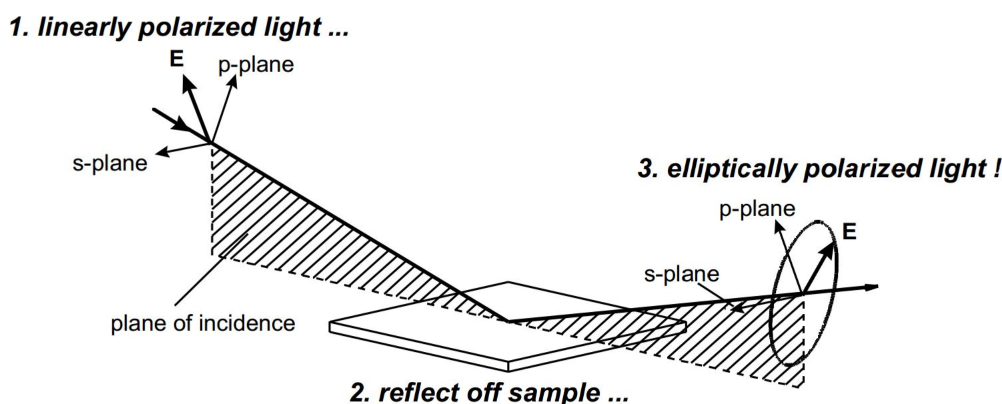

Figure 3.8: Principle of SE [47].

Once the data have been obtained, they must be fitted using an optical model. Cauchy's model in the visible wavelength range (400-750 nm) was used to fit the data for the samples in this work. The mean square error (MSE) is an indicator of how well the data can be fit. Models can be used to predict the thickness, roughness and the complex refractive index and the extinction coefficient of a deposited film, among many other properties [47].

3.2.2. Spectrophotometry

A spectrophotometer is an apparatus that, among other things, can measure the reflectance, transmittance and absorbance of a material as a function of wavelength. In this research, a Cary UV/Vis/NIR 5000 system from Agilent was used in the spectral range of 300 to 1800 nm. As shown in figure 3.9, a dispersion device or a monochromator splits the incident light from the source such that the sample can be exposed to a particular wavelength. The sample, depending on where it is placed, either transmits or reflects incident light. Since a lot of the light is scattered, an integrating sphere, as shown in figure 3.10, is used to collect and measure the intensity of the light. It is more accurate than the standard photoelectric detector where most of the light is lost [48]. The absorbance can be calculated using Kirchhoff's law (equation 3.6)

$$T + R + A = 100\,\% \tag{3.6}$$

where T is the transmittance, R is the reflectance and A is the absorbance in percentage.

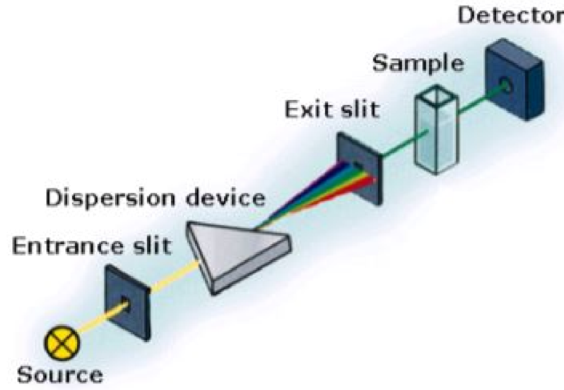

Figure 3.9: Schematic of the spectrophotometry principle [49].

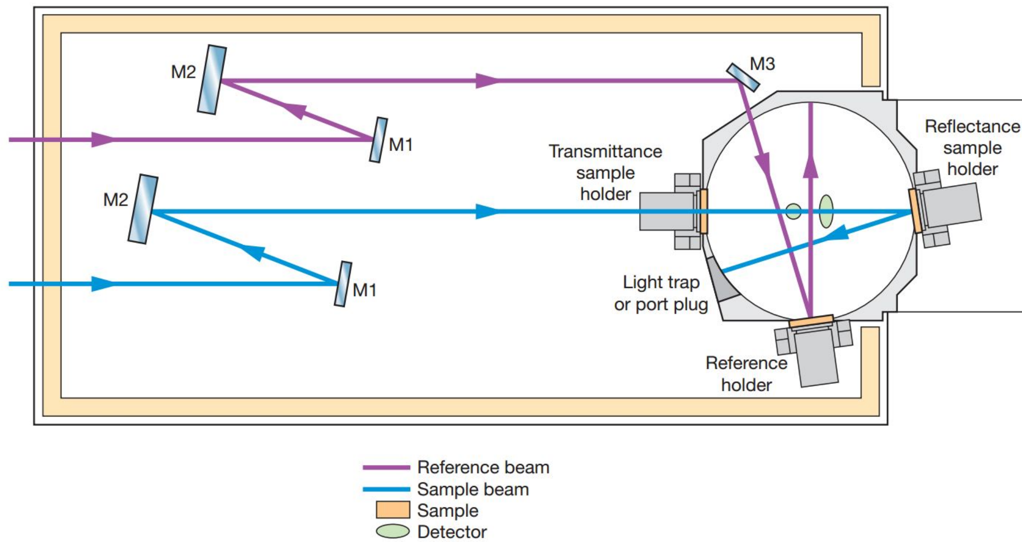

Figure 3.10: Schematic of the integrating sphere [48].

According to Beer-Lambert's law,

$$I(d) = I_o \exp(-\alpha d) \tag{3.7}$$

where α is the absorption coefficient, I(d) is the transmitted intensity, I_o is the incident intensity, d is the thickness of the sample in m.

From equation 3.7, we can derive:

$$\alpha = \frac{1}{d}\log(\frac{I}{I_o}) = 2.303\frac{A}{d} \tag{3.8}$$

The absorption coefficient thus obtained can be used to calculate the optical bandgap of the material from equation B.1 with the help of a Tauc plot (see Appendix B) [50],

$$\alpha h\nu = A(h\nu - E_g)^m \tag{3.9}$$

where h is Planck's constant, ν is the frequency in Hz and E_g is the optical bandgap of the material in eV. The value of m depends on the kind of electronic transition. Extrapolation of the linear region in a Tauc plot will give the optical bandgap of the material being studied [50].

3.2.3. Hall Setup

A Hall setup has been used to measure the electrical properties; i.e., the mobility of charge carriers, the resistivity and the carrier density of the TCO. The equipment used for this thesis was an Ecopia HMS 5000 system.

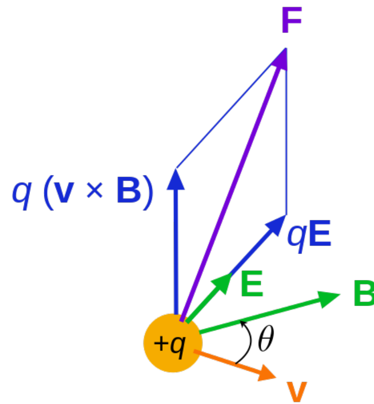

Figure 3.11: The Lorentz force [51].

The working principle of the setup is based on the Lorentz force: when an electric charge moves with a velocity along an electric field in the presence of a magnetic field, it experiences a force (figure 3.11). In an n-type semiconductor, this leads to all the electrons shifting to one side causing a potential drop, called the Hall voltage (V_H). The sheet carrier density (n_s) can then be determined by the equation 3.10 [52],

$$n_s = \frac{IB}{e|V_H|} \tag{3.10}$$

where I is the current in A, B is the magnetic field in T and e is a unit charge (1.6 x 10^{-19} C). The bulk density n can be easily calculated as in equation 3.11, where d is the thickness of the sample in m.

$$n = n_s/d \tag{3.11}$$

The resistivity of the sample is determined using the Van der Pauw technique. It is used for thin, uniform samples that can be arbitrarily shaped but are continuous films. Two characteristic resistances, R_A and R_B, are related to the sheet resistance R_S as in equation 3.12 known as the Van der Pauw equation [52]. The sheet resistance is measured in $\Omega/\square$.

$$\exp\left(\frac{-\pi R_A}{R_S}\right) + \exp\left(\frac{-\pi R_B}{R_S}\right) = 1 \quad (3.12)$$

This equation can be solved numerically for R_S. The resistivity can then be calculated as shown in equation 3.13. Once the sheet resistance and carrier density are known, the mobility μ can be calculated in $cm^2/V.s$ using equation 3.14 [52].

$$\rho = R_S d \quad (3.13)$$

$$\mu = \frac{V_H}{R_S I B} \quad (3.14)$$

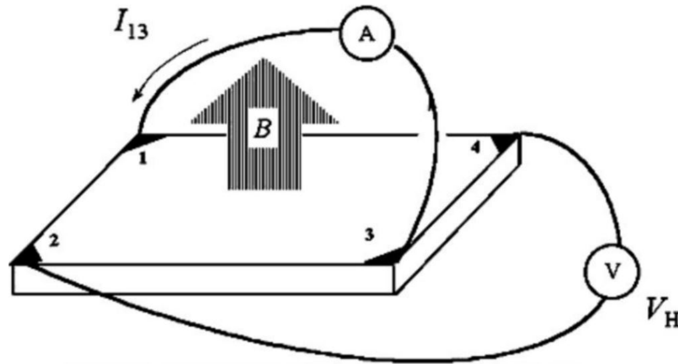

Figure 3.12: The Van der Pauw configuration for measuring the Hall voltage [52].

In the Van der Pauw configuration, the Hall voltage, V_H, is measured with a constant current and magnetic field applied perpendicular to the plane of the sample. Current is passed through two opposite corners and the induced voltage is measured across the remaining two as shown in figure 3.12. It is important to ensure that the power dissipated in the sample does not exceed the maximum value. The limit is calculated using equation 3.15,

$$I < \frac{1}{\sqrt{200R}} \quad (3.15)$$

where R is the resistance in Ω between two opposite contacts.

Eight measurements of voltage are made and for a uniform sample, the voltage between two opposite contacts should be the same. Errors caused due to the sample shape or improper connections can be compensated for by measuring the voltage with both, a positive and negative magnetic field [52].

In this research project, the deposited samples were cut to the size of 1 cm x 1 cm and measured directly. Each sample was measured multiple times in the same position without moving it to check for consistency.

3.2.4. Four-point probe

The resistivity and hence, the sheet resistance of a semiconductor material is an important property that affects the voltage, capacitance and series resistance of the material. It depends on the doping level and the nature of the semiconductor. In this research, a Keithley 2611A system was used to measure the sheet resistance of the thin-film samples. A four-point probe consists of four colinear probe needles. The outer probes source the current and the voltage is measured using the inner probes connected to a high-impedance voltmeter [53]. The schematic is shown in figure 3.13

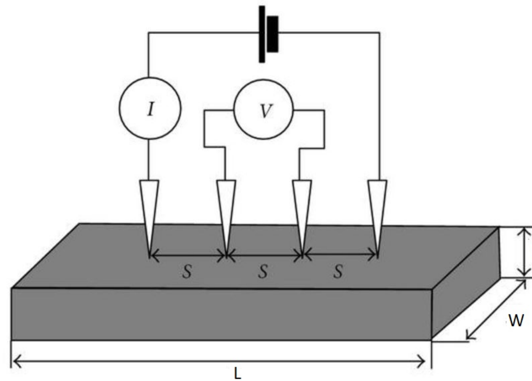

Figure 3.13: Schematic of a four point probe system [54].

If a semiconductor bar is modeled as a resistor,

$$J = \sigma E \tag{3.16}$$

where J is the current density in A/m^2, σ is the conductivity in $(\Omega.m)^{-1}$ and E is the electric field in V/m.

$$\rho = \frac{1}{\sigma} \tag{3.17}$$

where ρ is the resistivity in (Ω.m).

$$J = \frac{I}{Wt} \tag{3.18}$$

and

$$E = \frac{V}{L} \tag{3.19}$$

where I is the current in A in the direction of L, V is the voltage drop in volts, W is the width of the semiconductor, L is the length and t is the thickness, all in m [55].

From equations 3.16, 3.18 and 3.19, we can derive,

$$V = I\rho\frac{L}{Wt} = IR \tag{3.20}$$

If the sample is square in shape, the equation becomes,

$$R = \frac{\rho}{t} \equiv R_S = \frac{V}{I} \tag{3.21}$$

For a sample that is arbitrarily shaped, a correction factor is used to modify equation 3.21 [56].

$$R_S = \frac{\pi}{\ln(2)}\frac{V}{I} = 4.53\frac{V}{I} \tag{3.22}$$

Each sample was measured at nine points on the thin film sample. The sheet resistance is typically expressed as $\Omega/\square$ to avoid confusion with the value of resistance measured in Ω.

3.2.5. X-ray diffraction

X-ray diffraction is used to study the crystalline structure of a material. When a beam of monochromatic X-rays, typically Cu $K\alpha$ radiation with a wavelength of 0.154 nm, is incident on a crystalline material, it is reflected by the atoms of the crystal. These reflected rays can interfere either constructively or destructively (diffraction). The intensity and direction of these rays are detected. According to Bragg's law, this phenomenon is described by the following equation 3.23 [57],

$$n\lambda = 2d\sin\theta \tag{3.23}$$

where λ is the wavelength of the incident X-rays in nm, θ is the angle of incidence of the rays in degrees, d is the distance between atoms in m, and n is an integer. Bragg's law states that the interference is constructive when n is an integer because the waves are in phase and is illustrated in figure 3.14 [57].

A polycrystalline material is composed of several small crystals that are usually randomly oriented. Here, all the possible orientations can be detected by changing the angle of incidence θ. Constructive interference results in a strong intensity of the reflected light, a peak, at precise angles. Every material has its characteristic peaks at specific

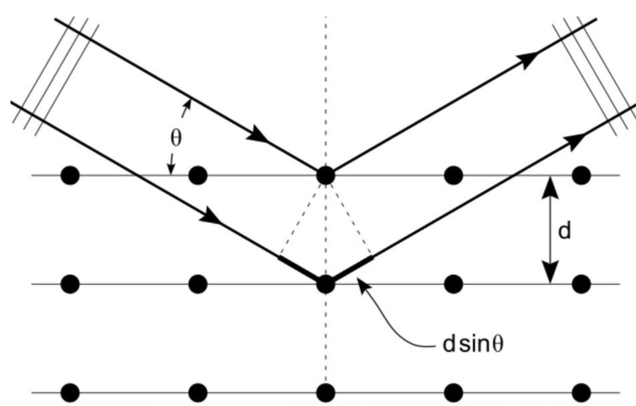

Figure 3.14: Bragg's law [58].

angles and this information can be used to identify the material and to study its structure. The intensity of the peak is also an indicator of the degree of crystallinity and the preferred orientation [57].

In this work, a Panalytical X'Pert MPD Pro diffractometer with a long fine focus Cu anode was used as an X-ray source for λ = 0.154 nm in the range of 5° and 90° of 2θ.

3.2.6. Scanning Electron Microscopy (SEM)

Scanning Electron Microscopy (SEM) is a technique used to study properties such as the morphology, crystalline structure, orientation of crystals, etc. of a solid sample. A beam of high-energy electrons (0.2 keV to 40 keV), generated thermionically in an electron gun, is focused onto the surface of the sample. The beam passes through scanning coils, which deflect the beam in the x and y-axes such that the sample is scanned as in a raster. The energy of these electrons is dissipated in the sample as they interact with the material. This energy produces secondary electrons, back scattered electrons (BSE), photons and heat, each of which is detected by a detector. Secondary electrons and the BSE are the most useful for imaging. Secondary electrons provide information about the morphology of the sample as they are emitted by the atoms near the surface while the BSE, which are the result of an elastic collision between incident electrons and the material, provide information about the composition in multi-phase samples. When incident electrons collide inelastically with electrons in the sample, X-rays are generated. Each element has its characteristic wavelength which can be used to detect the element's presence in the material. In a conventional SEM system, the entire setup is under vacuum. It is a non-destructive characterization technique and can be performed multiple times on the same sample [59]. Figure 3.15 shows a schematic of the SEM setup.

SEM, unlike an optical system, is not limited by the resolution of the lenses used. The resolution in a SEM depends on the size of the electron spot and the volume of interaction. This allows for very high-resolution images (500,000x) in comparison to a light microscope which is limited by optics.

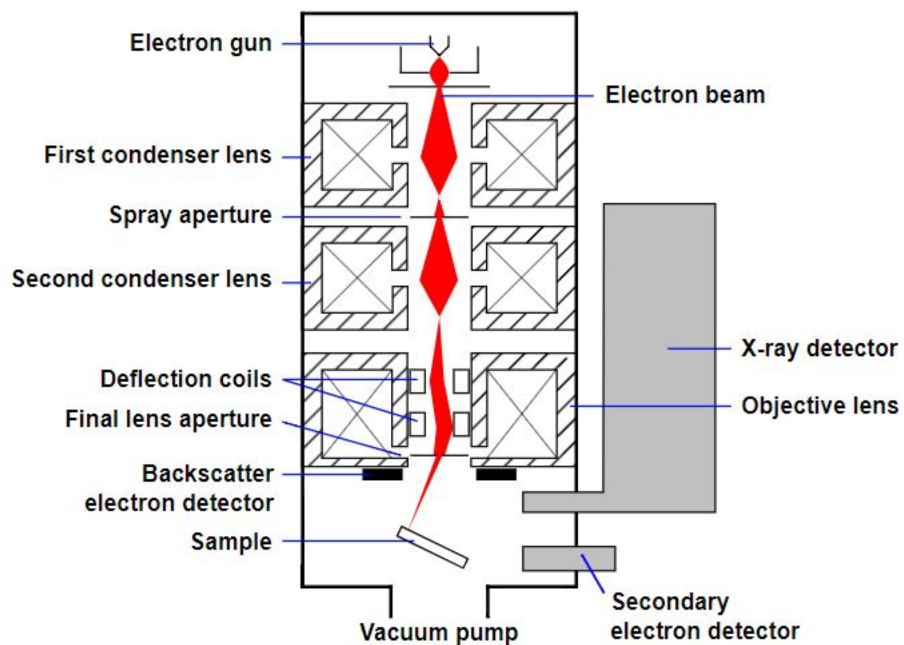

Figure 3.15: Schematic of a SEM setup [60].

In this project, a NovaNanoSEM 600 FE-SEM system from FEI, with an Oxford Xmax 80 EDX detector was used to characterize the thin films deposited on glass. The films were coated with carbon before the imaging to provide a path for the electrons to ground and prevent sample charging that reduces the contrast in the SEM images.

4

Deposition of hydrogen-doped indium oxide thin films using N_2 plasma

4.1. Introduction

In this chapter, the process window for depositing IO:H thin films using N_2 plasma has been explored. The films were then characterized and their structural, optical and electrical properties will be discussed. The following research questions have been answered in this chapter.

1. Is it possible to develop an ALD process using the plasma enhanced spatial ALD technique?
2. What are the conditions required to deposit IO:H thin films successfully using this technique?
3. What is the influence of temperature on the structural, optical and electrical properties of the films?

4.2. The ALD process window

The reaction rate in any chemical process is dependent on several factors, namely, the concentration of the reactants, activation energy, temperature, etc. In addition to the factors mentioned, the film growth rate in ALD is also dependent on the incident fluxes of reactive species and the sticking probability. The sticking probability, as the name suggests, is the likelihood that a reactant will adsorb or attach onto the surface of a substrate. The relation between sticking probability and the incident flux is given by equation 4.1,

$$R_{ads} = S * F \tag{4.1}$$

where R_{ads} is the rate of adsorption, S is the sticking probability and F is the incident flux on the substrate [61]. The incident flux remains the same throughout the process while the sticking probability reduces as the number of sites available on the substrate decrease as the reaction progresses. Figure 4.1 shows a typical plot of the growth per cycle (GPC) versus temperature. In an ideal reaction, at a certain point, R becomes zero and the curve becomes flat. This is the saturation region. The region between T_1 and T_2 is the ALD window, ideal for operation.

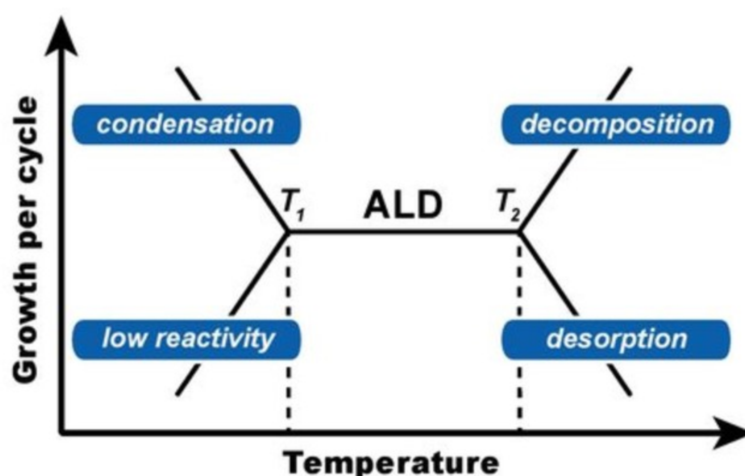

Figure 4.1: A typical plot of growth per cycle (GPC) versus temperature. The region between T_1 and T_2 is called the ALD process window [62].

Outside the ALD process window, several phenomena occur. A brief overview of these is discussed below.

Condensation

At low temperatures, some reactants or the fragments thereof may condense on the substrate. This may induce a CVD type reaction between the precursors. CVD reactions are not self-limiting and lead to a higher GPC than pure ALD reactions.

Decomposition

At high temperatures, it is possible that a precursor starts to decompose due to the thermal budget provided. This may again lead to CVD type reactions and to an increase in the GPC. TMI decomposes at 250 °C [36]. For this reason, experiments in this work were limited to a maximum of 225 °C.

Low reactivity

ALD reactions are thermally activated and at low temperatures, the reactivity of the precursors may be critically low. This leads to a low GPC. From the available literature (see section 2.1), it is known that the reaction between TMI and water is slow. Increasing the

temperature may lead to an increase in the reactivity of the precursor. This is discussed in detail in section 4.3 of this chapter.

Desorption of species

At high temperatures, adsorbed species or functional surface groups on the surface sites may desorb, if the thermal energy provided exceeds the energy required to keep the species bonded/adsorbed on the substrate. This leads to a decrease in the overall GPC of the reaction.

4.2.1. Non-ideal effects in ALD

In a perfect ALD reaction, each surface site that is available is occupied by the reactant forming a monolayer. However, perfect ALD reactions are not very common. If a precursor molecule is too large due to the presence of bulky ligands, it may block adjacent potential sites or may inhibit reaction with the second precursor. This is known as *steric hindrance*. In some cases, steric hindrance may cause delayed reactions [63].

The other possible reasons for non-uniform or rough layers are diffusion, the presence of defects, nucleation effects, etc. Thin-film depositions are governed by the interaction forces between adatoms and the surface sites. If the adatoms are attracted to the substrate more strongly than they are to each other, a uniform two-dimensional growth mode, known as Frank-Van der Merwe mode, is highly likely. If the adatom-adatom attraction is stronger than adatom-surface attraction, it leads to the formation of islands on the substrate. The Stranski-Krastanov growth mode is a combination of the 2-D growth and the island growth mechanisms and more common than either the 2-D or the island growth mode. The transition from smooth to rough layers occurs at a critical thickness that depends on the physical and chemical properties of the layer and the substrate. Figure 4.2 shows all three growth models for thin films [64].

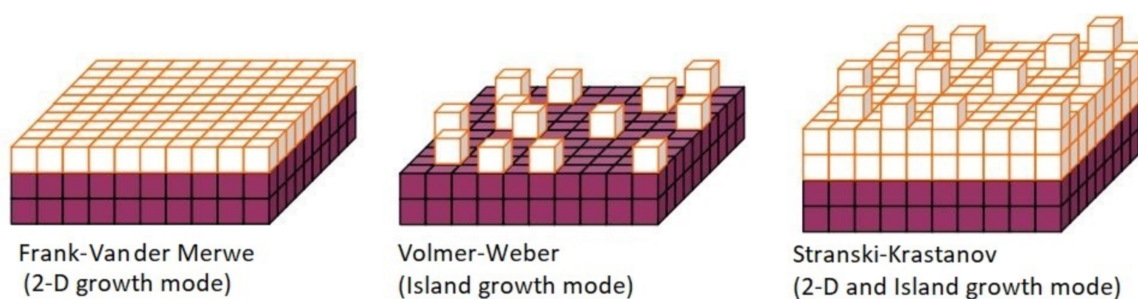

Figure 4.2: Schematic of the different growth models for thin films.

The key parameters that influence the film growth are the strain due to lattice mismatch which affects the interfacial energy and the surface free energies for the substrate and the material being deposited. Equation 4.2 shows the relation between the two. Here, γ_A and γ_B are the surface free energies and γ_i is the interfacial energy. If $\Delta\gamma$ is negative,

the growth is 2-D. At a critical thickness, $\Delta\gamma$ becomes positive and the Stranski-Krastanov growth mode will be preferred [64].

$$\Delta\gamma = \gamma_A + \gamma_i - \gamma_B \tag{4.2}$$

4.3. Process parameters

Some of the key parameters that influence the deposition process are the concentrations of the precursor (TMI) and the co-reactant (water), the exposure time of the substrate to the precursors and the temperature. To answer the first two research questions mentioned in section 4.1, each of these parameters and its effect on the process needs to be studied. The effect of each of these parameters on the growth rate of the film was studied. The purpose of these experiments was to obtain an idea of the most suitable values of these parameters. A combination of these will then be used to conduct further analysis.

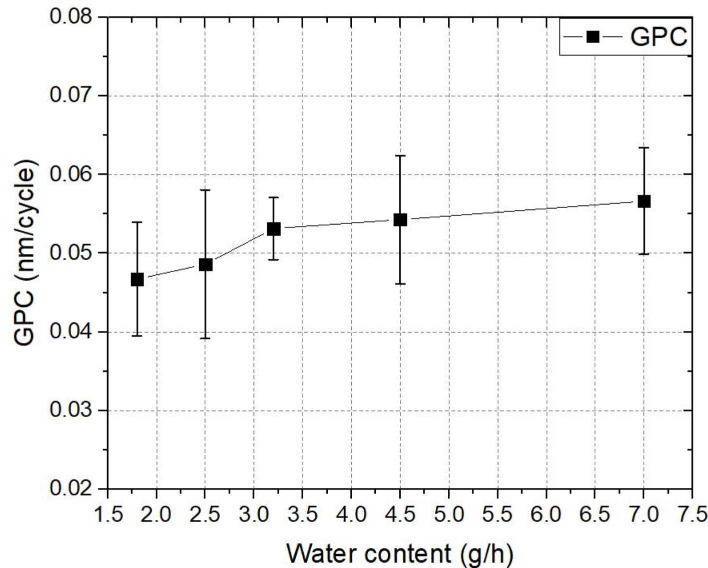

Figure 4.3: The growth per cycle versus water content. The rotation speed of the substrate table was maintained at 20 rpm and the temperature at 150 °C. TMI flow was 150 sccm.

The effect of changing water content on the growth rate is shown in figure 4.3. It can be seen that increasing the water content increases the growth rate and approaches saturation. As the highest growth rate is seen for the flow rate of 7 g/h, for all further experiments with N_2 plasma, the same has been used.

The films deposited using a rotary s-ALD machine have the shape of a donut as shown in figure 4.4. It means that at a particular rotation speed, the exposure of the substrate to the precursors decreases as the radius increases. In figure 4.4, the area marked as 1 is exposed to the precursors for a longer time than area 3. A pie-shaped injector that is designed to geometrically compensate for this difference is used. While the injector

for TMI is pie-shaped, the shape of the plasma source used is linear introducing a radial dependence of the deposition rate. The exposure of the substrate to water may be insufficient at a high rotation speed. Table 4.1 shows the exposure time of the substrate for different positions and different speeds.

Table 4.1: Exposure time at different positions for different rotation speeds.

Speed (rpm)	Exposure time (ms)		
	3 cm	4 cm	5 cm
40	115	75	50
20	225	150	100
10	450	300	200

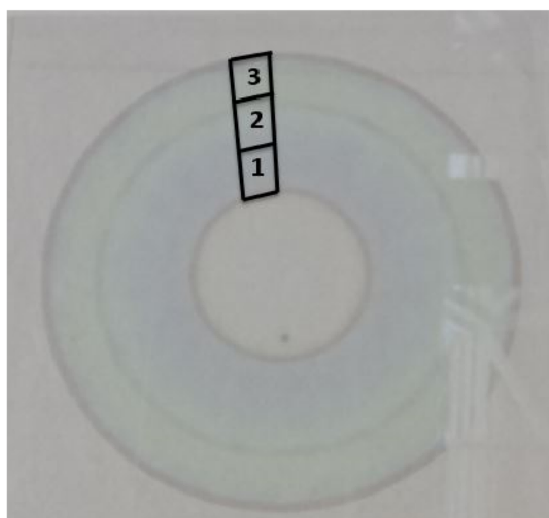

Figure 4.4: Photograph of the sample with the different areas marked out. Area 1 is approximately 3 cm, Area 2 is 4 cm and Area 5 is 5 cm from the centre of the donut.

The growth rates for all the positions versus their respective exposure times are shown in figure 4.5. It is seen that at 40 and 20 rpm, the growth rate across the film is not uniform, implying that the exposure time is insufficient. At 10 rpm (corresponding to 450 ms, 300 ms and 200 ms in figure 4.5), the growth rates match closely as the process approaches saturation. While using lower speeds (such as 7 or 5 rpm) may further improve the growth rate, it will make the process too slow rendering it less practical. Thus, all the samples made using nitrogen plasma have been prepared at 10 rpm, unless otherwise stated.

From previous experiments performed at TNO, it was ascertained that a flow rate of 150 sccm of TMI is sufficient to drive the reaction to saturation. This was also confirmed

with the current settings of water flow and speed.

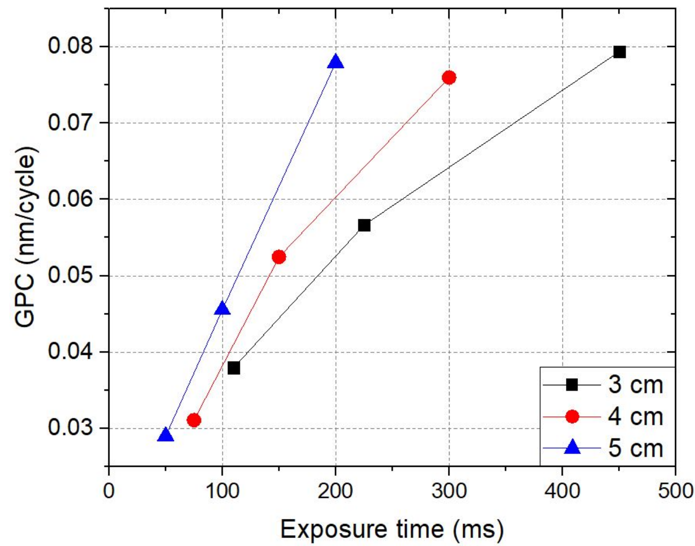

Figure 4.5: The growth per cycle versus exposure time corresponding to rotation speeds of 40, 20 and 10 rpm. The temperature was maintained at 150 °C, TMI flow was 150 sccm and the water flow was 7g/h.

4.4. The ALD process window using N_2 plasma

ALD is a thermally driven reaction, and hence the effect of temperature on the properties of the layer is one of the most important characteristics to be studied.

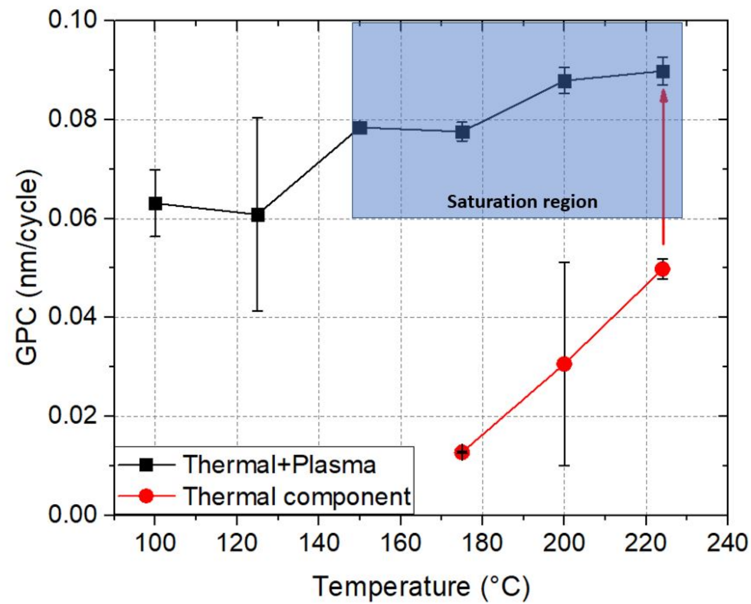

Figure 4.6: The growth per cycle versus temperature. The samples were deposited at 10 rpm, with 7 g/h water flow and 150 sccm of TMI.

Figure 4.6 shows a plot of the growth rate versus the deposition temperature. The black markers (■) represent the growth rate when the reaction is enhanced by plasma and the red markers (●) show only the thermal component of the reaction, i.e., no plasma was used. Increasing the temperature steadily improves the rate of growth when no plasma is used. Despite this, the growth rate is low, and little or no growth is observed below 175 °C. When the reaction is enhanced by plasma, the growth rate, at 225 °C, almost doubles from 0.045 to 0.09 nm/cycle. It could be due to the increased availability and reactivity of species such as $OH^{-}, H^{+}, O^{\cdot}, H^{\cdot}$, etc. Plasma also increases the local temperature of the substrate surface by 4-5 °C, which may add to the higher growth rate. Apart from increasing the rate of reaction, plasma also enables deposition of the thin films at lower temperatures (100 °C and 125 °C). Plasma, in effect, opens up the process window and the thermal component becomes significant at temperatures above 175 °C. Beyond 150 °C, increasing the temperature, increases the GPC only slightly from 0.08 nm/cycle to 0.09 nm/cycle, indicating a region of saturation (shown in the blue region in figure 4.6) within practical limits. This is the ALD process window and further investigation into the layers developed at these temperatures has been carried out.

4.5. Film thickness uniformity

The uniformity of a TCO layer is important because the thickness affects layer properties such as resistivity and carrier density. The thickness uniformity of the samples can be calculated using equation 4.3 [65].

$$\text{Non-uniformity} = \frac{\text{Maximum(d)} - \text{Minimum(d)}}{2 * \text{Average(d)}} \tag{4.3}$$

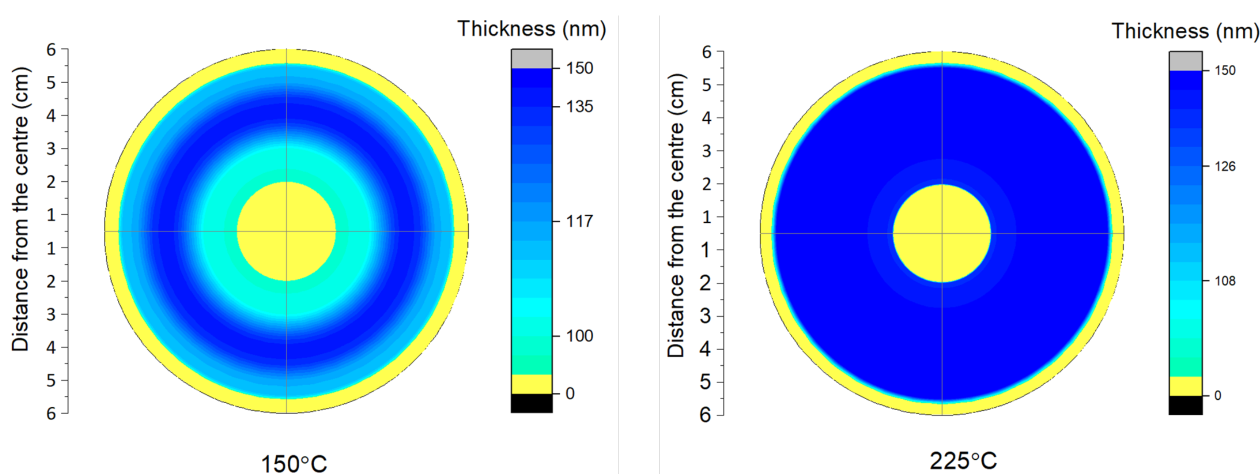

Figure 4.7: Thickness uniformity for samples grown at 150 °C and 225 °C.

Using the growth rate obtained in figure 4.6, the thin films were grown to a thickness of ~ 140 nm. For the sample deposited at 150 °C, the uniformity was 85 % for an area

of 50 cm^2 while for that deposited at 225 °C, it was 97 % for the same area. Figure 4.7 shows the non-uniformity observed. This difference may be ascribed to the improved reactivity of the radicals at higher temperatures leading to a more homogeneous layer. The flow of the plasma gas is complex and depends on several factors one of which may be temperature. The increased reactivity of TMI itself at higher temperatures may also be one of the causes.

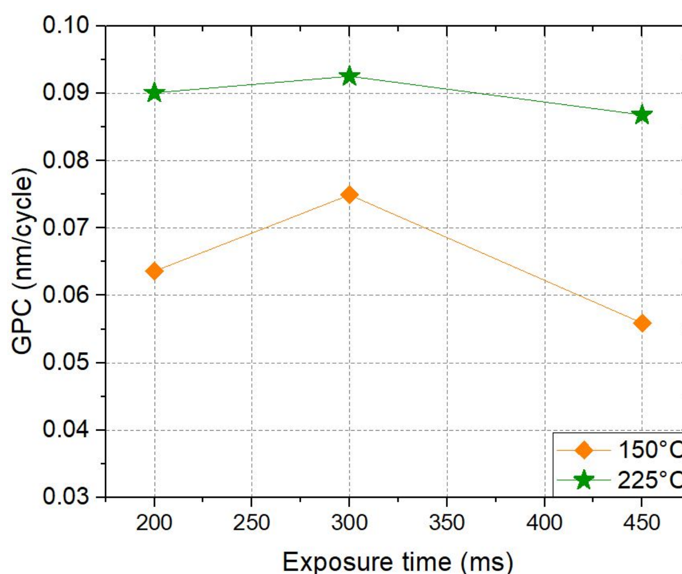

Figure 4.8: Thickness uniformity shown in a GPC versus exposure time graph.

Figure 4.8 shows the difference in thickness at different positions on the substrate. This figure also shows that the thickness uniformity improves with an increase in temperature. This is because at low temperatures, reactivity of TMI and water is low making plasma an important factor. At higher temperature, the plasma component and the thermal component contribute, rendering the film thickness more uniform.

4.6. Structural Properties

The structure of a material defines properties such as conductivity and mobility. The structural properties of the IO:H films were investigated using the X-ray diffraction (XRD) technique. The intensity of the reflected X-rays is plotted against the incident angle 2θ. To study the effect of the deposition temperature, the XRD spectra of thin films deposited at 150 °C, 200 °C and 225 °C are plotted against the incident angle as shown in figure 4.9. The bottom-most graph of the stack shows the XRD data for a standard sample of In_2O_3, i.e., a powdered sample with random grain orientations with data obtained from the Crystallography Open Database (COD) card number 1010341 [66]. The most prominent orientations are (222), (400), (440) and (622) with their diffraction peaks at 30°, 35°, 50° and 60°, respectively.

The data were normalized to provide a fair comparison of the preferred orientation of

the grains. It is evident from the graph that all the samples are highly crystalline. The concentration of each component producing the intensity is directly related to the respective peak intensity [67]. By normalizing the peaks of the layers deposited, it is seen that the (222) orientation has a slight preference but presence of the other peaks matching with the reference sample shows that the crystal orientations have some degree of randomness. For the IO:H thin films deposited by temporal ALD, similar results were observed for deposition temperatures above 150 °C using InCp [11, 21].

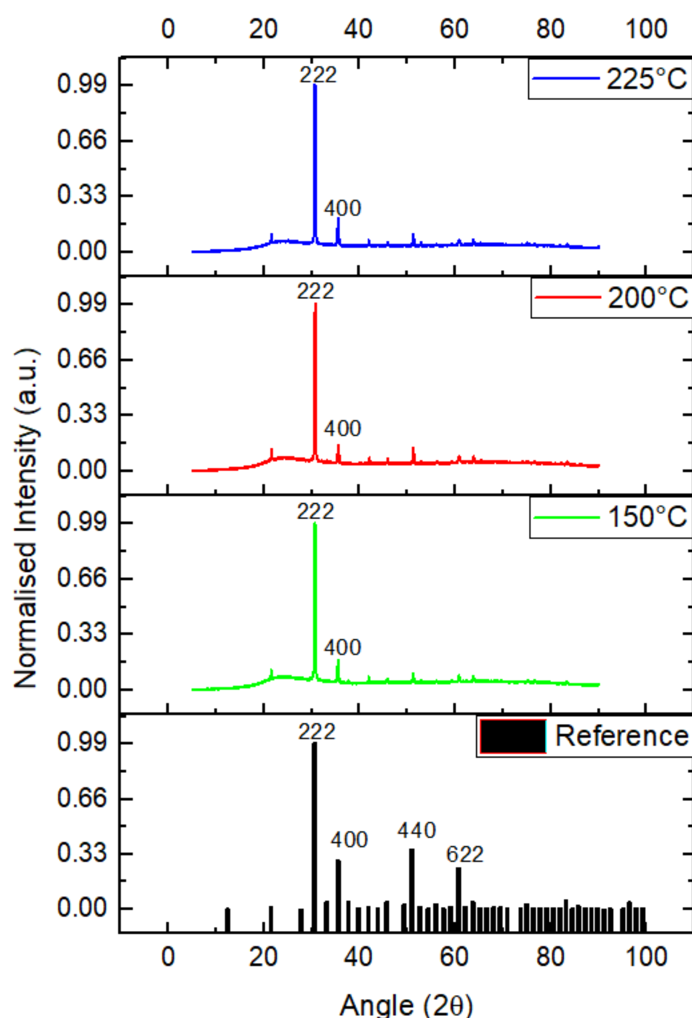

Figure 4.9: XRD patterns for the films deposited at 150 °C, 200 °C and 225 °C. Layer thickness ~ 140 nm.

Table 4.2 shows the approximate size of the crystals with the orientation (222), in the direction perpendicular to the surface of the substrate. The crystal size was calculated using the Debye-Scherrer equation (equation 4.4), where, D is the average crystal size, K is a constant (0.94), λ wavelength of Cu Kα, β is the full width at half maximum (FWHM) of the peak and θ is the incident angle [68].

$$D = \frac{K\lambda}{\beta \cos\theta} \tag{4.4}$$

The Scherrer method assumes that the crystal is spherical. However, that may not be the case. It is possible that the size represents a group of crystals with the same orientation. The particle size increases only marginally with increasing temperature implying that beyond 150 °C the effect of temperature on the crystal size is negligible unless a very high thermal budget is provided to the material to change it.

Table 4.2: Approximate size of the crystallites in the IO:H film

Temperature (°C)	**Peak position (2θ)**	**FWHM**	**Particle size (nm)**
150	30.67	0.24	42.3
200	30.70	0.24	44.3
225	30.69	0.22	45.56

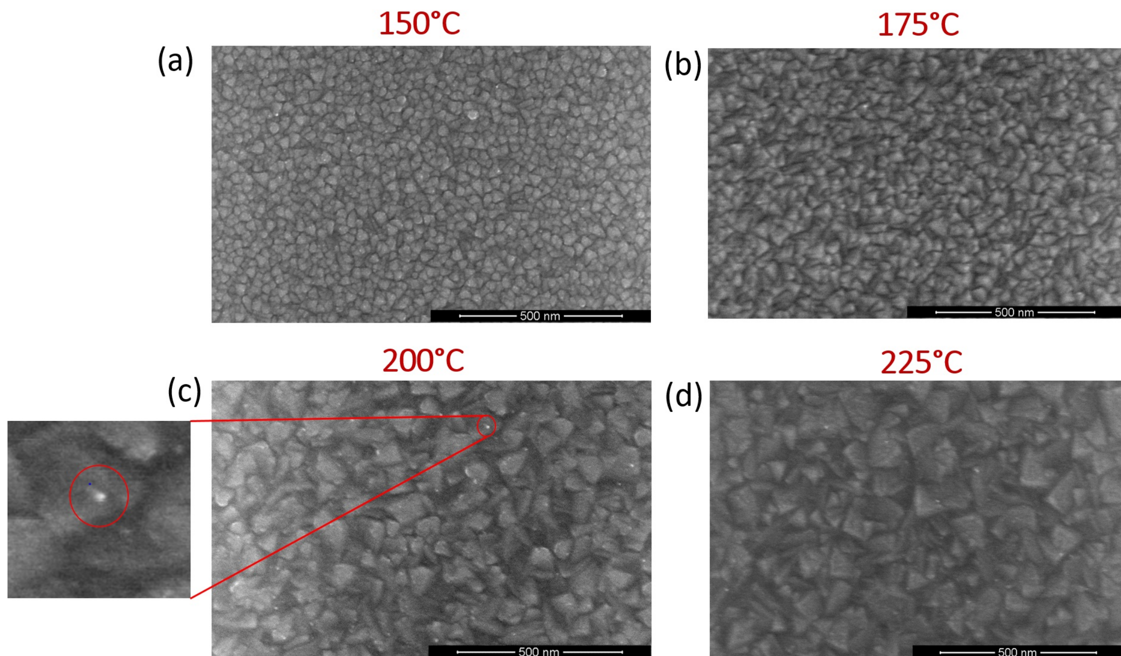

Figure 4.10: Top-view SEM images of the layers deposited at (a) 150 °C, (b) 175 °C, (c) 200 °C and (d) 225 °C. The white speck as shown in the zoom inset to the left of figure 4.10c may indicate embedded crystallites.

A top-view SEM analysis was performed to study the morphology of the layer in the direction parallel to the surface of the substrate. Figure 4.10 shows the images obtained from the SEM analysis of IO:H films deposited at (a) 150 °C, (b) 175 °C, (c) 200 °C and (d) 225 °C. From the image, it is clear that an increase in the temperature leads to an increase in the grain size laterally. The material is densely packed. With an increase in temperature and increase in grain size, the number of grain boundaries decreases. The component of

scattering that arises from grain boundaries is, thus, likely to reduce. The lateral grain size for the layer deposited at 150 °C is 25-50 nm while at 225 °C it ranges between 55-125 nm. This change reflects clearly in the electrical properties of the material. The white speck (as shown in the zoomed in image to the left of figure 4.10c) could indicate embedded crystallites. The growth of indium oxide layers in this way has been observed by Macco *et al.* [21]. During the growth of the layer, nucleation of these crystallites occurs at a certain thickness. These embedded crystallites act as seeds for the further development of the crystals as the thickness increases. Figure 4.11 shows a growth model for this type of growth. The nucleation occurs in an amorphous incubation layer. These crystallites then continue to grow into larger crystals.

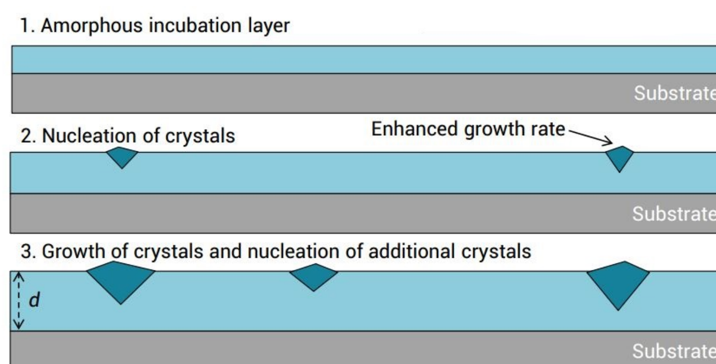

Figure 4.11: Schematic showing the nucleation and growth of the crystallites [21].

4.7. Optical Properties

The optical properties of a TCO are one of the most important parameters to be studied. However, ascertaining optical constants is not easy due to three main reasons: (a) variation of the free carrier absorption with carrier concentration, (b) a shift of the band edge absorption with carrier density and (c) dependence of transparency on thickness [69]. The optical properties of the IO:H films deposited at different temperatures were measured using spectrophotometry.

The reflectance (R) and transmittance (T) as a function of wavelength are shown in figure 4.12 while the absorption is shown in figure 4.13. The deposition temperature is denoted in the legend of the plots. Transparency values of around 90 % are observed for all the layers in the visible region of the spectrum. Increasing the temperature has little effect on the transparency of the layers. A slight blue shift is observed for the film deposited at 200 °C. In the visible region, 400 nm-750 nm, samples deposited at lower temperatures (150 and 175 °C) have a lower reflection than those deposited at higher temperatures. In the infrared (IR) region, however, this changes and the reflection from samples deposited at lower temperatures increases slightly. Though the absorption for all the layers is below 10 %, there is still an increase in absorption with an increase in temperature. The blue shift observed may be explained by the Burstein-Moss shift which

occurs in degenerate semiconductors when the apparent optical bandgap increases due to the non-availability of free energy states in the conduction band. The Fermi level shifts into the conduction band, increasing the apparent bandgap of the material [69]. However, the carrier density has been shown to vary significantly with exposure time and temperature (see section 4.8) and hence, drawing absolute conclusions, in this case, is difficult.

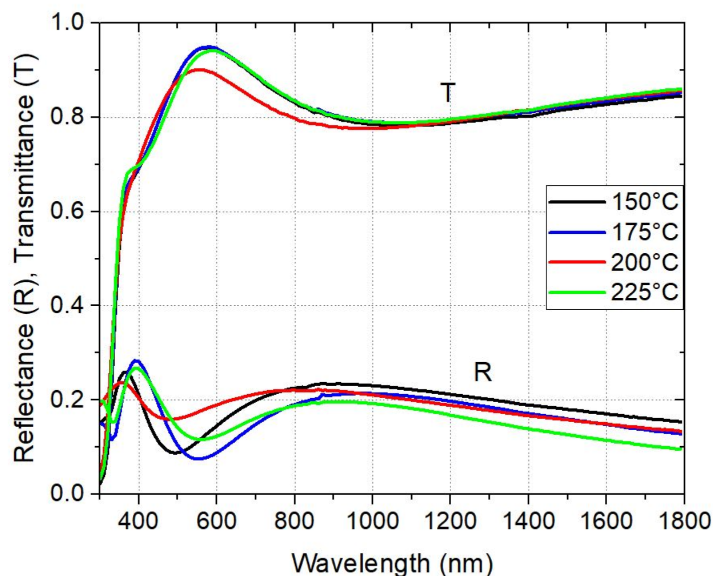

Figure 4.12: Transmission and reflectance of the IO:H films grown at different temperatures. Film thickness ~ 140 nm.

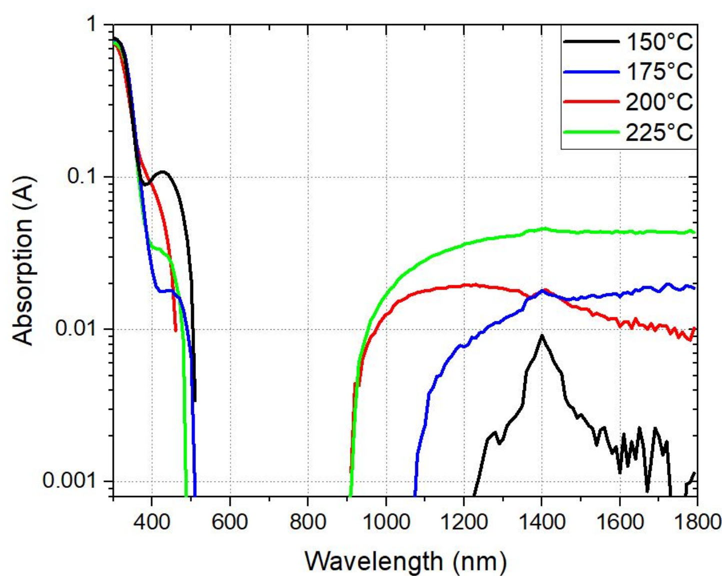

Figure 4.13: Absorbance of the IO:H films grown at different temperatures. Film thickness ~ 140 nm.

The optical bandgap of IO:H can be determined using the so-called Tauc plot which makes use of the absorption coefficient. This can be calculated using equation 3.8. In a plot of $(\alpha h\nu)^{1/\mathrm{m}}$ versus the photon energy, if the linear part of the curve is extrapolated, the intercept of the tangent on the x-axis gives the bandgap. For the layers deposited in this work, the bandgap is around 3.75 eV, which is in good agreement with the values observed for crystalline IO:H layers in literature [21]. This high bandgap allows for a high transparency in the visible and near infrared (NIR) region of the wavelength spectrum.

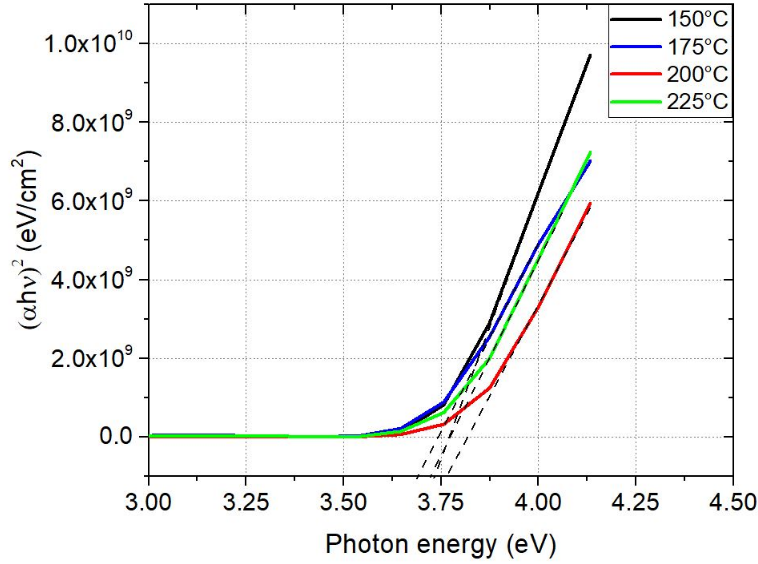

Figure 4.14: Tauc plots of the IO:H films deposited at different temperatures as used for the determination of their optical bandgap values.

4.8. Electrical Properties

In this section, the behavior of electrical properties of the IO:H layer as a function of temperature has been investigated. One of the critical requirements of a TCO is a low resistivity to avoid losses in ohmic contacts. It is dependent on the interplay between carrier concentration and the mobility of the layer as shown in equation 4.5,

$$\rho = (\mathrm{Ne}\mu)^{-1} \tag{4.5}$$

where ρ is the resistivity, N is the carrier density, e is the elementary charge and μ is the mobility. Typical resistivity values of a TCO range between 10^{-3} to 10^{-4} Ω.cm. The resistance depends on the carrier mobility as in equation 4.6 where μ is the mobility, e is the elementary charge, τ is the average relaxation time and m* is the effective mass of the charge carriers [39].

$$\mu = \frac{\mathrm{e}\tau}{\mathrm{m}^*} \tag{4.6}$$

The relaxation time depends on the drift velocity and the mean free path of the carriers which are the result of an interplay of different scattering mechanisms in the material. Since the relaxation time depends on the temperature, with increasing temperatures, phonon scattering increases and the mobility decreases. The mobility also decreases with increasing impurity concentration as the ionized impurity scattering increases. Mobility, therefore, depends on the interaction between electrons, phonons, and impurities. The temperature dependence of mobility is given by equation 4.7,

$$\mu_{\mathrm{T}} \propto \mathrm{T}^{-3/2} \tag{4.7}$$

and the dependence of mobility on impurity concentration by equation 4.8 where T is the temperature and n_{tot} is the total impurity concentration which consists of ionized impurities, neutral impurities, grain boundaries, etc. [39].

$$\mu_{\mathrm{tot}} \propto \frac{\mathrm{T}^{3/2}}{\mathrm{n}_{\mathrm{tot}}} \tag{4.8}$$

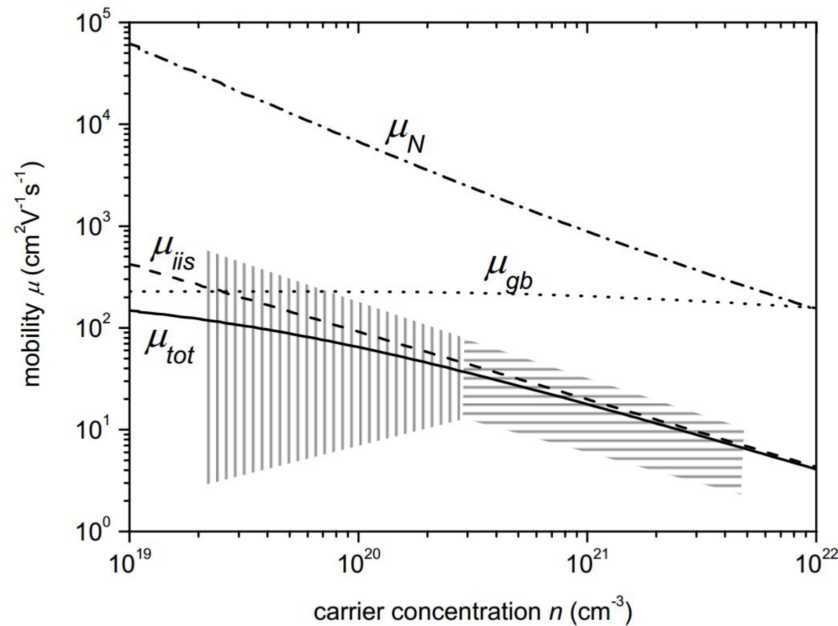

Figure 4.15: Upper mobility limit influenced by different scattering mechanisms. The μ_{iis}-limit is due to ionized impurity scattering, the μ_{gb}-limit is due to grain boundary scattering, the μ_{N}-limit is due to neutral impurity scattering and the μ_{tot}-total mobility limit is due to total impurity scattering. The hashed areas show the spread of data points in literature: horizontal lines for ionized impurities scattering, vertical lines for grain boundary scattering [7].

When both temperature and impurity concentration are taken into account, the total mobility is given by equation 4.9 [39].

$$\frac{1}{\mu_{\text{eff}}} = \frac{1}{\mu_{\text{T}}} + \frac{1}{\mu_{\text{tot}}} \tag{4.9}$$

From the above equation, it is clear that the lower μ value of the two will be the limiting factor for the mobility of the material. The simulation of the upper limit of mobility due to the various scattering mechanisms for indium oxide for a nominal grain size of 50 nm is shown in figure 4.15. The effect of neutral impurities on electron scattering at low carrier density is not significant on the mobility limit. Grain boundary scattering remains relatively constant for carrier densities between 10^{19} cm^{-3} to 10^{22} cm^{-3} and ionized impurity scattering increases with increasing carrier concentration beyond a carrier density of 10^{19} cm^{-3}. Ionized impurity scattering, thus, usually defines the upper mobility limit, however, if the grain size is considerably small, the scattering due to the grain boundaries becomes significant as well, in particular between a carrier density of 10^{19} cm^{-3} to 10^{20} cm^{-3} [7].

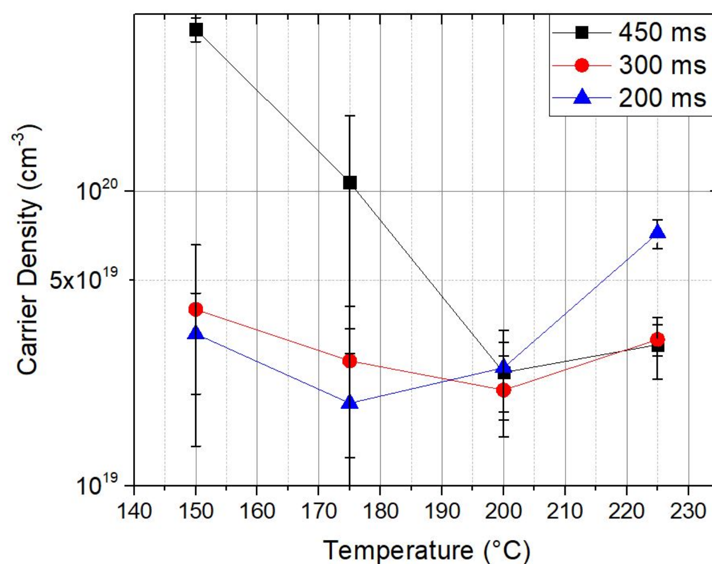

Figure 4.16: Plot of carrier density versus deposition temperature of the IO:H thin films. Layer thickness ~ 140 nm.

The electrical properties are plotted at three different positions in the sample. The black markers (■) show the values at a distance of approximately 3 cm from the center, where the exposure time is 450 ms. This is referred to as the inner circle. The red markers (●) show the values as a distance of approximately 4 cm from the center (exposure time is around 300 ms). This is referred to as the middle circle and the blue markers (▲) show the values at a distance of approximately 5 cm from the center (exposure time is around 200 ms). This is referred to as the outer circle.

Figure 4.16 shows the variation of carrier density as a function of temperature. At 150 °C there is a large spread in the values measured. This spread decreases with increas-

ing temperature until 200 °C. Beyond this temperature, a small spread is again observed. The reason for this difference could be the flow of the plasma-activated radicals along the surface of the substrate. This flow is complex and depends on many factors such as the pressure of the carrier gas, distance from the substrate, temperature, etc. From XRD and SEM analysis, it is clear that increase in temperature increases the crystallinity of the layers leading to a reduction of the number of defects or trap states in the lattice, occupied by H^+, affecting the carrier concentration.

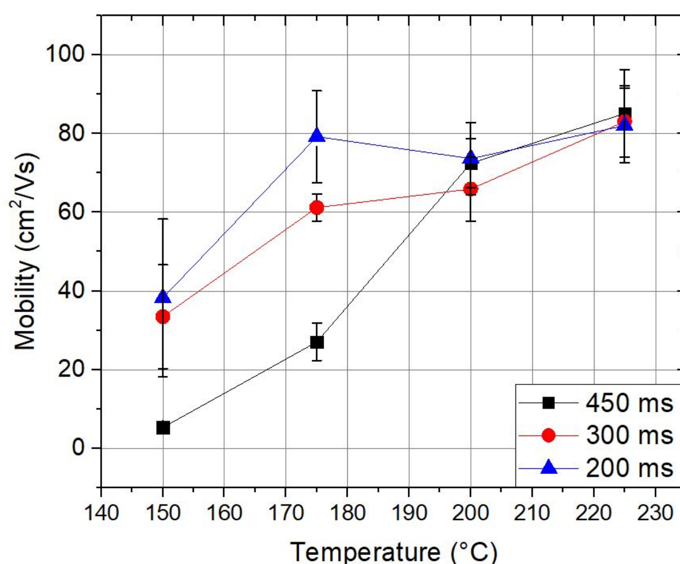

Figure 4.17: Plot of mobility versus deposition temperature of the IO:H thin films. Layer thickness ~ 140 nm.

Figure 4.17 shows the variation of the mobility with temperature. Contrary to what is expected, the mobility in the layers increases with increasing temperature. Ionized impurity scattering plays a dominant role in semiconductors with N > 10^{19} cm^{-3}. The decrease in ionized impurity scattering, as a result of decreasing carrier density, is higher than the increase in phonon scattering due to the increase in temperature. It is also likely that the increased crystallinity will reduce the scattering at grain boundaries. As a result, the overall mobility of the charge carriers increases and reaches a maximum of 85 $cm^2/V.s$. The spread of values at different positions also reduces following the carrier density.

As mentioned before, the combination of carrier density and mobility yields the resistivity of the material. The resistivity of the thin films in this work is measured using a four-point probe station. The overall resistivity decreases with a decrease in temperature. The increase in the mobility with increasing temperatures is more prominent than the decline in the carrier density and the net value of resistivity reaches a low value of around 2 mΩ.cm at 225 °C.

It has been reported that post-deposition annealing of IO:H thin films leads to a signif-

icant improvement of material properties. This is because of solid-phase crystallization of the amorphous material [15, 16]. Post-deposition annealing of the films in an atmosphere of Ar at 200 °C for 30 minutes showed no significant change in their electrical properties, probably because the films were already deposited as polycrystalline layers.

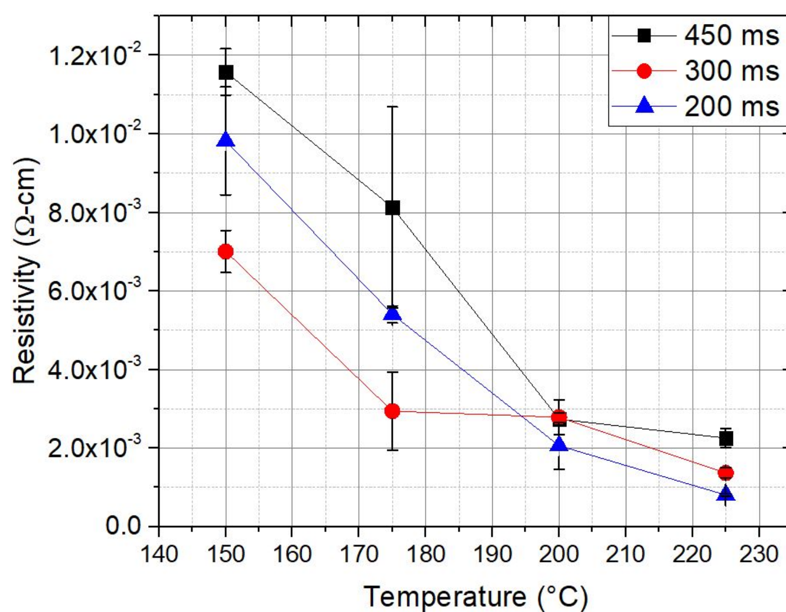

Figure 4.18: Plot of resistivity versus deposition temperature of the IO:H thin films. Layer thickness ~ 140 nm.

4.9. Concluding remarks

In this chapter, the process for depositing IO:H thin films using N_2 plasma has been explored. The films were then characterized and their structural, optical and electrical properties have been discussed. It was found that using plasma-enhanced spatial ALD technique, it is possible to grow the film on a substrate. After studying the growth rate of the thin film for different flow rates of water, a flow rate of 7 g/h was chosen for the best growth rate. Similarly, the effect of the rotation speed of the substrate table on the growth rate was studied and 10 rpm was chosen for optimized film growth. The ALD process window was confirmed to be between 150 °C and 225 °C. It was also observed that plasma enhances the reaction and enables processing at temperatures lower than those for a purely thermal process. Structural analysis showed that the layers are polycrystalline with an average crystal size between 42-45 nm perpendicular to the substrate. The grain size grows laterally with increasing temperature from an average of 50 nm to 100 nm. The film thickness uniformity increases at high temperatures (225 °C) with only 3 % non-uniformity over an area of 50 cm^2. The carrier density decreases to around 3 x 10^{19} cm^{-3} with an increase in temperature, possibly due to a reduction in defects and trap densities. The mobility reaches a maximum value of 85 cm^2/V.s and the resistivity

drops to 2 mΩ.cm. These values are comparable to the values recorded in literature for IO:H.

4.10. Limitations

Hydrogen-doped indium oxide has attracted attention because of the very high values of mobility (120 $cm^2/V.s$) that have been achieved after post-deposition annealing of amorphous layers (sputtering) at relatively low temperatures (200 °C) [16]. Temporal ALD using InCp yields crystalline layers but with a resistivity of around 0.5 mΩ.cm at relatively low temperatures (150 °C-175 °C) [11, 21]. Using spatial ALD, even though a layer with comparable properties has been developed at 200 °C and 225 °C, it is still not on par with the best layers developed. Moreover, the deposition temperatures used here may be unsuitable for some processes. These limitations call for further investigation into methods that enable the deposition of IO:H thin films at lower temperatures.

5

Deposition of hydrogen-doped indium oxide thin films using H_2 plasma

5.1. Introduction

In this chapter, the process for depositing IO:H thin films using H_2 plasma has been investigated. The films were then characterized and their structural, optical and electrical properties have been discussed. The following research questions will be answered in this chapter.

1. Can the entire process be improved by using H_2 plasma?
2. What are the conditions required to deposit IO:H thin films successfully using hydrogen plasma?
3. What is the influence of temperature on the structural, optical and electrical properties of the films?

5.2. Motivation for using H_2 plasma

In chapter 4, it was observed that IO:H thin films with good electrical and optical properties could only be produced by spatial ALD at high temperatures (200 °C and 225 °C). Such high temperatures may not be suitable for polymer substrates, CIGS solar cells, etc. Deposition of the films at a rotation speed of 10 rpm means that the total time taken to deposit 140 nm of IO:H is approximately 2.75 hours. To improve the overall process, an endeavor has been made to (i) decrease the deposition temperature and (ii) increase the net speed of the process while maintaining material properties.

Doping using H_2 plasma has been successfully used to make hydrogen doped zinc oxide using temporal ALD. It was found that the hydrogen from the plasma was incorporated into the layer and enabled higher mobility than that of iZnO [22]. Since hydrogen is

the primary donor in IO:H layers as well, hydrogen plasma along with water was used to improve the process and develop high-quality IO:H thin-films.

5.3. Process parameters

The same plasma source as used for N_2 plasma was used to perform experiments with H_2 plasma. At the time of performing these experiments, it was possible to use both the plasma top flow channels (see figure 3.7) to deliver the co-reactant to the substrate as opposed to the use of a single channel for N_2 plasma. Further, both water and hydrogen are fed through the channels (plasma top flow) to create plasma, which then reacts with the TMI on the substrate. The flow rates of TMI and water were kept constant at 150 sccm and 8 g/h, respectively.

Hydrogen is a highly reactive gas and can form an explosive mixture with air. To reduce this risk at atmospheric pressure, nitrogen has been used as a dilution gas. When argon was used as a dilution gas, a lower voltage than that used for nitrogen was required to maintain a stable plasma (see figure 3.5). This resulted in layers with high resistivity. A mixture of oxygen and hydrogen plasma was also tried but produced layers with very high resistivity possibly due to increased oxygen content and was not pursued further.

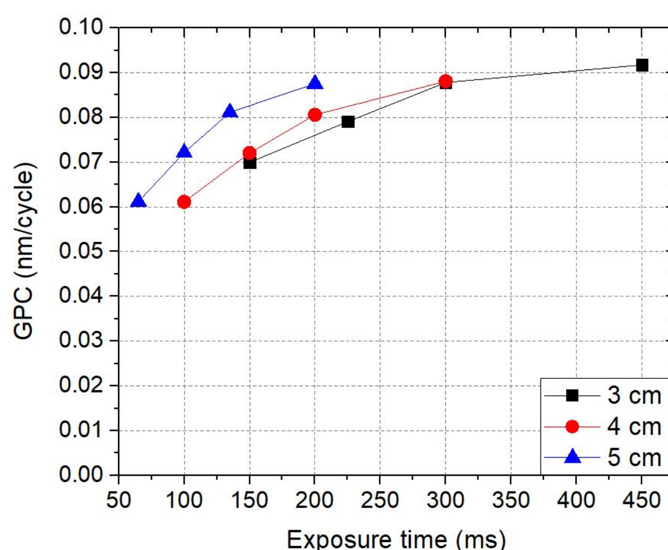

Figure 5.1: GPC versus exposure time for spatial ALD of IO:H from TMI and water. The temperature was maintained at 150 °C and 50 % H_2/N_2 gas mix was used.

The growth rate of the IO:H layer as a function of exposure time is shown in figure 5.1. The temperature is maintained at 150 °C and the concentration of H_2 50 % of H_2/N_2 at a flow rate of 4 slm. The exposure time at different positions on the substrate and different rotation speeds is shown in table 5.1. It is seen here that as before, near-total saturation occurs only at 10 rpm. The GPC at 20 rpm is lower slightly by 0.015 nm/cycle. To develop a faster process, 20 rpm was chosen as the rotation speed for all further experiments and the concentration of H_2 was adjusted for saturation.

Table 5.1: Exposure time at different positions for different rotation speeds.

Speed	Exposure time (ms)		
(rpm)	3 cm	4 cm	5 cm
30	150	100	65
20	225	150	100
15	300	200	135
10	450	300	200

Figure 5.2 shows the growth rate as a function of the percentage of hydrogen. To cover a large range, 12.5 %, 25 % and 50 % H_2/N_2 concentrations are considered. It is seen that as the hydrogen content increases, the GPC decreases slightly. Hydrogen is a reducing agent, therefore it is highly likely that, at high concentrations, the indium oxide layer is being etched during deposition. Similar effects have been observed by Macco *et al.* [22] for hydrogen doped zinc oxide deposition by temporal ALD using hydrogen plasma for doping. A growth rate of 0.08 nm/cycle is achieved using spatial ALD with 12.5 % concentration of H_2 in the plasma. This setting has been used for all further experiments unless stated otherwise.

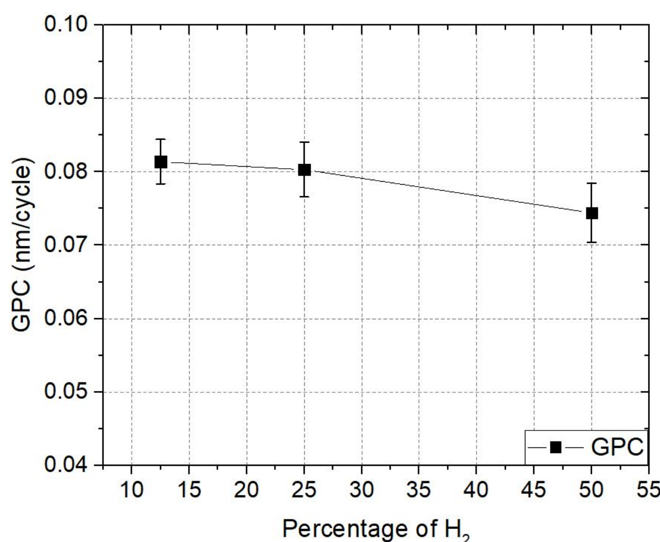

Figure 5.2: GPC versus percentage of H_2 for s-ALD of IO:H from TMI and water. The rotation speed was maintained at 20 rpm and the temperature at 150 °C.

5.4. The ALD process window using H_2 plasma

In ALD, the temperature range for which the growth rate of a material remains constant is known as the ALD process window. Figure 5.3 shows the variation of the growth rate with temperature. It can be seen that, at 150 °C, a growth rate of 0.08 nm/cycle is achieved as compared to 0.06 nm/cycle observed when nitrogen plasma was used (compare figure 4.6). With increasing temperature, the growth rate increases but only slightly, indicating

the saturation region of the curve, shown in the blue region in the figure. Interestingly, with increasing temperature, the difference in thickness at different radial positions on the sample, increased, as shown by the larger error bar. This may result from a combination of the difference in growth rates for different exposure times (20 rpm) and the increased reactivity of the precursor at higher temperatures (see also figure 4.6). In the following sections, the structural, optical and electrical properties of the IO:H thin films deposited as such are discussed.

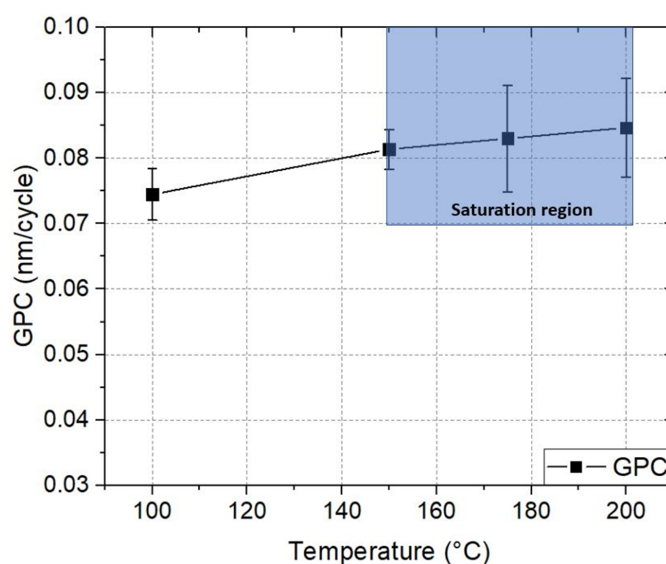

Figure 5.3: GPC versus deposition temperature for s-ALD of IO:H from TMI and water. The rotation speed was maintained at 20 rpm and H_2 concentration was 12.5 %.

5.5. Film thickness uniformity

Figure 5.4 shows the thickness uniformity of two thin films deposited at 150 °C and 200 °C.

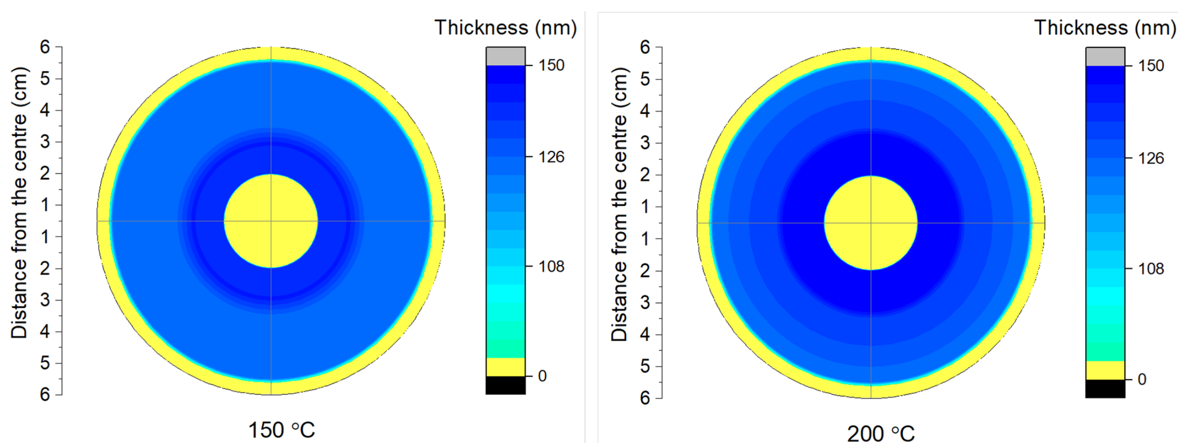

Figure 5.4: Thickness uniformity for IO:H layers deposited at 150 °C and 200 °C.

Using equation 4.3 the non-uniformity of both the layers has been calculated. The

non-uniformity for the film deposited at 150 °C is 3 % while for that at 200 °C is 8 %. The thickness decreases as one moves towards the outer edge of the donut. The effect of different exposure times seems to have a more pronounced effect at higher temperatures.

5.6. Structural Properties

The structural properties of the films have been investigated using the XRD technique.

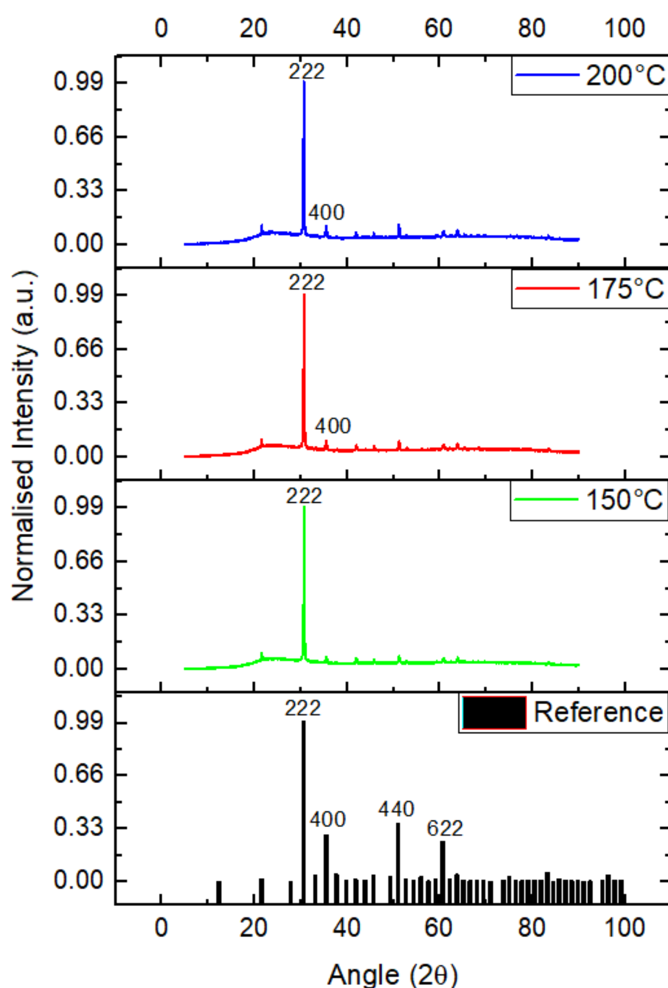

Figure 5.5: XRD patterns for films deposited at 150 °C, 175 °C and 200 °C. Film thickness ~ 140 nm.

A plot of the XRD peak intensities of thin films deposited at 150 °C, 175 °C and 200 °C versus the incident angle (2θ) is shown in figure 5.5. The bottom-most panel shows the peaks obtained from the XRD spectrum of a standard powdered sample of indium oxide. These data were used as a reference and obtained from the COD card number 1010341 [66]. The data were normalized to provide a fair comparison and they show that all samples are crystalline. There seems to be only a slight preference for the (222) orientation as all the peaks corresponding to the standard sample are present, indicating a random orientation. Table 5.2 shows the full width at half maximum for the (222) orientation and

the particle size as calculated using the Scherrer's equation (equation 4.4). It indicates a similar crystalline grain size. An irregular, marginal change with deposition temperature, in the direction perpendicular to the surface of the substrate is observed.

Table 5.2: Approximate size of the crystallites in the IO:H film.

Temperature (°C)	Peak position (2θ)	FWHM	Particle size (nm)
150	30.71	0.21	48.4
175	30.69	0.22	45.9
200	30.67	0.20	49.5

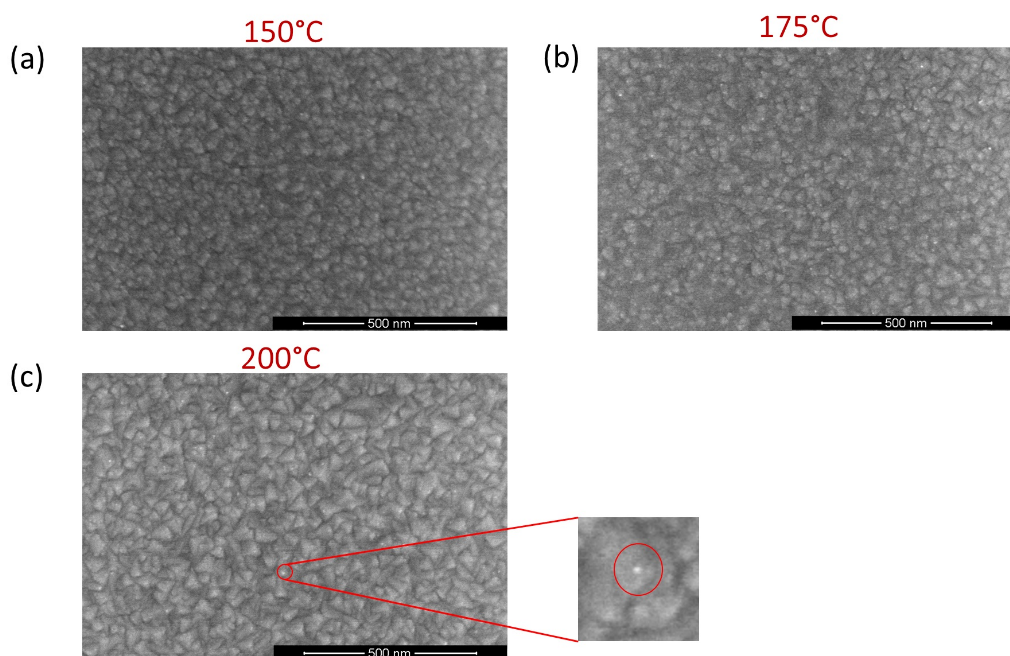

Figure 5.6: Top view of SEM images of the layers deposited at (a) 150 °C, (b) 175 °C and (c) 200 °C. The white speck as shown in the zoom inset to the right of figure 5.6c may indicate embedded crystallites.

For a better insight into the structure of the layer parallel to the surface of the substrate, a top-view SEM analysis was performed. Figure 5.6 shows the images obtained. At 150 °C, the crystals are small and the boundaries are more rounded. The lateral size of the crystals varies between 10 and 65 nm, as derived from figure 5.6. With increasing deposition temperature, the boundaries become sharper and the crystallinity increases. The average size of the crystallites increases and in the films deposited at 200 °C they have a lateral size of 35-80 nm with some crystals being even larger. An increase in the crystal size indicates that the component of grain boundary scattering might decrease as the number of boundaries will decrease. In figure 5.6 c, the white specks, shown to the right of figure 5.6 after magnification, could indicate the embedded crystallites. These crystallites may be located near or at the surface and propagate the growth of crystals (see figure

4.11) [21]. In comparison to the crystals in the layers developed using N_2 plasma, the crystals formed at 150 °C are marginally larger when H_2 plasma is used. The grain boundaries are more sharply defined for the films deposited using N_2 plasma, but as the temperature increases, the crystals formed in both cases are similar in size (compare figure 4.10).

5.7. Optical properties

The optical properties of the IO:H films deposited at different temperatures are discussed below.

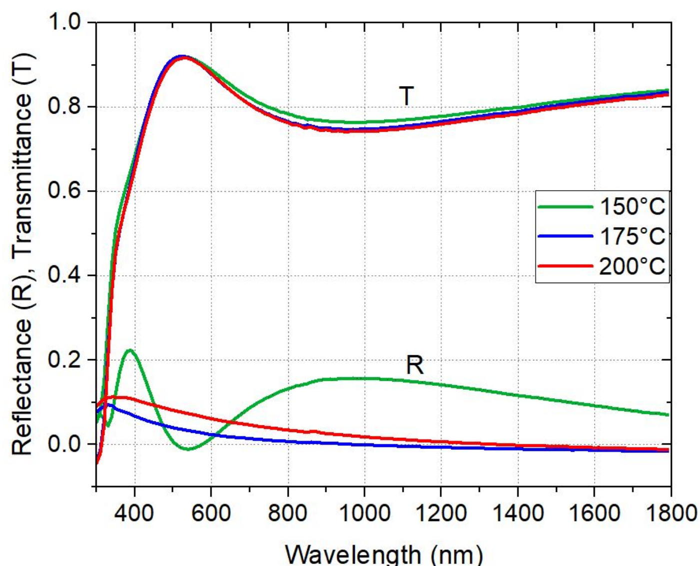

Figure 5.7: Transmission and reflectance of the IO:H films grown at different temperatures. Film thickness ~ 140 nm.

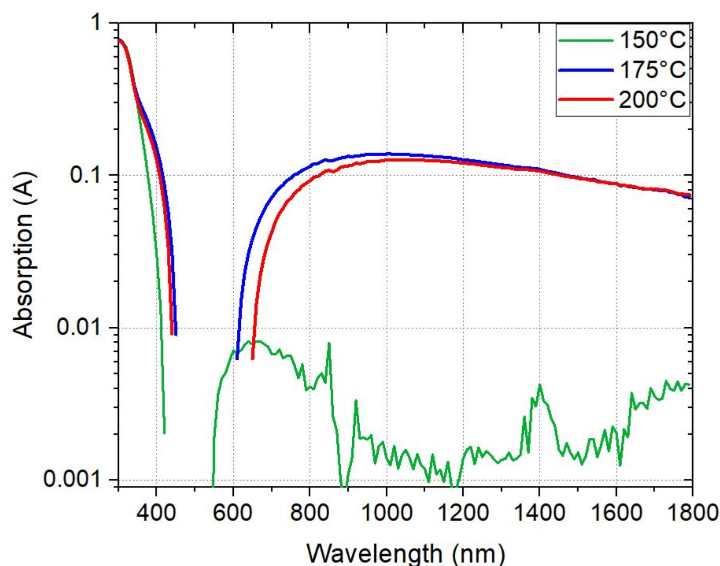

Figure 5.8: Absorbance of the IO:H films grown at different temperatures. Film thickness ~ 140 nm.

The reflectance (R) and transmittance (T) of the films as a function of the wavelength are shown in figure 5.7 while the absorption is shown in figure 5.8. The deposition temperature is denoted in the legend of the plots. Transparency values of around 85 % in the visible region and 80 % over the range of 300-1800 nm, were observed for all layers, with the transparency of the layer deposited at 150 °C being only marginally higher. The transparency in the infrared region is lower than that of the thin films deposited using N_2 plasma by around 2 % (compare figure 4.12). The reflectance of samples deposited at 175 °C and 200 °C is remarkably low but the absorbance for these films is approximately 10 % as shown in figure 5.8. The absorption for the film deposited at 150 °C, however, is less than 1 % in the visible and NIR region of the spectrum.

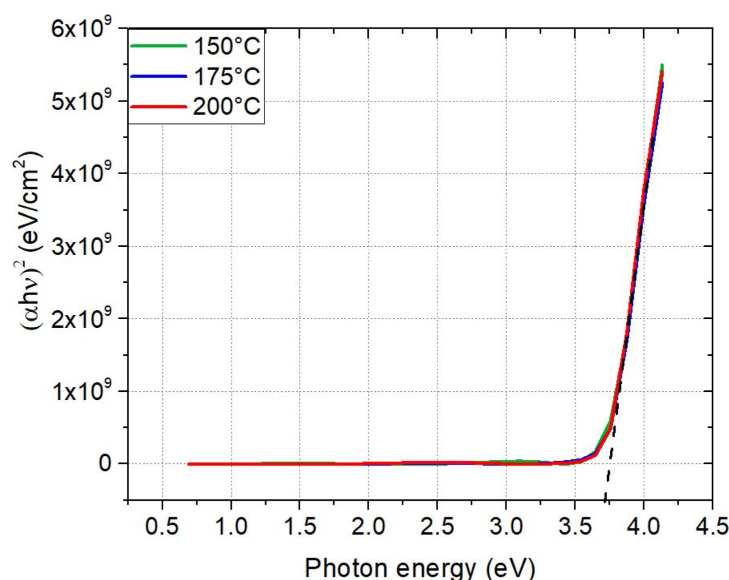

Figure 5.9: Tauc plots of the films deposited at different temperatures for determination of their optical bandgap values.

Tauc plots were used to determine the optical bandgap of the films. Figure 5.9 shows that there is almost no difference in the bandgap of the material deposited at different temperatures and the curves overlap. A direct bandgap of 3.75 eV could be determined. Such a high bandgap means that the material is highly transparent in the visible and NIR region of the spectrum.

5.8. Electrical Properties

Figure 5.10 shows a plot of the carrier density of the IO:H thin films against temperature. As in Chapter 4, the black markers (■) show the values at 3 cm from the center, where the exposure time is 225 ms (inner circle). The red markers (●) show the values at 4 cm from the center (exposure time is 150 ms-middle circle) and the blue markers (▲) show the values at 5 cm from the center (exposure time is 100 ms-outer circle).

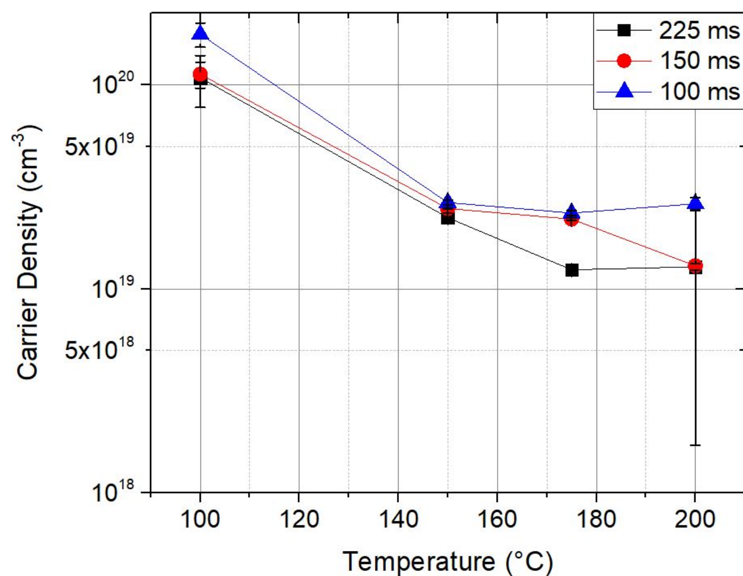

Figure 5.10: Plot of carrier density versus deposition temperature of the IO:H thin films. Layer thickness ~ 140 nm.

The carrier density is the most uniform (2.2 x 10^{19} cm^{-3}) for the thin-film deposited at a temperature of 150 °C. Beyond this temperature, the carrier density remains constant in the outer ring but drops towards the center. The mobility, as shown in figure 5.11, increases correspondingly as both ionized impurity scattering and grain boundary scattering decrease (possibly due to the larger crystal size).

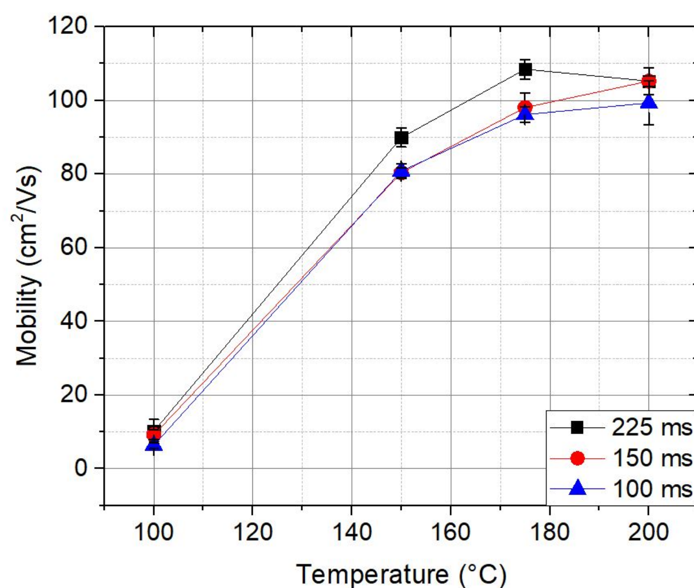

Figure 5.11: Plot of mobility versus deposition temperature of the IO:H thin films. Layer thickness ~ 140 nm.

At 175 °C, the mobility approaches a maximum value of 110 $cm^2/V.s$ (see figure 4.16),

which is very close to the maximum mobility reported for IO:H [16] and thereafter remains constant. This is higher than the mobility observed for films deposited using N_2 plasma, where the maximum value obtained was 85 $cm^2/V.s$ at 225 °C.

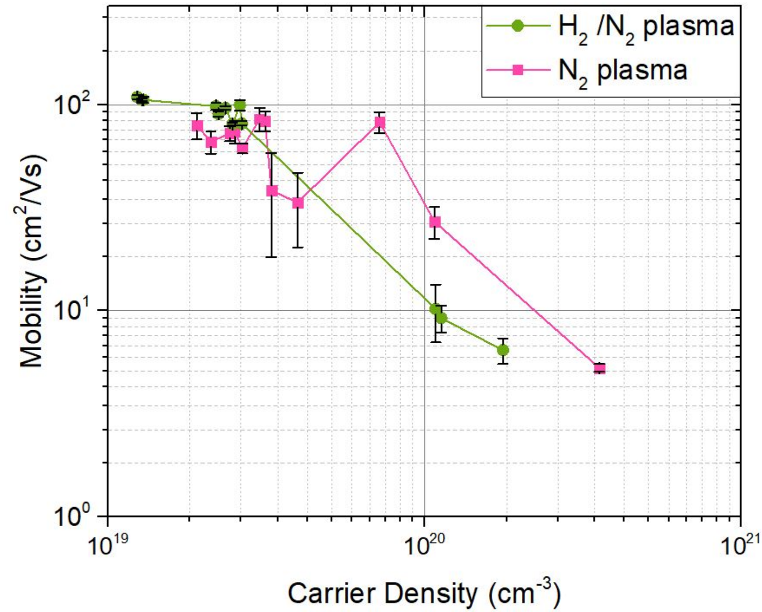

Figure 5.12: Plot of mobility vs. carrier density for IO:H thin-films deposited at different temperatures. The values obtained when N_2 plasma and H_2/N_2 plasma are used are shown using pink and green markers, respectively.

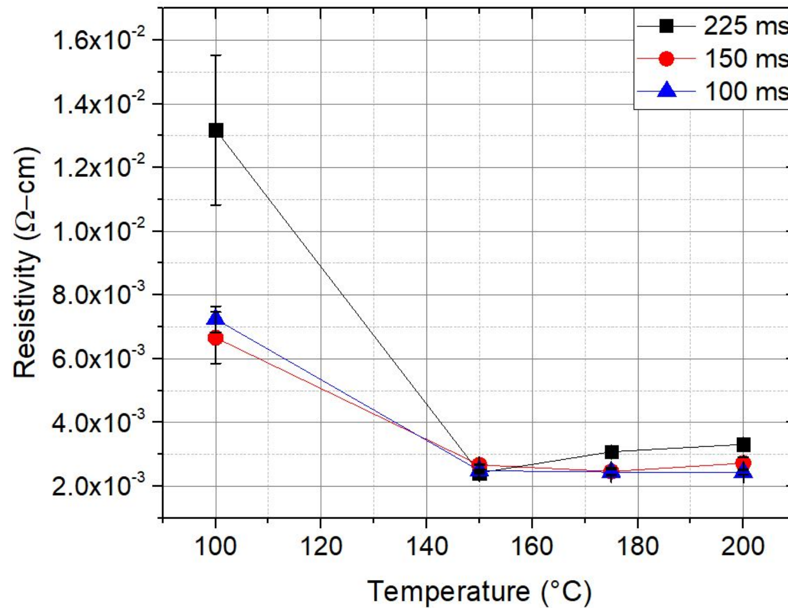

Figure 5.13: Plot of resistivity of the IO:H thin films versus deposition temperature. Layer thickness ~ 140 nm.

Figure 5.12 shows a plot of mobility values measured versus the corresponding carrier density. It is seen that with an increase in the carrier density, the mobility decreases, following the trend shown in figure 4.15. Here, ionized impurity scattering and grain boundary scattering seem to dominate and thus set the upper mobility limit. It can be seen that beyond a carrier density of 3 x 10^{19} cm^{-3}, the mobility for thin films deposited using N_2 plasma is higher. This is mainly due to different deposition temperatures.

Figure 5.13 shows a plot of the resistivity against deposition temperature. As of 150 °C, a resistivity value of 2.5 mΩ.cm is observed which is practically the same at all three positions on the sample. The increase in mobility at 175 °C and 200 °C is not enough to compensate for the drop in carrier density at these temperatures, resulting in a marginal increase in resistivity towards the center at higher temperatures.

5.9. Concluding remarks

In this chapter, the effect of using H_2/N_2 plasma instead of N_2 plasma has been explored. The use of H_2 facilitates the deposition of IO:H thin films with excellent layer properties at a temperature of 150 °C as compared to a temperature of 200 °C or 225 °C which is required when N_2 plasma is used. A carrier density of 2.2 x 10^{19} cm^{-3}, a mobility of 85 $cm^2/V.s$ and a resistivity of 2.5 mΩ.cm was achieved for the film with a thickness of 140 nm. A high optical transparency with very low absorption in the infrared region was observed. As the rotation speed has been doubled, depositions with H_2/N_2 plasma take only half of the time (1.5 hours) in comparison to the process with N_2 plasma. The non-uniformity that has been observed may be eliminated by depositing the films at rotation speeds lower than 20 rpm (see table 5.1).

6

Optical modelling of IO:H thin films in a CIS solar cell

6.1. Introduction

In chapters 4 and 5, the deposition and characterization of IO:H layers using N_2 and H_2/N_2 plasma have been explored. This TCO has been developed with the application as an electrode in solar cells in mind. This chapter is dedicated to the optical simulation of the short-circuit current in a cell with IO:H deposited by spatial ALD as a TCO. To fully appreciate the properties of the material, a comparison with indium tin oxide (ITO) was made. This choice was made because ITO is the mainstay indium-based TCO material used in the industry, and having comparable electrical properties. The following research question has been answered.

- How do the thin films deposited by this method compare against ITO when an optical analysis is performed?

6.2. Optical modelling and simulations

Solar cells are complex optical devices that utilize light in-coupling and trapping techniques. Optical simulation of solar cell design is a vital tool that provides a detailed understanding of the optical behavior of the cell. Studying the losses due to reflection and parasitic absorption and devising ways to reduce them is one of the most important advantages of performing optical modelling. Optical simulation tools allow us to analyze each layer of a device individually and design it. The development of accurate modelling techniques in the recent past has meant that the experimental results match closely with the results obtained from simulations and thus time and resources can be saved by using optical simulations during cell design [70].

Most of the optical models are based on either wave optics or ray optics. Models

based on wave optics are computation-intensive as they consider the electromagnetic nature of light by solving Maxwell equations. Using this method only allows for small simulation domains. Ray optics considers light as rays and wave effects such as diffraction are ignored because of which sub-wavelength features cannot be studied. Depending on the application, a model based on either wave optics or ray optics is chosen.

6.3. Optical simulations using GenPro4

In this research work, GenPro4 was used to perform optical simulations. GenPro4 is an optical model for solar cells that has been built on ray optics developed on MATLAB (matrix laboratory). In GenPro4, a cell is modelled as a 1-D multi-layered structure and the light absorbed in each layer is calculated taking into account scattering and light trapping at interfaces. Each layer in a solar cell absorbs or reflects a certain amount of light. As a result, only a part of the incident light is ultimately converted into energy. A TCO is one of the many layers in a cell and has a significant effect on the total efficiency. It should be noted that GenPro4 only takes into account the optical properties of the layer and no electrical properties are considered [70].

The net-radiation method is used to calculate the reflectance (R), transmittance (T) and absorbance (A) of the solar cell layers. The model uses the complex refractive index of a material (n,k data) measured at each wavelength to calculate R, T and A also as functions of wavelength using Fresnel equations.

This method is accurate for flat layers that are thicker than the coherent length of sunlight ($\sim 1\ \mu$m). These layers are incoherent layers. Layers thinner than ($\sim 1\ \mu$m) are considered coherent and treated as 'coatings.' This distinction is important as the effect of interference comes into play for thin films. For incoherent films, at each interface, four fluxes are defined. They indicate the light entering/leaving the interface from top/bottom. Each flux represents net-radiation from all photon paths and is simply added. The net radiation method can be adapted for coherent layers as well. In coherent layers, the fluxes represent complex amplitudes of the incident electromagnetic waves and a separate calculation method is used for determining the optical properties. It is also possible to estimate the effect of surface textures by using the scalar scattering method [70].

GenPro4 has been used to simulate optical models for c-Si cells, perovskite based tandem cells, thin film solar cells etc. and the results have been validated against measured data. For e.g., Zhang *et al.* have shown that for 4-terminal perovskite / c-Si tandem mini modules, the simulated and experimental optical and electrical characterization match closely. It was found that the EQE of the cell and the absorption of light in the absorber layer as predicted by the model were in close agreement.

6.3.1. Validation using IO:H-Glass interface

Optical simulations can be used to investigate the influence of TCOs on the overall cell performance and to optimize the TCO layer thickness for a better overall design. They can also be used to compare the optical performance of one TCO to another. IO:H deposited by spatial ALD in this work serves as a TCO and investigating its performance in a solar cell is important.

First, to check the accuracy of the simulation, IO:H was simulated on glass and the measured values of R, T, A were compared with the values as calculated using GenPro4. The n-k data file was used as an input to the model. Figure 6.1 shows the comparison between the two. The continuous lines represent the values as calculated using GenPro4 and the open circular symbols represent the n-k data obtained from SE measurements. It can be seen that the measured and calculated data matches closely in the wavelength range considered. This implies that this data can be used to predict the performance of the TCO in a cell reliably.

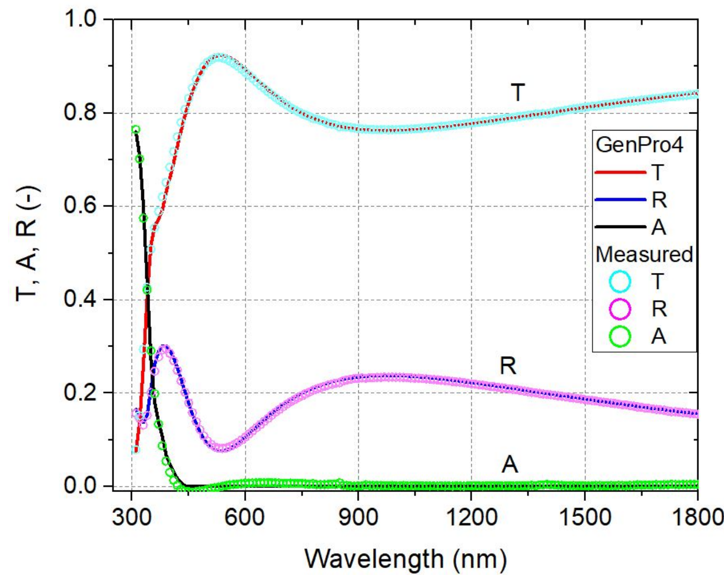

Figure 6.1: Measured optical properties compared with the optical properties calculated using GenPro4.

6.3.2. Comparison of IO:H with ITO

A CuInSe (CIS) based solar cell with a stack as shown in figure 6.2 was chosen as an example cell for the simulation as this material absorbs light in the broad range of 300 nm to 1320 nm. The short-circuit current can be calculated by equation 6.1.

$$J_{sc} \approx J_{CIS} = e \int_{300}^{1320} A_{CIS}(\lambda)\varphi(\lambda)d\lambda \tag{6.1}$$

where J_{sc} and J_{CIS} are the short-circuit currents, e is the elementary charge, $A_{CIS}(\lambda)$ is

the absorption in the CIS absorber layer as a function of the wavelength and $\varphi(\lambda)$ is the photon flux of the AM 1.5 solar spectrum as a function of the wavelength.

Two cell structures, one with IO:H as the TCO and another with ITO as the TCO were compared. ITO was chosen as it is the most popular indium based TCO and has electrical comparable properties. For a fair comparison, both the TCOs were modelled such that their sheet resistance is the same. As resistivity is a material property, the sheet resistance was matched by altering the thickness of the coating. An IO:H coating with a resistivity value of 2.2 x 10^{-3} Ω.cm was chosen as this is one of the lowest values achieved using spatial ALD. For ITO, a resistivity value of 4.2 x 10^{-4} Ω.cm was chosen as a representative value [71]. Consequently, to achieve a sheet resistance of 60 Ω/□, a 420 nm thick layer of IO:H is required while only a 70 nm thick layer of ITO is needed. Because of the difference in the resistivity of IO:H and ITO, a much thicker layer of IO:H is required to achieve the target sheet resistance.

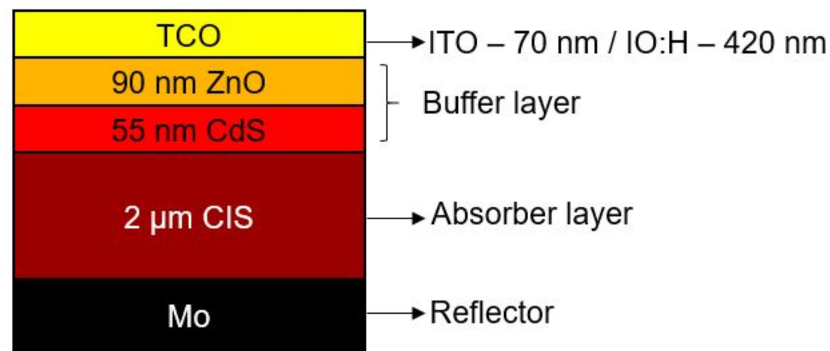

Figure 6.2: TCO-ZnO-CdS-CIS-MO stack used for optical analysis.

Figures 6.3 and 6.4 show the absorption of light in each layer of the solar cell stack. In the wavelength range of 300-1300 nm, a maximum of implied photocurrent density of 51.49 mA/cm^2 is available which is distributed in each layer as shown in the legends of figures 6.3 and 6.4. The absorption in each layer (ZnO, CdS, CIS and Mo) of the cell stack is influenced by the absorption and reflection from the layers and the interference in the thin films. An increase in the thickness of the TCO may cause more interference peaks in a certain wavelength range.

It can be seen that when IO:H is used as the TCO, there is no absorption in the infrared region. However, when ITO is used, free carrier absorption is observed possibly due to a higher carrier density. Absorption loss in ITO is approximately 1.5 % as compared to 1.3 % in IO:H. Despite this, absorption in the CIS layer with ITO is higher by 0.52 mA/cm^2. This is because the loss due to reflection from IO:H is greater than that from ITO by 2 %. The advantage of high transparency of IO:H is lost here as a very thick layer of TCO is used to compensate for the resistivity. The reflection losses can be minimized by further optimizing the layer with texturing, use of anti-reflective coating, etc.

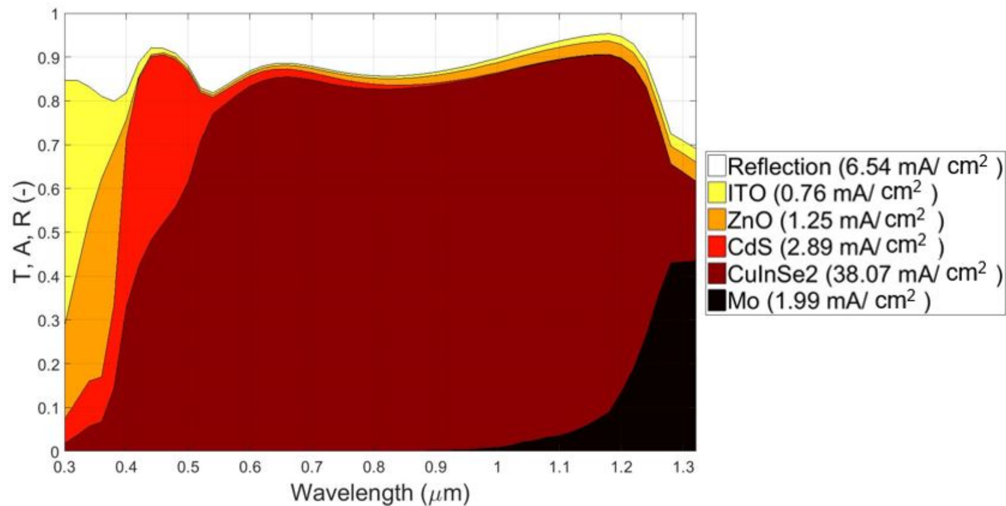

Figure 6.3: Simulation of the short circuit current components in a CIS solar cell with ITO as the TCO.

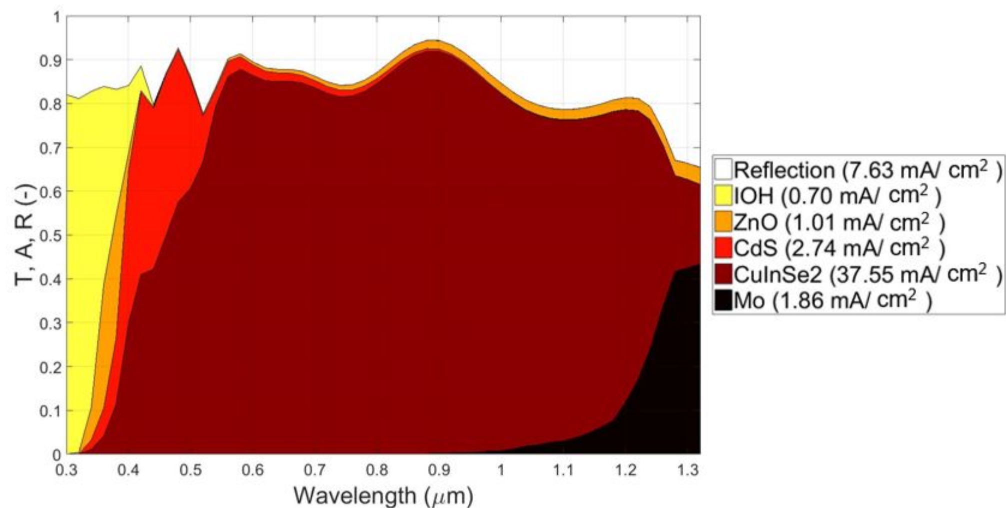

Figure 6.4: Simulation of the short circuit current components in a CIS solar cell with IOH deposited using spatial ALD as the TCO.

6.4. Concluding remarks

In this chapter, an optical analysis of the IO:H film developed using spatial ALD was performed and compared with the performance of ITO, which is currently one of the most widely used TCOs in the solar industry. The measured optical properties of IO:H were first compared with the R, T, A values calculated from the n-k data of the material using the GenPro4 model and found to be in close agreement. When IO:H was compared with ITO as a TCO in a CIS solar cell, it was found that a thick layer of IO:H needs to be used to compensate for the higher resistivity of layer in comparison to ITO. IO:H has significant reflection losses which can be reduced either by using light trapping techniques or by

adjusting the thickness of the film such that an anti-reflective effect is produced at the same wavelength as in the ITO based stack. An anti-reflective effect can be obtained by using a thickness such that the path difference between the reflected waves is $\lambda/2$, where λ is the wavelength.

7
Conclusions and recommendations

7.1. Concluding remarks

The main aim of this thesis was to contribute to the development of high-quality hydrogen-doped indium oxide using atmospheric-pressure plasma-enhanced spatial atomic layer deposition. In this research project, it has been shown that it is possible to develop such a process. The films so deposited were then characterized and their structural, optical and electrical properties were discussed.

First, a choice of the precursor and the co-reactant to be used was made keeping in mind the reactivity, availability, cost and the possibility of up-scaling for commercial implementation. Trimethylindium (TMI) and water were chosen as the precursor and the co-reactant, respectively.

The development of a process from scratch involves the analysis of different process parameters and a selection of them for the best results. The most significant parameters such as the concentration of the reactants, the substrate rotation speed and consequently the exposure time of the substrate to the reactants, and the deposition temperature were studied. In the first set of experiments, N_2 plasma was used to enhance the reaction between TMI and water. After considering the growth rate for different flow rates of water, a flow rate of 7 g/h was chosen as the highest growth rate was observed for this flow. Similarly, the effect of the rotation speed of the substrate table on the growth rate was studied. 10 rpm was chosen as this rotation speed allowed for saturation throughout the area of the substrate exposed to the reactants. Next, the growth rate of the thin-film as a function of the deposition temperature was studied. The temperature window for this ALD process was confirmed to be between 150 °C and 225 °C. A comparison between the growth rates for a purely thermal process with the plasma-enhanced process showed that plasma enhances the reaction and doubles the growth rate from 0.045 nm/cycle to 0.09 nm/cycle. Plasma also enables processing at temperatures lower than those of a purely thermal process.

Further analysis was carried out for thin films deposited at 150 °C, 175 °C, 200 °C and 225 °C. To study the morphology of the films deposited, XRD and SEM analysis was performed. From XRD, it was concluded that all four layers are polycrystalline. A comparison of the diffraction peaks of the thin-films deposited with those of a standard powder sample of In_2O_3 showed that all peaks are present with a slight preference for the (222) orientation. The average crystal size was between 42-45 nm perpendicular to the substrate. The increase in the mean grain size with increasing temperature is marginal in this direction. SEM analysis showed that the grain size grows laterally with increasing temperature from an average of 50 nm to 100 nm. The increase in grain size could lead to fewer grain boundaries. The film thickness uniformity was calculated and it was found that the uniformity increases at high temperatures (225 °C) with only 3 % non-uniformity over an area of 50 cm^2. At 150 °C, the non-uniformity was 15% for the same area. It was reasoned that with increasing temperature, the reactivity of the reactants increases and contributes to the uniform growth. The electrical and optical properties of a TCO are of utmost importance. The transparency of the IO:H thin films deposited in this research work was 90 % in the visible spectrum and 85 % on an average for a spectral range of 300-1800 nm. The absorbance in the layers increased with increase in temperature but was below 10 % for all cases. The carrier density decreases to around 3 x 10^{19} cm^{-3} with an increase in deposition temperature. This is accompanied by an increase in the mobility which reaches a maximum value of 85 $cm^2/V.s$ and the resistivity dropping to 2 mΩ.cm at 225 °C. The interplay between ionized impurity scattering and phonon scattering results in the increase in mobility. While the optical and electrical properties achieved are good, the deposition temperatures required to achieve them is quite high and the process time of 2.75 hours is too slow. An endeavour is, thus, made to enable the deposition of layers with similar or better properties at lower deposition temperatures in a shorter time.

Because hydrogen is one of the primary donors in these thin films, using a H_2/N_2 plasma was the next logical step. As for the earlier set of experiments, the process parameters were once again determined for best results. A rotation speed of 20 rpm was chosen along with a 12.5 % dilution ratio for the H_2/N_2 plasma. A small concentration of H_2 was opted to avoid possible etching effects on the deposited layer. The use of H_2 facilitates the deposition of IO:H thin films with excellent layer properties at a temperature of 150 °C as compared to a temperature of 200 °C or 225 °C which is required when N_2 plasma is used. The thickness non-uniformity increased from 3 % to 8 % with an increase in temperature from 150 °C to 200 °C. Contrary to the earlier set of experiments, the inner film deposition zone was found to be thicker than the outer one. This seems to be the effect of the different exposure times at various radial positions enhanced by the increase in reactivity of the reactants at higher temperatures. XRD analysis showed similar results as in the case with N_2 plasma. An average crystal size of 47 nm in the direction perpendicular to the substrate was observed with little change as the deposition temperature was varied. In the direction parallel to the surface of the substrate, an increase in crystal size which varies within a layer was observed. At 150 °C, the crystals are small and

rounded. At higher temperatures, the crystallites have larger and sharper, more defined edges. Upon measuring the electrical properties, a carrier density of 2.2 x 10^{19} cm^{-3}, a mobility of 85 $cm^2/V.s$ and a resistivity of 2.5 mΩ.cm were achieved for a film thickness of 140 nm at a deposition temperature of 150 °C. An even higher mobility of 110 $cm^2/V.s$ was achieved for films deposited at 175 °C as compared to the value of 85$cm^2/V.s$ obtained for a deposition temperature of 225 °C using N_2 plasma. However, the spread in the values of carrier density increases with increasing temperature. A high optical transparency, close to 90 %, in the visible spectrum of the wavelength with very low absorption in the infrared region, was observed for films grown at 150 °C. As the rotation speed has been doubled, depositions with H_2/N_2 plasma take only half of the time (1.5 hours) in comparison to the process with N_2 plasma. The non-uniformity that has been observed may be eliminated by depositing the films at a rotation speed lower than 20 rpm (see table 5.1). After taking into account all the observations, it can be said that the use of H_2/N_2 plasma makes a significant difference and enables the deposition of a good TCO at relatively low temperatures.

An optical analysis of the IO:H film developed in this work was performed and compared with the performance of ITO, which is currently the most used TCO in the solar and display industry. It was found that, to compensate for the high resistivity of the IO:H layer in comparison to ITO, a thick layer of IO:H needs to be used. The IO:H thin-film developed with spatial ALD has significant reflection losses that may be reduced by using light trapping techniques such as texturing, employing the anti-reflective effect, etc.

7.2. Recommendations

Through this thesis, many parameters involved a new process development have been explored, yet, there is a long way to go in making the IO:H thin film a strong contender in industry applications.

In this study, due to the time constraint, the parameters that govern plasma such as power, plasma source configuration, the flow of gases, etc. were kept constant. It is recommended that an in-depth analysis of these parameters is carried out. Plasma chemistry is highly complex, and with each configuration, a different effect may be observed. The other aspect to be considered is the shape of the plasma source which is linear. This causes differences in the exposure time and may inhibit saturation at high substrate rotation speeds in a rotary reactor.

The properties of a TCO are the result of an interplay between the charge carrier density and the effect of the structure of the material deposited. The carrier density measured for the IO:H thin films in this work is ~ 10^{19} cm^{-3}. The resistivity of the material is low but not the best value of IO:H thin films reported in literature [15, 16]. An optimum value of carrier density that ensures a low resistivity and high transparency needs to be achieved. An approach to this would be to investigate how exactly the dopant incorporation in a plasma-enhanced spatial ALD process occurs and how it can be controlled.

The performance of a TCO can only be fully appreciated once it is incorporated in a device. In this thesis, an optical analysis of the performance expected, based on the optical data, was carried out. It is recommended that the IO:H thin-films developed by the process suggested in this thesis be incorporated in an actual solar cell such as a-Si or CIGS, to gain an understanding of its advantages and disadvantages and their effect on the solar cell performance (fill factor, efficiency, etc.).

A

Recipe for the deposition of IO:H thin films using plasma enhanced spatial ALD

Apart from the experimental settings mentioned in the report, several other recipe parameters were used for the deposition of the IO:H thin films as described above. These settings are listed below.

A.1. Deposition using N_2 plasma

- Deposition temperature: 150 °C-225 °C
- Flow of water: 7 g/h
- Rotation speed of the substrate table: 10 rpm
- Flow rate of TMI: 150 sccm
- Plasma voltage: 5000V
- Plasma duty cycle: 50 kHz
- Flow rate of N_2 for plasma: 2.5 slm
- Flow rate of N_2 for top flow: 3.5 slm
- Flow rate of N_2 for dilution of water: 1 slm
- Initial no. of cycles: 1600
- Pressure of N_2 in the gas bearing: 1600 mbar

A.2. Deposition using H_2/N_2 plasma

- Deposition temperature: 100 °C-200 °C
- Rotation speed of the substrate table: 20 rpm
- Flow of water: 8 g/h
- Flow rate of TMI: 150 sccm
- Plasma voltage: 5000V
- Plasma duty cycle: 50 kHz
- Total flow rate of H_2/N_2 mix for plasma: 4 slm
- Flow rate of N_2 for bottom flow: 2.5 slm
- Flow rate of N_2 for dilution of water: 1 slm
- Initial no. of cycles: 1600
- Pressure of N_2 in the gas bearing: 1600 mbar

B

Determination of the optical bandgap using the Tauc plot

The Tauc plot is used to determine the optical bandgap of semiconductor materials. It was first proposed by Tauc *et al.* that the optical bandgap of a material can be calculated using the relation B.1,

$$\alpha h\nu = A(h\nu - E_g)^m \tag{B.1}$$

where α is the absorption coefficient, h is Planck's constant, ν is the frequency in Hz and E_g is the optical bandgap of the material in eV. Here, A is a constant and the value of n depends on the type of transition that takes place in the material. For

- n=1/2, it implies a direct allowed transition
- n=2, it implies an indirect allowed transition
- n=3, it implies indirect forbidden transition and
- n=3/2, it implies direct forbidden transition

A plot of $(\alpha h\nu)^{1/n}$ versus $h\nu$ is used to determine the bandgap. If the linear part of the curve is extrapolated to meet the x-axis, the intercept gives the value of the optical bandgap. For several semiconductors a tail at the lower energy side of the absorption edge exists. Such an example was reported by Tauc [72] for amorphous Ge. This band was not observed in crystalline Ge implying that the strength of the band is sensitive to the structure of the material. The presence of localized defects present in amorphous layers or low crystalline layers causes the extension of the bandgap [72].

The bandgap of indium oxide has long been debated upon. Walsh *et al.* have shown that for indium oxide the bandgap from the VBM to the CBM is formally forbidden. This

is because of parity selection rules. Both VBM and CBM are of even parity and thus contribute to optical transitions only weakly. From 0.81 eV below the VBM strong optical transitions are observed (figure B.1). The odd parity bands at 0.25 eV and 0.5 eV below the VBM are pseudodirect, and hence only weak transitions are observed [73].

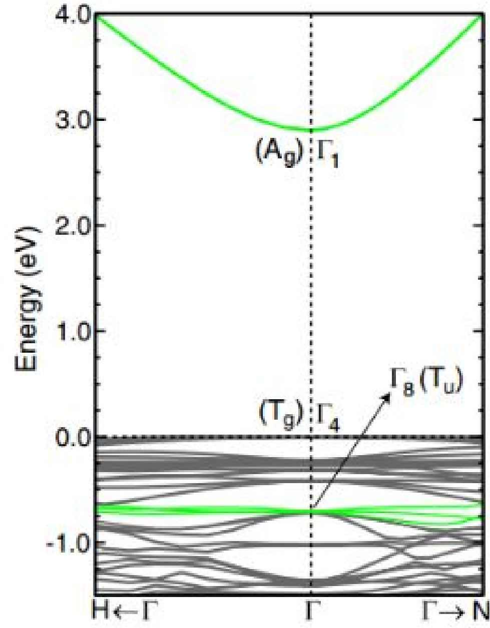

Figure B.1: Band structure of indium oxide [73].

C

Relation between the refractive index, electrical and optical properties

The refractive index of a material is closely related to the electrical and the optical properties of a material. The complex refractive index $\overline{n}_r$ of a material is given by equation C.1, where n_r is the real part and k is the extinction coefficient [74].

$$\overline{n}_r = n_r - ik \tag{C.1}$$

Both n_r and k are related to the relative permittivity (ε_r) as shown in equations C.2 and C.3 [75],

$$n_r = \sqrt{\frac{\sqrt{(\varepsilon_1{}^2 + \varepsilon_2{}^2)}}{2} + \frac{\varepsilon_1}{2}} \tag{C.2}$$

$$k = \sqrt{\frac{\sqrt{(\varepsilon_1{}^2 + \varepsilon_2{}^2)}}{2} - \frac{\varepsilon_1}{2}} \tag{C.3}$$

where, ε_1 is the real part and ε_2 is the imaginary part of ε_r. The relative permittivity can be expressed as a sum of various susceptibilities as shown in equation C.4. Here, χ_{BG}, χ_{FE}, χ_{PH} are the contributions of the bandgap, free electron gas and optical phonons, respectively [75].

$$\varepsilon = \varepsilon_1 + i\varepsilon_2 = 1 + \chi_{BG} + \chi_{FE} + \chi_{PH} \tag{C.4}$$

The contribution of bandgap is the most prominent in the visible range of the spectrum while the contribution of the free electrons dominates the near IR (750-1400 nm)

mid IR (3000-8000 nm). The optical phonon contribution is prominent in the far IR region of the electromagnetic spectrum. This can be used to approximate the relative permittivity as a sum of ε_∞ and χ_{FE}, where ε_∞ is the high frequency permittivity, in the NIR region. The real (ε_1) and imaginary (ε_2) parts of ε then are given by eqs. C.5 and C.6, respectively [75].

$$\varepsilon_1 = \varepsilon_\infty(1 - \frac{{\omega_p}^2}{\omega^2}) \tag{C.5}$$

$$\varepsilon_2 = (\frac{\varepsilon_\infty {\omega_p}^2}{\omega^3 \tau}) \tag{C.6}$$

Here, ω_p is the plasma frequency of the material, ω is the angular frequency and τ is the relaxation time of the electron. The plasma frequency of a material is a function of the carrier density of the material as shown in equation 1.1. The relaxation time of an electron is related to the mobility as shown in equation 4.6. The absorption coefficient, α, is dependent on the extinction coefficient as shown in equation C.7.

$$\alpha = 4\pi \mathrm{k}/\lambda \tag{C.7}$$

where λ is the wavelength in nm. The transmittance in turn is related to the absorption coefficient by Beer-Lambert's law. From all the equations above, it is seen clearly that the electrical properties and optical properties are closely related and this presents the opportunity for trade-offs between the carrier mobility, density and the thickness of the thin film.

8

Glossary

8.1. List of acronyms

AC	Alternating Current
ALD	Atomic Layer Deposition
ALE	Atomic Layer Epitaxy
AZO	Aluminium zinc oxide
BCC	Body centered cubic
BSE	Back Scattered Electrons
CBM	Conduction Band Minimum
CIGS	Copper Indium Gallium Selenide
CMOS	Complimentary Metal Oxide Semiconductor
CVD	Chemical Vapour Deposition
DC	Direct Current
DRAM	Dynamic Random Access Memory
FET	Field Effect Transistor
FWHM	Full Width at Half Maximum
GPC	Growth per cycle
InCp	Indium Cyclopentadienyl
IO:H	Hydrogen doped indium oxide

ITO Indium Tin Oxide

MOCVD Metal Organic Chemical Vapour Deposition

OLED Organic Light Emmitting Diode

PECVD Plasma Enhanced Chemical Vapour Deposition

PLD Pulsed Laser Deposition

PV Photovoltaic

PVD Physical Vapour Deposition

QCM Quartz Crystal Microbalance

rpm Rotations per minute

SDBD Surface Dielectric Barrier Discharge

SEM Scanning Electron Microscopy

SHJ Silicon Hetero Junction

TCO Transparent Conductive Oxide

TMI Trimethylindium

TNO Nederlandse Organisatie voor Toegepast Natuurwetenschappelijk Onderzoek

VBM Valence Band Maximum

XRD X ray Diffraction

8.2. List of symbols

A	Absorbance
A_{CIS}	Absorbance in a CIS cell
B	Magnetic field
d	Thickness
D	Average crystal size
e	Elementary charge ($1.6 * 10^{-19}$C)
E	Electric field
E_A	Energy levels introduced by acceptor atoms
E_b	Height of the potential barrier
E_C	Energy at conduction band minimum
E_D	Energy levels introduced by donor atoms
E_F	Fermi level
E_g	Bandgap
E_V	Energy at valence band maximum
F	Incident flux
h	Planck's constant
H_i	Interstitial hydrogen
H_o	Substitutional hydrogen
I	Current
$I(d)$	Transmitted intensity
I_0	Incident intensity
J	Current Density
J_{SC}	Short circuit current density
J_{CIS}	Short circuit current density of a CIS cell
k	Extinction coefficient
k_b	Boltzmann's constant

L	Length
L_g	Grain size
m^*	Effective electron mass
$\overline{n}_r$	Complex refractive index
n_r	Refractive index
n_s	Sheet carrier density
N	Carrier Concentration
q	Charge of the trap
r_p	Reflectivity of p-polarized light
r_s	Reflectivity of s-polarized light
R	Reflectance
R_{ads}	Rate of adsorption
R_s	Sheet resistance
S	Sticking probability
t	Thickness
T	Temperature
V_H	Hall voltage
V_o	Oxygen vacancies
W	Width

α	Absorption coefficient
β	Full Width at Half Maximum
γ_A	Surface free energy of a film material with phase A
γ_B	Surface free energy of a film material with phase B
γ_i	Interfacial energy
Δ	Phase of change in polarization
ε	Relative permittivity

ε_0	Permittivity in vacuum
θ	Angle of incidence
λ	Wavelength
μ	Mobility
μ_{eff}	Effective mobility
μ_{gb}	Mobility due to grain boundary scattering
μ_{i}	Mobility due to one component of scattering
μ_{ph}	Mobility due to phonon scattering
μ_{tot}	Total mobility component due to scattering
μ_{T}	Temperature dependence of mobility
ν	Frequency
ρ	Resistivity
σ	Conductivity
ϕ	Photon flux
ψ	Magnitude of change in polarization
τ	Relaxation time
ω_{p}	Plasma frequency
Ω	Resistance

Bibliography

[1] R. K. Pachauri, M. R. Allen, V. Barros, *et al.*, *Climate change 2014: synthesis Report. Contribution of working groups I, II and III to the fifth assessment report of the intergovernmental panel on climate change*, IPCC , 167 (2014), arXiv:arXiv:1011.1669v3 .

[2] J. Muller, B. Rech, J. Springer, *et al.*, *TCO and light trapping in silicon thin film solar cells*, Solar Energy **77**, 917 (2004).

[3] A. Louwen, W. van Sark, R. Schropp, *et al.*, *A cost roadmap for silicon heterojunction solar cells*, Solar Energy Materials and Solar Cells **147**, 295 (2016).

[4] K. Jager, M. Fischer, R. A. C. M. M. Van Swaaij, and M. Zeman, *A scattering model for nano-textured interfaces and its application in opto-electrical simulations of thin-film silicon solar cells*, Journal of Applied Physics **111** (2012), 10.1063/1.4704372.

[5] *Solar Applied Materials Technology Corporation*, `http://www.solartech.com.tw/en/product_sputtering_targets_for_thin_film_solar_cell01.html`, accessed online: 19-08-2017.

[6] Sigma-Aldrich Co. LLC, *Next Generation Nanomaterials for Energy and Electronics*, Vol. 11 (2016) pp. 15–19, `http://www.sigmaaldrich.com/content/dam/sigma-aldrich/docs/Aldrich/Brochure/1/material-matters-v11-n1.pdf`.

[7] J. Dekker, *Transparent Conductive Oxides on Polymeric Substrates by Pulsed Laser Deposition*, Ph.D. thesis, Eindhoven University of Technology (2007).

[8] Z. Jin, I. Hamberg, and C. G. Granqvist, *Optical properties of sputter□deposited ZnO:Al thin films*, Journal of Applied Physics **64**, 5117 (1988).

[9] C. Kittel, *Solid-State Physics (Fourth Extensively Updated and Enlarged Edition): An Introduction to Principles of Materials Science* (2010) pp. 1–533, arXiv:arXiv:1011.1669v3 .

[10] A. Smets, K. Jager, O. Isabella, M. Zeman, and R. van Swaaij, *Solar Energy: The Physics and Engineering of Photovoltaic Conversion, Technologies and Systems* (UIT Cambridge, 2016) p. 488.

[11] Y. Wu, *Growth, phase and doping control in ZnO and In_2O_3 thin films prepared by atomic layer deposition*, Ph.D. thesis, Eindhoven University of Technology (2016).

[12] R. Dingle, *Scattering of electrons and holes by charged donors and acceptors in semiconductors*, The London, Edinburgh, and Dublin Philosophical Magazine and Journal of Science **46**, 831 (1955).

[13] K. Ellmer and R. Mientus, *Carrier transport in polycrystalline transparent conductive oxides: A comparative study of zinc oxide and indium oxide*, Thin Solid Films **516**, 4620 (2008).

[14] J. Y. W. Seto, *The electrical properties of polycrystalline silicon films*, Journal of Applied Physics **46**, 5247 (1975).

[15] B. Macco, H. C. M. Knoops, and W. M. M. Kessels, *Electron Scattering and Doping Mechanisms in Solid-Phase-Crystallized In_2O_3:H prepared by Atomic Layer Deposition*, ACS Applied Materials & Interfaces **7**, 16723 (2015).

[16] T. Koida, H. Fujiwara, and M. Kondo, *Hydrogen-doped In_2O_3 as high-mobility transparent conductive oxide*, Japanese Journal of Applied Physics, Part 2: Letters **46** (2007), 10.1143/JJAP.46.L685.

[17] F. O. Adurodija, L. Semple, and R. Brüning, *Real-time in situ crystallization and electrical properties of pulsed laser deposited indium oxide thin films*, Thin Solid Films **492**, 153 (2005).

[18] C. Y. Wang, V. Cimalla, H. Romanus, T. Kups, G. Ecke, T. Stauden, M. Ali, V. Lebedev, J. Pezoldt, and O. Ambacher, *Phase selective growth and properties of rhombohedral and cubic indium oxide*, Applied Physics Letters **89**, 1 (2006).

[19] E. H. Morales, Y. He, M. Vinnichenko, B. Delley, and U. Diebold, *Surface structure of Sn-doped In_2O_3 (111) thin films by STM*, New Journal of Physics **10**, 125030 (2008).

[20] S. Limpijumnong, P. Reunchan, A. Janotti, and C. G. Van De Walle, *Hydrogen doping in indium oxide: An ab initio study*, Physical Review B - Condensed Matter and Materials Physics **80**, 193202 (2009).

[21] B. Macco, *Atomic layer deposition of metal oxide thin films for Si heterojunction solar cells*, Ph.D. thesis, Eindhoven University of Technology (2016).

[22] B. Macco, H. C. Knoops, M. A. Verheijen, W. Beyer, M. Creatore, and W. M. Kessels, *Atomic layer deposition of high-mobility hydrogen-doped zinc oxide*, Solar Energy Materials and Solar Cells , 1 (2017), in press.

[23] J. E. Crowell, *Chemical methods of thin film deposition: Chemical vapor deposition, atomic layer deposition, and related technologies*, Journal of Vacuum Science & Technology A: Vacuum, Surfaces, and Films **21**, S88 (2003).

[24] R. W. Johnson, A. Hultqvist, and S. F. Bent, *A brief review of atomic layer deposition: From fundamentals to applications*, Materials Today **17**, 236 (2014).

[25] P. Poodt, D. C. Cameron, E. Dickey, and S. M. George, *Spatial atomic layer deposition: A route towards further industrialization of atomic layer deposition*, Journal of Vacuum Science & Technology A: Vacuum, Surfaces, and Films **30** (2012), 10.1116/1.3670745.

[26] J. Gaines, *Challenges for Non-Ideal Atomic Layer Deposition Processes & Systems*, `https://www.lesker.com/newweb/blog/post.cfm/challenges-for-non-ideal-atomic-layer-deposition-processes-systems` (2016), accessed on: 23-08-2017.

[27] T. Suntola and J. Antson, *Method for producing compound thin films*, (1977), US Patent 4,058,430.

[28] J. A. van Delft, D. Garcia-Alonso, and W. M. M. Kessels, *Atomic layer deposition for photovoltaics: applications and prospects for solar cell manufacturing*, Semiconductor Science and Technology **27**, 074002 (2012).

[29] A. Illiberi, F. Roozeboom, and P. Poodt, *Spatial atomic layer deposition of zinc oxide thin films*. ACS Applied Materials & Interfaces **4**, 268 (2012).

[30] M. Boccard, N. Rodkey, and Z. C. Holman, *High-mobility Hydrogenated Indium Oxide without Introducing Water during Sputtering*, Energy Procedia **92**, 297 (2016).

[31] M. Ritala, T. Asikainen, and M. Leskelä, *Enhanced growth rate in atomic layer epitaxy of indium oxide and indium-tin oxide thin films*, Electrochemical and Solid-State Letters **1**, 156 (1998).

[32] O. Nilsen, R. Balasundaraprabhu, E. Monakhov, N. Muthukumarasamy, H. Fjellvåg, and B. Svensson, *Thin films of In_2O_3 by atomic layer deposition using In(acac)$_3$*, Thin Solid Films **517**, 6320 (2009), Proceedings on the Sixth Symposium on Thin Films for Large Area Electronics.

[33] J. W. Elam, A. B. F. Martinson, M. J. Pellin, and J. T. Hupp, *Atomic layer deposition of In_2O_3 using cyclopentadienyl indium: a new synthetic route to transparent conducting oxide films*, Chemistry of Materials **18**, 3571 (2006).

[34] J. A. Libera, J. N. Hryn, and J. W. Elam, *Indium oxide atomic layer deposition facilitated by the synergy between oxygen and water*, Chemistry of Materials **23**, 2150 (2011).

[35] B. Macco, Y. Wu, D. Vanhemel, and W. M. M. Kessels, *High mobility In_2O_3:H transparent conductive oxides prepared by atomic layer deposition and solid phase crystallization*, Physica Status Solidi (RRL) – Rapid Research Letters **8**, 987 (2014).

[36] A. U. Mane, A. J. Allen, R. K. Kanjolia, and J. W. Elam, *Indium Oxide Thin Films by Atomic Layer Deposition Using Trimethylindium and Ozone*, The Journal of Physical Chemistry C **120**, 9874 (2016).

[37] A. Illiberi, B. Cobb, A. Sharma, T. Grehl, H. Brongersma, F. Roozeboom, G. Gelinck, and P. Poodt, *Spatial atmospheric atomic layer deposition of* $In_xGa_yZn_zO$ *for thin film transistors*, ACS Applied Materials & Interfaces **7**, 3671 (2015).

[38] K. Jager, O. Isabella, A. H. M. Smets, R. A. C. M. M. van Swaaij, and M. Zeman, *Solar Energy Fundamentals, Technology and Systems* (2014) pp. 1–420.

[39] S. M. Sze, K. K. Ng, J.-P. Colinge, and C. A. Colinge, *Physics of Semiconductor Devices* (2006) pp. i–x.

[40] P. Erhart, A. Klein, R. G. Egdell, and K. Albe, *Band structure of indium oxide: Indirect versus direct band gap*, Physical Review B - Condensed Matter and Materials Physics **75**, 1 (2007).

[41] O. Bierwagen and J. S. Speck, *High electron mobility* In_2O_3 *(001) and (111) thin films with nondegenerate electron concentration*, Applied Physics Letters **97**, 3 (2010).

[42] Y. Wu, B. Macco, D. Vanhemel, S. Kölling, M. A. Verheijen, P. M. Koenraad, W. M. M. Kessels, and F. Roozeboom, *Atomic layer deposition of* In_2O_3*:H from InCp and* H_2O/O_2*: Microstructure and isotope labeling studies*, ACS Applied Materials & Interfaces **9**, 592 (2017).

[43] D. M. Hofmann, A. Hofstaetter, F. Leiter, H. Zhou, F. Henecker, B. K. Meyer, S. B. Orlinskii, J. Schmidt, and P. G. Baranov, *Hydrogen: A relevant shallow donor in zinc oxide*, Phys. Rev. Lett. **88**, 045504 (2002).

[44] H. B. Profijt, S. E. Potts, M. C. M. van de Sanden, and W. M. M. Kessels, *Plasma-Assisted Atomic Layer Deposition: Basics, Opportunities, and Challenges*, Journal of Vacuum Science & Technology A: Vacuum, Surfaces, and Films **29**, 050801 (2011).

[45] U. Kogelschatz, *Dielectric-barrier discharges: Their History, Discharge Physics, and Industrial Applications*, Plasma Chemistry and Plasma Processing **23**, 1 (2003), arXiv:0005074v1 [arXiv:astro-ph] .

[46] Krishnavedala, *File:Paschen curves.svg*, `https://commons.wikimedia.org/wiki/File:Paschen_curves.svg` (2010), accessed on: 2017-08-18.

[47] J. A. Wollam Co. Inc, *CompleteEASE ™ Data Analysis Manual*, (2011).

[48] Perkin Elmer, *Applications and Use of Integrating Spheres With the LAMBDA 650 and 850 UV/Vis and LAMBDA 950 UV/Vis/NIR Spectrophotometers*, (2004).

[49] J. A. Kerszulis, *User Guide and Tutorial for Using the Cary 500 in the Reynolds Research Group*, Georgia Institute of Technology **2**, 1 (2012), `https://ww2.chemistry.gatech.edu/reynolds/sites/ww2.chemistry.gatech.edu.reynolds/files/Cary.pdf`.

[50] K. Nama Manjunatha and S. Paul, *Investigation of optical properties of nickel oxide thin films deposited on different substrates*, Applied Surface Science **352**, 10 (2015).

[51] Maschen, *File:Lorentz force particle.svg*, `https://commons.wikimedia.org/wiki/File%3ALorentz_force_particle.svg` (2012), 23-08-2017.

[52] R. W. Thurber, *The Hall Effect*, `https://www.nist.gov/pml/engineering-physics-division/hall-effect#lorentz` (2016), 2017-06-09.

[53] Keithley Instruments, *Four-Probe Resistivity and Hall Voltage Measurements with the Model 4200-SCS*, (2011).

[54] M. Sain, S. Ummartyotin, J. Juntaro, C. Wu, and H. Manuspiya, *Deposition of PEDOT: PSS nanoparticles as a conductive microlayer anode in OLEDs device by desktop inkjet printer*, Journal of Nanomaterials **2011** (2011).

[55] D. A. Neamen, *Semiconductor Physics and Devices*, 3rd ed. (McGraw Hill, 2003) p. 162.

[56] J. G. Webster, *Electrical Measurements, Signal Processing, and Displays* (CRC Press, 2004) pp. 36–47.

[57] XOS, *X-Ray Diffraction (XRD)*, `https://www.xos.com/XRD` (2017), accessed online: 2017-06-18.

[58] *X-ray diffraction*, `https://en.wikipedia.org/wiki/X-ray_crystallography#/media/File:Bragg_diffraction_2.svg` (2011), accessed online: 2017-06-19.

[59] J. Goldstein, *Scanning electron microscopy and X-ray microanalysis: a text for biologists, materials scientists, and geologists*, illustrated, reprint ed. (Plenum Press, 1981) p. 673.

[60] *Diagram of a scanning electron microscope with English captions*, `https://commons.wikimedia.org/wiki/File:Schema_MEB_(en).svg` (2010), accessed online: 2017-08-14.

[61] H. Butt, K. Graf, and M. Kappl, *Physics and Chemistry of Interfaces*, Physics textbook (Wiley, 2006).

[62] *Atomic Layer Deposition (ALD)*, `https://www.tue.nl/en/university/departments/applied-physics/research/research-groups/research-cluster-plasma-and-radiation/plasma-and-materials-processing-pmp/facilities/technologies/atomic-layer-deposition-ald/`, accessed online: 01-08-2017.

[63] W. G. Jeong, E. P. Menu, and P. D. Dapkus, *Steric hindrance effects in atomic layer epitaxy of InAs*, Applied Physics Letters **55**, 244 (1989).

[64] K. Oura, V. Lifshits, A. Saranin, A. Zotov, and M. Katayama, *Surface Science: An Introduction*, Advanced Texts in Physics (Springer Berlin Heidelberg, 2003).

[65] S. B. S. Heil, J. L. van Hemmen, C. J. Hodson, N. Singh, J. H. Klootwijk, F. Roozeboom, M. C. M. van de Sanden, and W. M. M. Kessels, *Deposition of TiN and HfO_2 in a commercial 200 mm remote plasma atomic layer deposition reactor*, Journal of Vacuum Science & Technology A **25**, 1357 (2007).

[66] *Crsytallographic Open Database - Information card for* 1010341, `http://www.crystallography.net/cod/1010341.html`, accessed online: 2017-08-14.

[67] K. Norrish and R. M. Taylor, *Quantitative analysis by X-ray diffraction*, Clay Minerals **5**, 98 (1962).

[68] A. L. Patterson, *The Scherrer Formula for X-Ray Particle Size Determination*, Physical Review **56**, 978 (1939).

[69] H. Fujiwara and M. Kondo, *Effects of carrier concentration on the dielectric function of ZnO:Ga and In_2O_3:Sn studied by spectroscopic ellipsometry: Analysis of free-carrier and band-edge absorption*, Physical Review B - Condensed Matter and Materials Physics **71**, 1 (2005).

[70] R. Santbergen, T. Meguro, T. Suezaki, G. Koizumi, K. Yamamoto, and M. Zeman, *Gen Pro4 optical model for solar cell simulation and its application to multijunction solar cells*, IEEE Journal of Photovoltaics **7**, 919 (2017).

[71] D. Zhang, W. Verhees, M. Dörenkämper, *et al.*, *Combination of advanced optical modelling with electrical simulation for performance evaluation of practical 4-terminal perovskite/c-si tandem modules*, Energy Procedia **92**, 669 (2016), proceedings of the 6th International Conference on Crystalline Silicon Photovoltaics (SiliconPV 2016).

[72] J. Tauc, R. Grigorovici, and A. Vancu, *Optical Properties and Electronic Structure of Amorphous Germanium*, Physica Status Solidi (B) **15**, 627 (1966).

[73] A. Walsh, J. L. F. Da Silva, S. H. Wei, *et al.*, *Nature of the band gap of In_2O_3 revealed by first-principles calculations and X-ray spectroscopy*, Physical Review Letters **100**, 2 (2008).

[74] Z. C. Jin, I. Hamberg, and C. G. Granqvist, *Optical properties of sputter-deposited ZnO:Al thin films*, Journal of Applied Physics **64**, 5117 (1988).

[75] T. J. Coutts, D. L. Young, and X. Li, *Characterization of transparent conducting oxides*, MRS Bulletin **25**, 58–65 (2000).